UCLouvain

École polytechnique de Louvain

Modeling & Analysis of the tibio-femoral joint contact by coupling surface meshes and multibody formalism

Author: **Baptiste ISTACE**
Supervisors: **Nicolas DOCQUIER, Paul FISETTE**
Reader: **Philippe LEFÈVRE**
Academic year 2023–2024
Master [120] in Mathematical Engineering

Acknowledgement

This thesis completes five years of study in applied mathematics civil engineering. It's time for me to honour all the people who have contributed in one way or another to the success of this experience.

I wish first of all to thank the team of my supervisors Prof. Paul Fisette and Prof. Nicolas Docquier who supported me and helped me to complete this thesis, and in particular Olivier Lantsoght who never counted the hours he spent helping me when I needed it. I would also thank the reader, Philippe Lefèvre, for the time he spent reading my work.

This thesis is the culmination of an academic career rich in emotions and wonderful meetings, and I am grateful to my parents for having always supported and encouraged me during the more difficult times.

Thanks to everyone who played a part in my time at UCL. Thanks to each and every one of you for supporting me, helping me, guiding me, advising me and enriching my knowledge. Thanks to all of you, today I'm in the right place.

Baptiste

Abstract

This thesis presents a work on the modeling and analysis of contact in the tibio-femoral joint by integrating surface meshes with a multibody formalism. The aim is to develop an accurate and efficient model to simulate the complex interactions in the knee joint, focusing on the contact dynamics between the femur and the tibia. In particular, advanced computational techniques, accurate anatomical meshes, collision detection algorithms and dynamic modeling of contact forces are investigated.

A detailed overview of the anatomy of the knee joint and the principles of multibody system dynamics will be provided. A number of aspects of knee motion and joint surface geometry are then explored, highlighting the critical features required for accurate simulation.

The thesis details the methodology for contact detection using meshes, including both approximate surfaces and scanned data surfaces. Advanced algorithms such as the Gilbert-Johnson-Keerthi (GJK) algorithm, the Expanding Polytope (EPA) algorithm and the Ray Casting algorithm are implemented and validated to ensure that contact detection is accurate.

The dynamics of contact forces are modelled using different theoretical approaches, including elastic foundation models and Hertz contact theory. These are validated by simulations, demonstrating their ability to accurately reproduce real-world biomechanical behaviours.

Finally, the results provide potential improvements and recommendations for future research. This work contributes to the field of biomechanical engineering by offering a viable method for simulating the dynamics of the knee joint. These may be useful for clinical diagnosis, surgical design and the design of orthopaedic implants.

Contents

List of Figures

List of Tables

Chapter 1

Introduction

1.1 Overview

After replacement of a knee with a prosthesis i.e total knee arthroplasty (TKA), around 20% of patients continues to suffer from pain [1].

The knee joint is the largest and most complex joint in the human body. Despite the extensive research conducted to date, there is still much to be discovered about the functional aspects of the knee joint. The structure of the knee is a compromise, allowing the leg to move while maintaining stability [2].

The simulation of human movement represents a valuable application of multibody dynamics. A human body model can be represented as a complex mechanism, typically using rigid bodies to represent body segments, simple kinematic joints to represent anatomical joints, active torque elements to represent muscle forces and various contact models to represent external contacts [3]. The use of more complex models in specific cases can improve the accuracy of the simulation. For example, a joint can be modelled by incorporating contact, ligaments and muscles, as opposed to utilising a simplified kinematic joint.

Often, surgeons focus primarily on geometric aspects when designing and implanting prostheses, ensuring that the shape and alignment are correct. However, it is just as crucial to take into account the internal forces within the joint to avoid pain or complications in other parts of the body after the operation. By neglecting internal forces and stresses, there is a risk that the implantation of a prosthesis, although geometrically optimised, could lead to biomechanical imbalances causing pain or dysfunction elsewhere in the musculoskeletal system.

The aim of this chapter is to provide a brief description of the anatomy of the joint, an overview of existing knowledge and previous studies of the kinematics of the knee joint. We will also talk very vaguely about multibody dynamics, which in this work will be used to explain what happens within the knee joint.

1.2 Anatomy of Human Knee Joint

The knee is a joint that allows the bones in contact to move relative to each other within a certain range of motion, with limitations, which is called a diarthrodial joint. The different reference planes, anatomical directions and relative directions are outlined in Appendix A.

To represent the knee joint, mathematical models are developed that respect the laws of physics, such as equilibrium, and consist of a set of mathematical relationships between the variables in the system. Two main types of mathematical models are identified in the literature: the phenomenological and anatomical models [4].

1.2.1 Phenomenological Models

The first type of models is the phenomenological models. These models are employed to describe the response of the knee without consideration of its actual structural composition. In [5], the model used is a pivot joint (or hinge joint), which approximates the primary function of the knee (providing an axis of rotation). However, it does not model tibio-femoral contact forces, ligament forces, or muscle forces. Consequently, a pivot joint may be employed to model the knee when it is not the primary focus of a given model. This may be the case in whole-body models, where the objective is to analyse global motion rather than specific internal forces.

1.2.2 Anatomical Models

Anatomical models represent the second type of models. These models were developed to study the behaviour of the various structural components that make up the knee joint and require precise geometry to match the real anatomy. The tibio-femoral surfaces and contact (bone, cartilage and meniscus), ligament forces and muscle forces are therefore introduced. As a result, anatomical models are generally more complex and computationally expensive than phenomenological models, but they provide a more complete and accurate model of the knee.

Bones

Figure 1.1 shows the knee joint connecting the femur and tibia, as well as the fibula, another long bone parallel to the tibia that is not implicated in the joint. There is also the patella, a small, flat, rounded bone located at the front of the knee joint. It is embedded in the quadriceps tendon and articulates with the femur.

The knee joint comprises three contact surfaces: the medial and lateral tibio-femoral and the patello-femoral. It should be noted that the present study is primarily concerned with the tibio-femoral contact. At the knee, the distal femur and proximal tibia expand and divide into distinct sections, known as condyles. The posterior femoral condyles are convex in the sagittal and frontal planes and are almost spherical [6]. A more detailed discussion of this topic can be found in Section 2.2.1.

The femoral condyles are separated by an intercondylar fossa, which extends anteriorly to

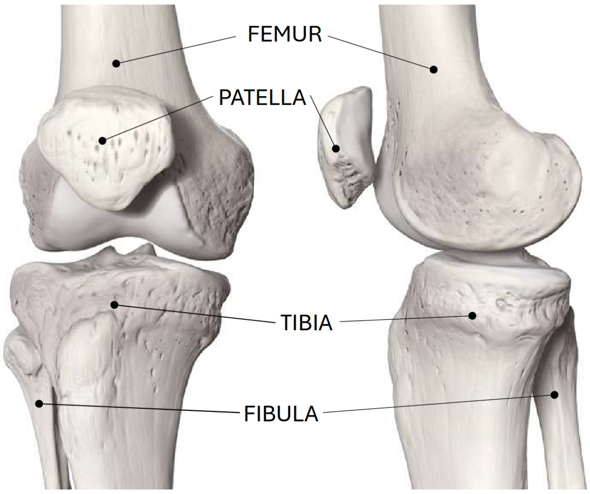

Figure 1.1: The bones of the right knee joint: frontal view (left) and sagittal view (right). Image modified from [7].

form the patellofemoral groove, in which the patella moves. Conversely, the tibial condyles display a slight concavity in the frontal plane. In the sagittal plane, the medial condyle is flat, while the lateral condyle displays a slight convexity [2]. The joint between the tibia and femur is formed by surfaces that do not correspond perfectly with one another. The two tibial condyles are inclined in a posterior direction.

Ligaments

In the knee, the ligaments guide the movement of the joint and, by transmitting forces through the joint, also provide stability. Ligaments are passive structures, i.e there is no neural input, although they may play a sensory role [8]. The four main ligaments that cross the knee are illustrated in Figure 1.2: the Anterior Cruciate Ligament (ACL), the Posterior Cruciate Ligament (PCL), the Medial Collateral Ligament (MCL) and the Lateral Collateral Ligament (LCL).

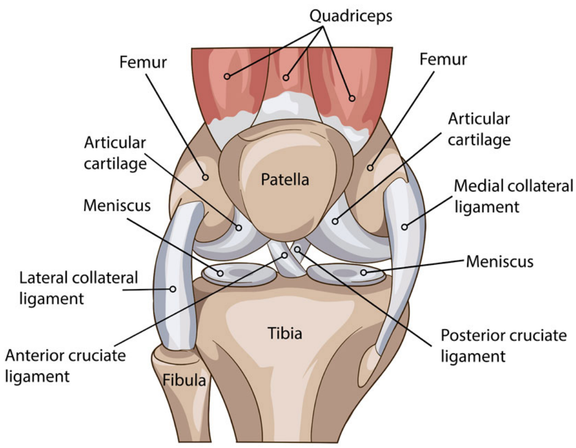

Figure 1.2: The anatomy of the knee and its ligaments in a frontal view. Image from [9].

By definition, a ligament is a soft tissue structure that connects one bone to another. Most of them connect the tibia to the femur, but the LCL connects the femur to the fibula.

Cartilage

Figure 1.2 also shows the quadriceps muscle and the meniscus, as well as the articular cartilage.
The extremities of joint bones are covered with a tough, flexible connective tissue. This tissue, called cartilage, helps reducing friction and absorb impacts, which gives the surface a coefficient of friction as low as $\mu = 0.01$ in healthy human articular joints [10]. In such conditions, friction is negligible, the effect of shear stress on the contact surface could be neglected.

Meniscus

As illustrated in Figure 1.2, the meniscus is situated between the bones in both the medial and lateral compartments of the knee. The meniscus serves to reduce contact stresses on the condyles by filling the space between the bones.

Muscles

Unlike ligaments, muscles are active structures, meaning that they are activated by the central nervous system. Skeletal muscles activate the bones of the body to produce movement at joints and provide stability by resisting movement between joints.
The muscles of the knee are grouped into two parts: flexors and extensors. The flexors are primarily located in the hamstrings group, while the extensors are found in the quadriceps group.

Figure 1.3 illustrates another view of the anatomy of the knee joint, where the muscles are more visible. The tendons are represented here, which serve to attach the muscles to the bones.

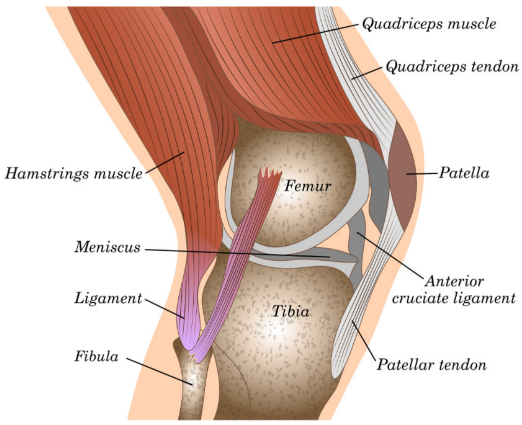

Figure 1.3: Another view (sagittal) of the anatomy of the knee joint. Image was made by orthopaedist [11].

1.3 Dynamics of Multibody Systems

The equations to be solve in the mathematical model are those of the dynamics of a multibody system. This section gives a very brief overview of these equations, which are solved with the Robotran software [12].

1.3.1 Basic Principles

This subsection serves to provide a brief reminder of the essential elements of multibody formalisms that will be employed throughout the rest of this work [1].

A general multibody system is a mechanical system composed of rigid bodies connected by n joints, where its topology is described by a tree structure.
The equations describing the dynamics in an unconstrained case can be represented by the following equation:

$$M(q)\ddot{q} + c(q, \dot{q}, frc, trq, g) = Q(q, \dot{q}) \tag{1.1}$$

where

- M is a matrix of size $n * n$ representing the symmetric mass matrix of the system.
- c is the nonlinear dynamic vector of size n containing the gyroscopic, centripetal, gravity terms and the external forces and torques.
- Q is the vector of size n representing the generalized joint forces/torques of the system.
- q is the vector of size n of the joint generalized coordinates; $\dot{q}$ and $\ddot{q}$ are the generalized velocities and accelerations respectively.

If the model contains loops of bodies, then it becomes a constrained multibody system, and algebraic constraints satisfy to close the loops. In order to incorporate the constraint forces into the dynamic equation (Eq. 1.1), it is necessary to employ the Lagrange multiplier technique.

In sum, the constrained dynamics are described by a set of the differential and algebraic equations (DAE):

$$M(q)\ddot{q} + c(q, \dot{q}, frc, trq, g) = Q(q, \dot{q}) + J^T\lambda \tag{1.2}$$

$$h(q) = 0 \tag{1.3}$$

$$\dot{h}(q, \dot{q}) = J(q)\dot{q} = 0 \tag{1.4}$$

$$\ddot{h}(q, \dot{q}, \ddot{q}) = J(q)\ddot{q} + \dot{J}(q, \dot{q})\dot{q} = 0 \tag{1.5}$$

where

- $h(q)$ represents the m loop algebraic constraints, of size m.
- J is the constraints Jacobian matrix of size $m * n$.

[1] For more details on this subject, we invite the reader to consult the book *"Symbolic Modeling of Multibody Systems."* by J.C Samin and P. Fisette [13].

- λ is the vector of the Lagrange multipliers associated with the constraints of size m.

The constraints refer to cuts aimed at opening each loop in order to write the closing constraints 1.3. Without going into too much detail, this is because a tree structure is desired. Here are the two types of cuts used in the rest of this work:

Cut of a Ball Joint

In the first case, three position constraints are applied to enable the loop to close. This case applies when the loop contains a ball joint that can be considered "ideal" from a geometric and dynamic point of view (Fig. 1.4).
Let's consider $\mathbf{x}^P$ and $\mathbf{x}^Q$ as the positions of the points P and Q located at the centre of the ball joint and belonging respectively to the primary and secondary kinematic chains, this constraint applies for each time t :

$$h(q,t) = \mathbf{x}^P(q,t) - \mathbf{x}^Q(q,t) = 0 \tag{1.6}$$

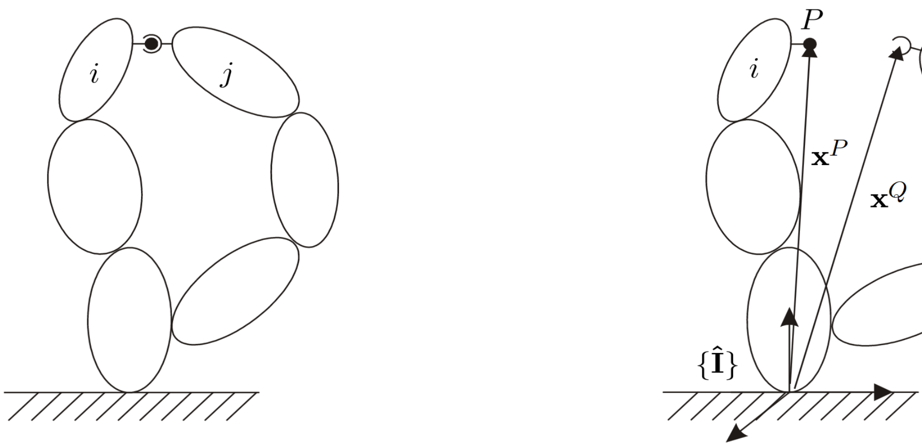

Figure 1.4: Cut of a ball joint. Image taken from the book [13].

Cut of a Connecting Rod

The second case is equivalent to two ball joints separated by a constant distance l_{rod} that represents a connecting rod whose mass and inertia can be neglected (Fig. 1.5).
Considering $\mathbf{x}^P$ and $\mathbf{x}^Q$ as the positions of points P and Q at the ends of the connecting rod on the primary and secondary body respectively, there is one constraint:

$$\|\mathbf{x}^P(q,t) - \mathbf{x}^Q(q,t)\| - l_{rod} = 0, \quad \text{and } l_{rod} > 0 \tag{1.7}$$

Returning to the DAE system (1.2–1.5), to solve it, now that the $h(q)$ constraints are established, it is possible to use the coordinate partitioning method. In simple terms, the aim of this method is to reduce the set of DAEs to a set of ODEs. To achieve this, the generalized coordinate q are split into two parts, the $(n-m)$ independent ones u and the m dependent

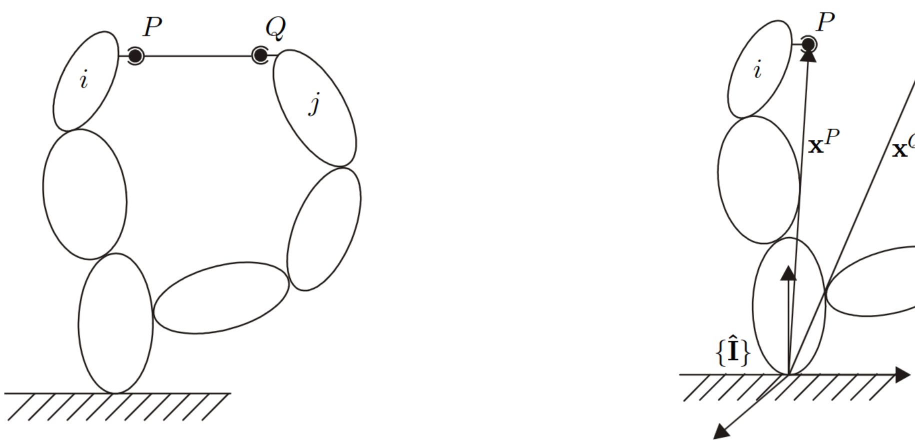

Figure 1.5: Cut of a connecting rod. Image taken from the book [13].

ones v, which are associated to the constraints. This gives the following representation:

$$q = \begin{pmatrix} u \\ v \end{pmatrix} ; J = \begin{pmatrix} J_u & J_v \end{pmatrix}$$

and at the differential equations are also partitioned as follows:

$$\begin{pmatrix} M_{uu} & M_{uv} \\ M_{vu} & M_{vv} \end{pmatrix} \begin{pmatrix} \ddot{u} \\ \ddot{v} \end{pmatrix} + \begin{pmatrix} c_u \\ c_v \end{pmatrix} = \begin{pmatrix} Q_u \\ Q_v \end{pmatrix} + \begin{pmatrix} J_u^T \\ J_v^T \end{pmatrix} \lambda \tag{1.8}$$

The dependent variables v are eliminated by solving the constraints 1.3, 1.4, 1.5 at each time step. This results in a system of ordinary differential equations (ODE) of size $(n - m)$ for the independent variables u:

$$M(u)\ddot{u} + f(u, \dot{u}) = 0 \tag{1.9}$$

Note that $(n - m)$ is the number of degrees of freedom of the multi-body system. From a mathematical point of view, the reduction amounts to projecting the equations of motion 1.2 into the constraint space along the permitted directions of motion.

Physical Interpretation

Once the equations have been solved, the most important thing is to be able to analyse the results physically. This is accomplished by measuring the values of the Lagrange multipliers λ associated with the constraints.
In the two cases described above, a Lagrange multiplier is assigned with each constraint. In the first case, the Lagrange multipliers are equal to the components of the constraint force F that keeps point P in contact with point Q, so :

$$\lambda_t = F$$

In the second case, λ_t represents the force per unit length transmitted by the rod:

$$\lambda_t = \frac{F}{l_{rod}}$$

This will serve in Chapter 5, where the force within the constraints to be applied will be analysed.

1.3.2 Driven Variables

In some cases, the independent generalized coordinates u are not considered as variables because their motion is either simply locked or forced to obey a specific function $f(t)$. In the present formalism, these variables are designated as driven, denoted by u^D. In resolving them, it is necessary to consider them as part of the set of independent variables, u, whose value obeys the specific function $f(t)$.

It should be noted that the driven variables cannot be integrated over time.
Consider u splited into $u = (u^I, u^D)$, where u^D are the driven variables and u^I the really independant variables. Equation 1.9 becomes :

$$\begin{pmatrix} M_{II} & M_{ID} \\ M_{DI} & M_{DD} \end{pmatrix} \begin{pmatrix} \ddot{u}^I \\ \ddot{u}^D \end{pmatrix} + \begin{pmatrix} f_I \\ f_D \end{pmatrix} = \begin{pmatrix} 0 \\ \lambda^D \end{pmatrix} \tag{1.10}$$

where λ^D is the Lagrange multiplier associated with the driven variables. The reduced form of the dynamic of a constrained multibody system with driven variables is then :

$$M_{II}\ddot{u}^I + f_I + M_{ID}\ddot{u}^D = 0 \tag{1.11}$$

This type of variable can be used in this work, and will be described in more detail in Chapter 2.

1.3.3 Static Equilibrum

In this work, the different forces involved in the static equilibrium of the knee will be examined. A static equilibrium is reached when $\ddot{u} = 0$ and $\dot{u} = 0$. Equations 1.2–1.5 becomes

$$\begin{cases} c(q, frc, trq, g) = Q(q) + J^T\lambda \\ h(q) = 0 \end{cases} \tag{1.12}$$

Reducing the set in the same way as equation 1.9, the following equation is obtained :

$$f(u) = 0 \tag{1.13}$$

This system of equations can be solved with the help of a Newton-Raphson method. If f denotes the equations to cancel, the Newton-Raphson algorithm iterates on the equilibrium variables $x = u$ (excluding the driven variables d) until the equilibrium state is obtained.

$$x_{k+1} = x_k - \left(\frac{\partial f}{\partial x}(x_k)\right)^{-1} f|_{x=x_k} \tag{1.14}$$

Being in a equilibrium position in the different models will enable to compare results.

1.4 Aims and Structure of the Thesis

The objective of this study is to employ a multibody approach to model the interaction of the tibio-femoral joint, with the aim of gaining a better understanding of the forces exerted within this joint. Such a model could, for example, assist surgeons in the fitting of prostheses or in the identification of risky positions and movements, with a view to avoiding injuries. Given the unique nature of each human body, it is imperative to determine the degree of precision required in the model parameters, with meshes serving as a potential means of achieving this. Accordingly, this study will examine the degree of precision required and the impact of a minor degree of deviation on the results.

Specifically, we will concentrate on the geometry of the right knee, where the dimensions are given in Appendix B.1. Our analysis will be limited to the tibio-femoral contact.

Initially, Chapter 2 introduces important concepts for the modeling of the knee model, such the way to represent the geometry of the articular surface. The use of finite elements and scanners is also studied to see how important the precision of the geometry is. To signify these dynamics using meshes, it is necessary to know how to detect contact. Chapter 3 explains the meshes used. Once this collision surface has been found, Chapter 4 looks at how to apply the force. Next, the results obtained will be compared with the different methods used in order to determine the importance of accuracy. This is discussed in Chapter 5. Finally, Chapter 6 will examine the results obtained and the various improvements that could be made in order to model the tibio-femoral contact more accurately.

Chapter 2

Knee Modeling

Knee modeling is essential for understanding and reproducing the biomechanical complexities of this joint. This chapter introduces the various aspects of knee modeling that will be employed in order to represent tibio-femoral contact.

2.1 Knee Motion

Knee motion is a complex and essential mechanism, crucial to daily mobility as it allows relative movements between the tibia and the femur. This section examines the three-dimensional geometry of this joint movement, providing a comprehensive description based on three rotations and three translations.

2.1.1 Joint Position

To determine the position of the knee joint, the starting point is the position of the femur, which is calculated using a virtual multibody sensor s attached to it. The sensor data (x, y, z, θ_x, θ_y, θ_z) is used to derive the rotation matrix describing the orientation of the sensor relative to a fixed reference frame.
For a sequence of angles $\theta_z \to \theta_y \to \theta_x$ such that $[\hat{X}_s] = R[\hat{I}]$, the rotation matrix R is calculated as follows:

$$R = \begin{pmatrix} 1 & 0 & 0 \\ 0 & \cos(\theta_x) & -\sin(\theta_x) \\ 0 & \sin(\theta_x) & \cos(\theta_x) \end{pmatrix} \begin{pmatrix} \cos(\theta_y) & 0 & \sin(\theta_y) \\ 0 & 1 & 0 \\ -\sin(\theta_y) & 0 & \cos(\theta_y) \end{pmatrix} \begin{pmatrix} \cos(\theta_z) & -\sin(\theta_z) & 0 \\ \sin(\theta_z) & \cos(\theta_z) & 0 \\ 0 & 0 & 1 \end{pmatrix}$$

and the translation vector $\mathbf{x}$ is equal to $[\hat{I}]^T \begin{pmatrix} x & y & z \end{pmatrix}^T$. Figures 2.1 and 2.2 represent the different notations.
In this case, the femur is supposed to be locked in translation and rotation relative to the inertial reference frame. This facilitates determination of the position of the knee joint, as well as the position of the tibia.

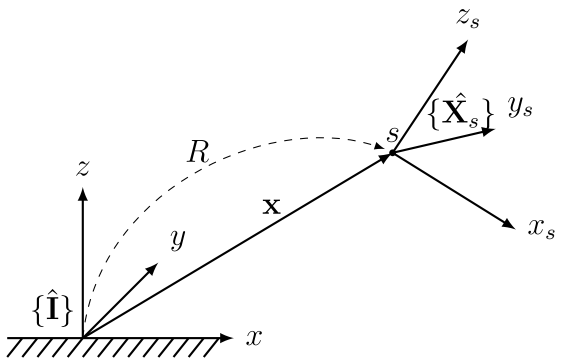

Figure 2.1: Representation of two three-dimensional coordinate systems. The (x, y, z) reference is the inertial reference, while the (x_s, y_s, z_s) reference is obtained by rotation R. The vector $\mathbf{x}$ represents the position vector of the point s relative to the origin of the inertial reference frame. The annotations $\{\hat{\mathbf{I}}\}$ and $\{\hat{\mathbf{X}}_s\}$ indicate the bases of the respective coordinate frames.

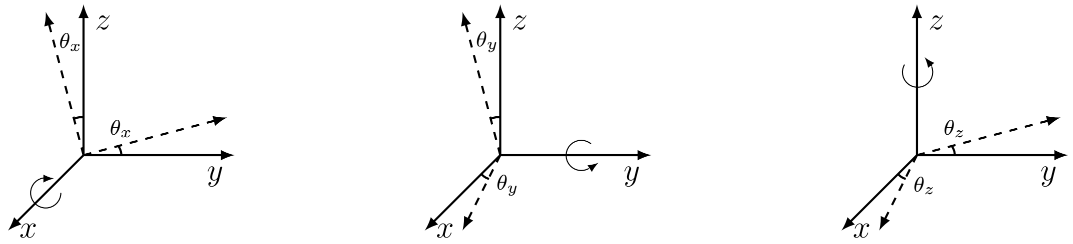

Figure 2.2: The three rotations θ_x, θ_y and θ_z around the x, y and z axes, respectively.

2.1.2 Joint Rotations/Translations

The position of the tibia will be described in terms of the three relative translations and three rotations of the joint in relation to the femur. For the rotations, the three axes are, as follows:

- **Flexion/Extension axis** : $\hat{e}_1 = \hat{f}_t$ around the transverse axis (x-axis)
- **Internal/External axis** : $\hat{e}_3 = \hat{i}_t$ around the longitudinal axis (z-axis)
- **Abduction/Adduction axis** : $\hat{e}_2 = \hat{e}_3 \times \hat{e}_1 = \hat{a}_t$ around the anteroposterior axis (y-axis)

With regard to translation, the right direction was always assigned as positive x ($\hat{e}_1$), the anterior direction as positive y ($\hat{e}_2$), and the superior direction as positive z ($\hat{e}_3$). These terms are shown in Figure 2.3. As a reminder, anatomical vocabulary is explained in Appendix A. Obviously, each rotation and translation is restricted by the different anatomical structures of the knee joint. As a reminder, Figure 1.2, which represents the anatomy of the knee and its ligaments in a frontal view, demonstrates that :

- **Flexion/Extension**: Limited mainly by muscles such as the quadriceps and two cruciate ligaments.
- **Abduction/Adduction**: Determined by the joint's spherical structures.

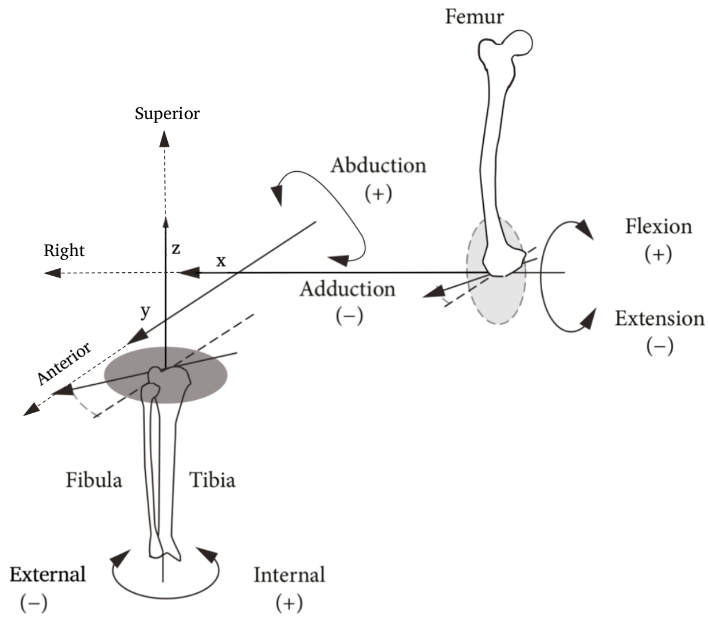

Figure 2.3: The knee joint system, including the rotations and directions used.

- **Internal/External**: Limited by the four ligaments.
- **Transverse axis** $\hat{e}_1$: Depends mainly on cruciate ligaments.
- **Anteroposterior** $\hat{e}_2$: Depends mainly on collateral ligaments.
- **Longitudinal** $\hat{e}_3$: Determined by the joint's spherical structures.

The nature of the joints will be adapted according to the model applied. Indeed, as explained later in Chapiter 5, depending on whether the condyles are considered flexible or not, or whether the constraints of the ligaments are added, the model will contain (or not) independent, dependent and driven joints.

The only parameter we will not be discussed in this work is the force of the quadriceps muscle. The muscle starts at the pelvis [1], bypasses the patella and attaches to the tibia (see Fig 1.3). It introduces a traction force "between" the tibia and the femur.

The force of the muscle is considered to oppose all the forces that would cause the knee joint to rotate in flexion/extension. Let's block the rotation of the knee in flexion and see what happens without this movement. A driven variable is therefore used to ensure that the rotation of the flexion maintains a constant value. This is a simplification of the model, but it is a good starting point for understanding the knee joint.

2.2 Articular Surface Geometry

Geometry of the articular surface enables consistent coordinate systems to be defined, essential for accurate modeling of joint motion. This section examines the estimation of

[1]The pelvis (*basin* in French) is a bone structure located at the base of the vertebral column and at the articulation of the lower limbs

contact point displacements, with a particular focus on the modeling approaches proposed by Feikes [14] and Peikes *et al.* [15]. Finally, the geometry of the articular surface is an essential factor in a knee mobility model.

2.2.1 Femoral Condyles

Firstly, the femoral condyles can be modelled using perfect spheres. These were best-fitted to the points measured on each femoral condyle by minimising the sum of the squares of the distances between each n data point and the surface of the sphere.

$$\min_{c,R} \sum_{i=1}^{n} (\|p_i - c\| - R)^2$$

where p_i is the point i of the tibia mesh data, c is the center of the sphere and R is the radius of the sphere.
This gives an mean error of :

$$ME = \frac{1}{n} \sum_{i=1}^{n} \|p_i - c\| - R \tag{2.1}$$

The femoral condyle can also be represented using polynomials. To obtain this, the Cartesian coordinates (x_i, y_i, z_i) are written in Spherical coordinates (r_i, θ_i, ϕ_i) (see Appendix C.1). The radial coordinate r_i is then described by a polynomial as a function of θ_i and ϕ_i :

$$r = f(\theta, \phi) = \sum_{i=0}^{k} \sum_{j=0}^{m} a_{ij} \theta^i \phi^j \tag{2.2}$$

where the best-fit a_{ij} coefficients were determined by a least-squares method [2]. The mean error of fit was then expressed as

$$ME = \frac{1}{n} \sum r_i - f(\theta_i, \phi_i) \tag{2.3}$$

2.2.2 Tibial Condyles

The tibial condyles are approximated by planes. The latter are fitted to the measured points on each tibial condyle by minimising the sum of the squares of the distances between each data point and the surface of the plane (Fig. 2.4a).
The equation of a plane is given by:

$$z = ax + by + c \tag{2.4}$$

and, using the principle of least squares, the error $S(a, b, c)$ is minimised.

$$\min_{a,b,c} \underbrace{\sum_{i=1}^{n} (z_i - (ax_i + by_i + c))^2}_{S(a,b,c)} \tag{2.5}$$

In this case, used for the analyses in Chapter 5, the result of the plane equation is :

[2]Least-square is calculated using Python's "scipy.optimiser.lestsq" function.

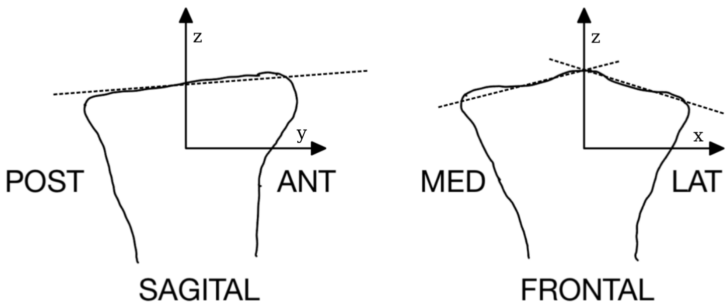

(a) Representation of the dotted line z-plane using the least squares principle.

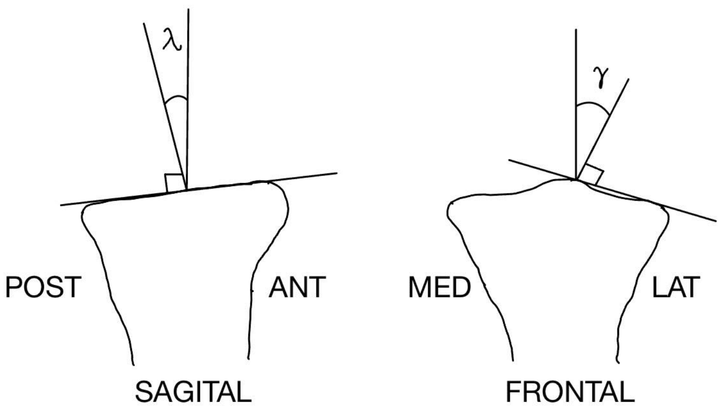

(b) Angles in the sagittal λ and frontal γ planes which describe the orientation of the planes fitted.

Figure 2.4: Planes fitted to the medial and lateral tibial condyles in the sagittal and frontal views. Image inspired from [14].

- For the Medial Tibial plane : $z = -0.12x - 0.024y - 0.0041$
- For the Lateral Tibial plane : $z = 0.19x - 0.013y - 0.0038$

Using the simple calculations described in Appendix C.2, the angles λ and γ representing the orientation of the planes fitted to the tibial condyles can be found. These angles are shown in Figure 2.4b. In the diagram at the bottom of Figure 2.5, the representation of these planes on the mesh at the top of the tibia can be observed.

At the top of Figure 2.5, there are a few outliers, unlike the femoral condyles (example circled in red).

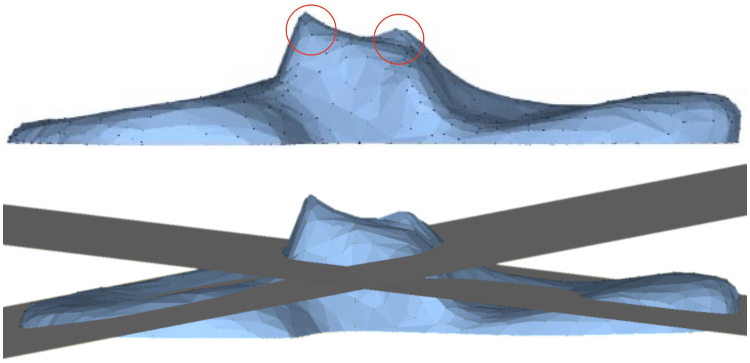

Figure 2.5: Frontal view of the tibial plateau mesh, with an example of the outliers in red at the top and the planes approximating the tibial condyles at the bottom.

Least squares methods are sensitive to outliers. Statistical analysis was therefore used to identify and remove outliers. The planes have been adjusted accordingly. Table 2.1 displays the values of angles λ and γ with their associated mean errors. The mean error has also been calculated when transverse plane is considered, i.e. when angles λ and γ are ignored.

	Medial condyle				**Lateral condyle**			
	Free			**Tran**	**Free**			**Tran**
	λ [°]	γ [°]	ME	ME	λ [°]	γ [°]	ME	ME
With outliers	−0.57	−6.23	2.27	2.57	−0.52	10.14	2.01	2.63
Without outliers	−0.36	−5.93	1.88	2.04	−0.34	9.82	1.62	2.01

Table 2.1: The values of angles (°) in the sagittal λ and frontal γ planes describe in Figure 2.4b with the associated mean error (mm) for planes with and without outliers. The Free plane represents a freely adjusted plane considering the angles λ and γ, while the Tran plane refers to a transverse plane where this angles are ignored.

It can be seen that removing the outliers reduces the mean error. It appears that the mean error is smaller for the fitted planes than for the transverse planes.

In another way, the tibial condyles can also be adjusted by polynomials as for the femoral ones. The polynomial function is defined as follows:

$$z = f(x, y) = \sum_{i=0}^{k} \sum_{j=0}^{m} a_{ij} x^i y^j \tag{2.6}$$

The best-fit coefficients a_{ij} are determined by minimising the error between the fitted surface and the measured points. The error is defined as the sum of the squared differences between the measured and fitted points.

2.2.3 Discussion

Using the previous expression, the accuracy of the approximation will depend on the degree of the polynomial. Table 2.2 and Table 2.3 represent the mean error as a function of the polynomial degree for the tibia and femur, respectively. These two tables are the results from Feikes [14], while the results in Tables 2.4 and 2.5 are those calculated using our model. Note that in our case we use meshes obtained from tibia and femur scans, which will be explained in detail in Chapter 3.
The sphere combined with a transverse plane is the case where a degree 0 polynomial is considered. The error remains within the same order of magnitude. In addition, using a degree 3 polynomial for the tibia and degree 4 for the femur is one of the best ways to describe the geometry of the articular surface. This is in line with Wismans *et al.* [16].

Degree		**Mean Error (mm)**		**Accuracy Increase (%) (relative to previous)**	
k	m	**Medial**	**Lateral**	**Medial**	**Lateral**
0	0	2.41	2.15	-	-
1	1	0.975	1.66	59.5	22.8
2	2	0.617	0.624	36.7	62.4
3	3	0.519	0.463	15.9	25.8
4	4	0.501 (RD)	0.443 (RD)	3.5	4.3
5	5	0.494 (RD)	0.44 (RD)	1.4	0.7

Table 2.2: Mean errors associated with the polynomial degree for the tibial condyles (RD = Rank Deficient). Results taken from [14].

Degree		**Mean Error (mm)**		**Accuracy Increase (%) (relative to previous)**	
θ	ϕ	**Medial**	**Lateral**	**Medial**	**Lateral**
0	0	1.86	1.55	-	-
1	1	1.75	1.54	5.9	0.7
2	2	1.48	1.31	15.4	14.9
3	3	0.791	0.853	46.6	34.9
4	4	0.750	0.789	5.2	7.5
5	5	0.722	0.784	3.7	0.6
6	6	0.718	0.774	0.6	1.3

Table 2.3: Mean errors associated with the polynomial degree for the femoral condyles. Results taken from [14].

Although increasing the degree of the polynomial reduces the average error, approximating the geometry of the articular surface by a degree 0 polynomial, i.e. a sphere on a plane, is already a good estimate. Let's start with a transverse plane in contact with a sphere, which will be studied in Chapter 5.

Degree		**Mean Error (mm)**		**Accuracy Increase (%) (relative to previous)**	
k	m	**Medial**	**Lateral**	**Medial**	**Lateral**
0	0	2.61	2.83	-	-
1	1	2.33	2.03	10.73	28.27
2	2	1.46	1.35	37.33	33.49
3	3	1.19	1.19	18.49	11.85
4	4	0.89 (RD)	1.01 (RD)	25.21	15.12

Table 2.4: Mean errors associated with the polynomial degree for the tibial condyles (RD = Rank Deficient).

Degree		**Mean Error (mm)**		**Accuracy Increase (%) (relative to previous)**	
θ	ϕ	**Medial**	**Lateral**	**Medial**	**Lateral**
0	0	2.02	1.96	-	-
1	1	1.91	1.87	5.45	4.59
2	2	1.52	1.11	20.42	40.64
3	3	1.223	0.926	19.54	16.58
4	4	1.186	0.856	3.03	7.56
5	5	1.113	0.852	6.16	0.47
6	6	1.108	0.848	0.45	0.47

Table 2.5: Mean errors associated with the polynomial degree for the femoral condyles.

Figure 2.6 illustrates the representation of the tibial surface using degree 3 polynomials from Table 2.4.

2.3 Ligaments

This section focuses on the modeling of ligaments. They are fundamental to the stability of the knee and the function of the joint. Their mechanical complexity and dynamic interaction with other anatomical structures of the knee require detailed modeling to understand their behaviour under various conditions.

In [17, 18], a commonly used model considers ligaments to be flexible.
The force applied to the ligament is written as :

$$f = \begin{cases} \frac{1}{4}k\epsilon^2/\epsilon_l & \text{if } 0 \leq \epsilon \leq \epsilon_l \\ k(\epsilon - \epsilon_l) & \text{if } \epsilon > \epsilon_l \\ 0 & \text{if } \epsilon < 0 \end{cases} \tag{2.7}$$

with

$$\epsilon = \left(\frac{l - l_0}{l_0}\right)$$

where k is a stiffness parameter and ϵ_l is a strain parameter assumed to be 0.03.
In the rest of the work, since the main objective is to determine the geometry of the tibio-femoral contact, the ligaments will be considered as additional elements and a precise study

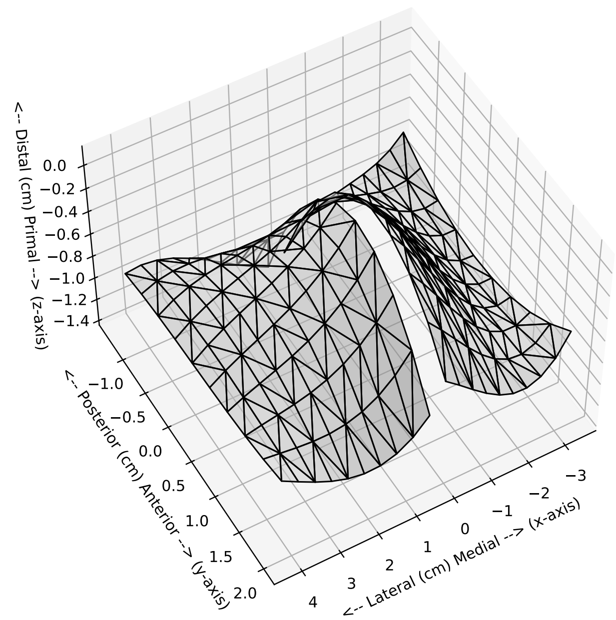

Figure 2.6: Tibial polynomial surfaces (degree 3 in x and y) fitted to the medial and lateral tibial condyles.

of these complex structures will not be possible. Adding them to one of the models can be done by imposing an additional constraint. Typically, in Chapter 5, a point on the femur and a point on the tibia must be connected by a constant distance, and the principle of Lagrange multipliers explained above in Section 1.3.1 will be used.
The positions of the ligament attachment points for the different models used, and their lengths, are listed in Appendix B.

Chapter 3

Detection of Contact

As explained in the previous chapter, the tibio-femoral contact is initially considered as two spheres with two planes. To refine the model, meshes are created to analyse this contact and then the mesh obtained from real scans will be used. In this chapter, we will discuss the meshes and algorithms used to detect this contact. The latter will provide crucial information for calculating the forces between the two bodies.

3.1 Meshes

The meshes used are grouped into three parts: those for planes, those for spheres and those for real tibia/femur.

3.1.1 Plane

To represent the plane, a simple "box" is created using the PyGmsh library [19]. The objective is to construct a rectangular parallelepiped, with one face designated as the plane assumed to be in contact with the spheres. The rest of the shape is mainly used to determine the collision depth with the other meshes.

The number of elements in this mesh has no impact on the accuracy of the results, as demonstrated by the algorithm explained in the following section. Consequently, a mesh with a reduced number of elements is employed to optimise performance and time. On the other hand, the dimensions of the rectangular parallelepiped will be exaggerated in order to guarantee comprehensive detection.

3.1.2 Icosphere

To represent spheres, we are using icospheres, which are polyhedral spheres made up of triangles. There are three different libraries for creating icospheres: PyGmsh, Gmsh [20] and the Trimesh library [21]. As shown on Figures 3.1 and 3.2, a large number of triangles is needed to correctly approximate a sphere.

This is confirmed by Figure 3.3, where the volume very quickly approaches the theoretical

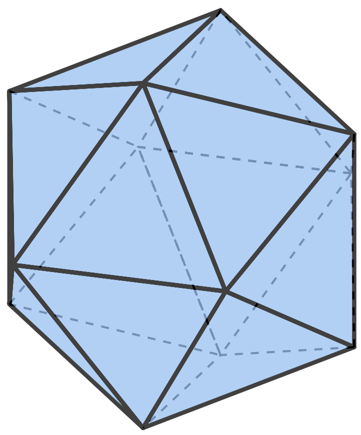

Figure 3.1: Theoretical Icosahedron: Icosphere with 20 faces.

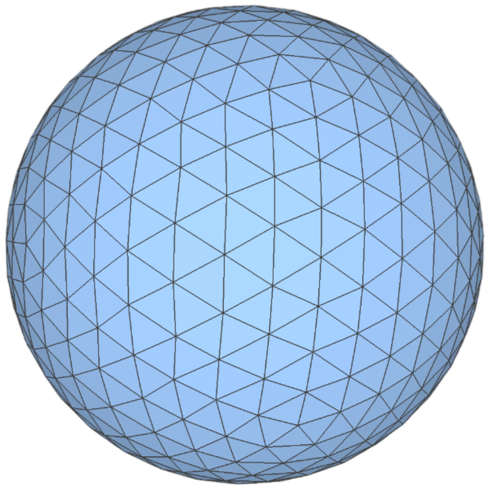

Figure 3.2: Icosphere created by PyGmsh with 1280 faces.

volume of the perfect sphere. There is also a green area representing a 0.5% error. It's considered to be accurate enough to give significant results.

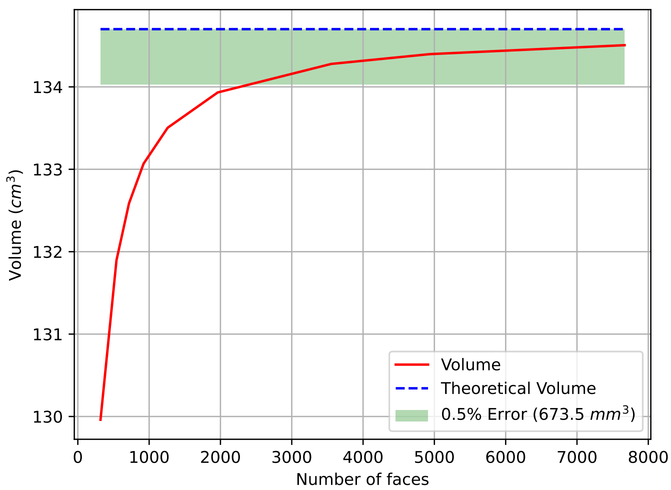

Figure 3.3: Convergence of the volume of the icosphere as the number of subdivisions increases for the Gmsh and PyGmsh libraries. (raduis = 3.18 cm which corresponds to that used to represent the lateral condyle).

3.1.3 Tibia/Femur

For the meshes of the tibia and femur, the in vivo data from a 29-year-old woman (mass = 70 kg, height = 170 cm) is employed [22, 23]. The geometries were derived from magnetic resonance images (MRI) and transcribed into binary STL[1]. Figure 3.4 represents a schematic representation of this reconstruction.

[1]STL is a file format native to the stereolithography CAD software created by 3D Systems. It is the file format that allows to store meshes.

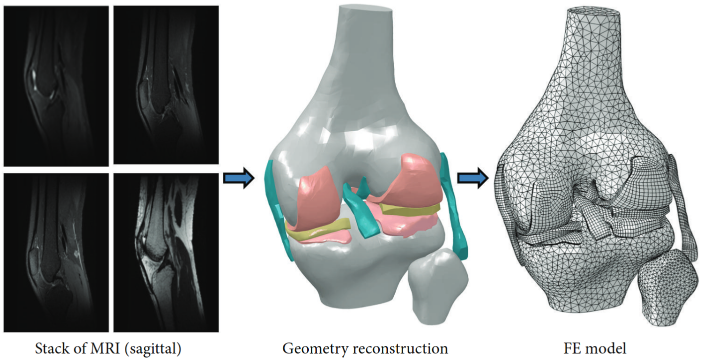

Figure 3.4: A schematic representation of geometry reconstruction from MRI data and FE mesh generation. Figure borrowed from [24].

This STL file has been transformed into the position and orientation used throughout this thesis. In Appendix B.3, the two meshes used are visualised. Given the considerable size of the meshes, it is also necessary to cut them in order to obtain meshes containing only the part that will be in collision. For example, as the only contact of interest in this study is the tibio-femoral contact, the head of the femur is not required in the mesh. Additionally, for clarification, the top of the tibia will also be divided into a lateral part and a medial part to obtain, for example, the plane equations presented in Figure 2.5.

3.1.4 Meshes Properties

Here are the main characteristics of the meshes used for collision testing :

- ***Euler Number*:** This characteristic can be employed to detect connectivity errors, check part of the validity of the mesh, etc.
  It is calculated by the formula :
  $$\chi = V - E + F \tag{3.1}$$
  where V is the number of vertices, E is the number of edges and F is the number of faces. χ is equal to 2 for all polyhedra that follow the topology of a sphere, whether convex or not.

- ***Winding Consistency*:** This criterion provides the sequence of vertices that comprise a given face. If it is true, the face is rotated in the clockwise direction, otherwise it is rotated in the opposite direction.
  This indicates whether it is oriented towards the outside of the mesh or the inside. Given that the normal of a face is a vector perpendicular to the surface, it can be calculated from the vector product of the edges formed by the vertices.

- ***Convexity*:** Check whether a mesh is convex. A mesh is convex if, for each pair of points in the mesh, the line segment connecting them is also in the mesh. More formally, a mesh is considered to be convex if and only if the straight line between two arbitrary points in the mesh never passes through a face (or part) of the mesh.

- ***Water-Tight***: Check if a mesh is watertight by making sure every edge is included in two faces. This allows to check whether the mesh is composed of a single closed surface or not.
- ***Empty***: Simply check whether the current meshes have defined data. This is the least important criterion, but it can sometimes correct stupid errors.

	Plan	Icosphere		Tibia/Femur	
		Gmsh/PyGmsh	Trimesh	Split	Total
Euler Number	2	2	2	2	2
Winding consistency	True	True	True	True	True
Convexity	True	False	True	False	False
Watertight	True	True	True	False	True
Empty	False	False	False	False	False

Table 3.1: Characteristics of the meshes used.

Table 3.1 lists the characteristics of the different meshes used. The characteristic that will most influence the algorithm will be the convexity of the mesh, which will be discussed and explained in the following sections.

The icospheres generated with Gmsh/PyGmsh are not convex. This does not seem correct, as a sphere is convex. This is due to a numerical error. Indeed, considering S the mesh generated with PyGmsh with points p_i for $i = \{1, 2, \ldots, M\}$ and its convex hull H[2] with points q_j for $j = \{1, 2, \ldots, M\}$.
The difference between the volumes of S and H is equal to $0.04mm^3$, for an icosphere S of volume $V = 69.3cm^3$, which corresponds to a relative error of 0.00006%. S is almost convex, but is concave. This allows us the opportunity to choose between concave and convex spheres for the rest of the work.

3.2 Collision Algorithm

This section will present a review of the stages involved in the detection of collisions between two meshes in physical simulation and 3D graphics applications. The main objective is to identify the elements in contact between the meshes, as well as their penetration distance. This will enable the calculation of the forces to be applied to the elements of these meshes at a subsequent stage.

To achieve this, an algorithm will be employed from the Trimesh library, which itself utilises fcl-python (Flexible Collision Library)[25], an C++ library for performing proximity and collision queries on pairs of geometric models and therefore meshes, in an optimal way.
This algorithm consists of two main steps: *Broad Phase* and *Narrow Phase*.
The broad phase searches for all bounded volume (BV) overlap, while the narrow phase asks whether the bounded objects actually overlap [26]. This is essentially a coarse-fine search. While the broad phase reduces all object pairs to a small set of potential collisions, the

[2]The convex hull of a set of points is the smallest convex polyhedron that contains all the points in the set.

narrow phase performs the actual overlap tests. Without the broad phase, the narrow phase would be infeasible, hence its importance. This separation also encourages code reuse, as the broad phase can be used as is for any set of objects that can be bounded, and if precision is not an issue, the narrow phase can be simplified or even omitted.

3.2.1 Convex vs Concave Meshes

Before going into details about the algorithm and the two main phases, fcl-python makes a very precise distinction between convex and concave objects.

In the case of convex objects, the entire volume of the mesh is taken into account, encompassing both the elements and the interior space between them. In the case of concave objects, the algorithm considers only the elements of the mesh.
To understand, with a simple example, in two dimensions, the difference between a circle and a disk is that the disk is full (it has a surface) but the circle is empty. Here it is the same principle, where disks are convex meshes and circles are concave ones.

This distinction is of great consequence for future developments, as it will significantly impact the algorithmic approach and, moreover, the selection of the mesh for spheres. Depending on whether the algorithm is designed to consider the entire volume or just the surface of the sphere, the mesh will be chosen accordingly.

3.2.2 Broad Phase

The aim of this phase is to reduce the number of potentially colliding elements. There are several techniques for achieving this, including Sweep-and Prune, KD-Tree, Bounding Volume Hierarchies (BVH), etc,... These and other main techniques are explained in more detail in [27]. In computer science, this phase is also called the box intersection checking problem [28].

Bounding Volume Hierarchies (BVH)

The present study focuses on the analysis of bounded volume hierarchies, which can be defined as a tree-like structure created over a set of geometric objects. All the geometric objects constitute the leaf nodes of the tree, which are enclosed in bounding volumes. These nodes are then organised into smaller groups and surrounded by larger bounded volumes. This process continues recursively, with these larger volumes being grouped together and enclosed within even larger volumes. The end result is a tree-like structure with a single encompassing volume at its top.
When using meshes, the set of geometric objects are the elements of the mesh. Figure 3.5 shows a simple example of the construction BVH for a 2D mesh. To sum up, the BVH is a tree structure where

- Each leaf contains an element
- Each internal node contains a BV which contains all the elements of its children.
- The root contains a BV containing all the elements of the mesh.

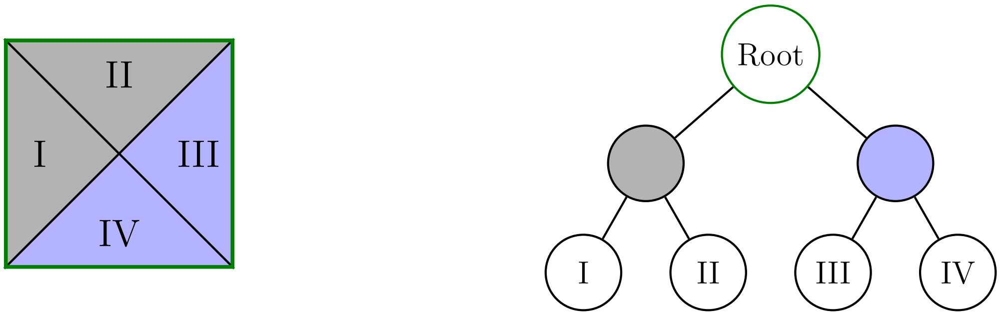

Figure 3.5: Example of BVH for a simple mesh.

Different Bounding Volumes

Once each tree has been built for each object, any potential collision between the two objects can be detected, but first it must be determined how the elements are to be enclosed. There are several types of boundary volume. Here are a few examples (Fig. 3.6).

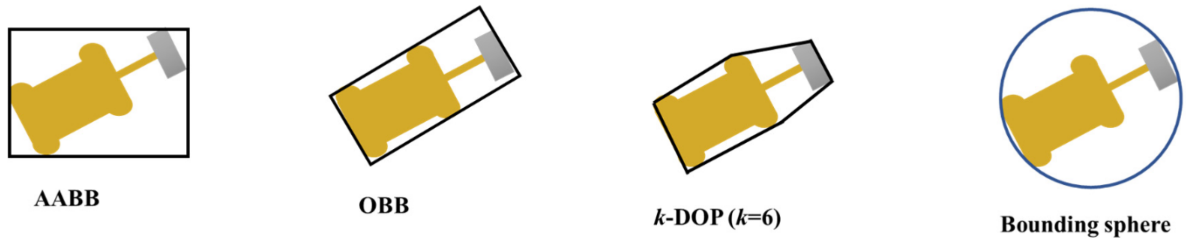

Figure 3.6: Different bounding boxes for an arbitrary object from [29].

AABB (Axis Aligned Bounding Box) is selected, which is a box whose edges are parallel to the coordinate axes.
Figure 3.7 represents an example of BVH using the AABB principle.

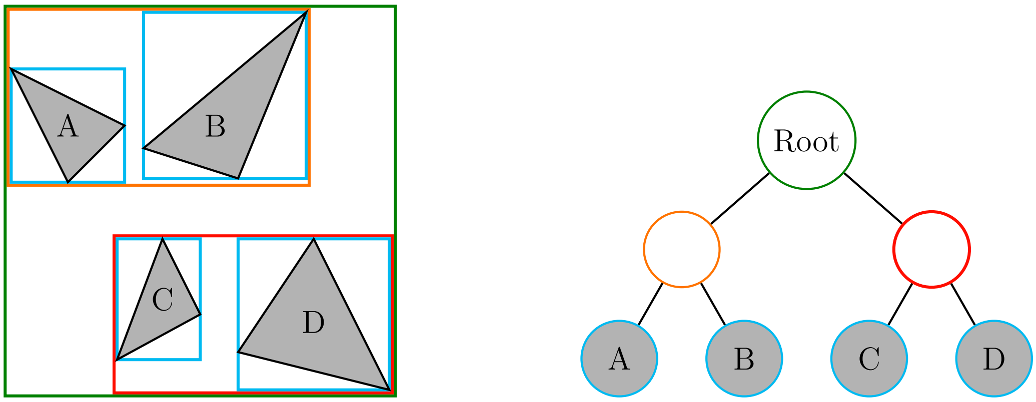

Figure 3.7: An example of a BVH using AABB with simple triangles.

The AABB principle represents a efficacious methodology for the generation of a bounded volume. The construction of an AABB volume is a relatively simple process, requiring only the input of the minimum and maximum points of the object in question. The two points may be employed for the inclusion of any object. The following example demonstrates the application of the AABB principle to a two-dimensional star (see Fig. 3.8).

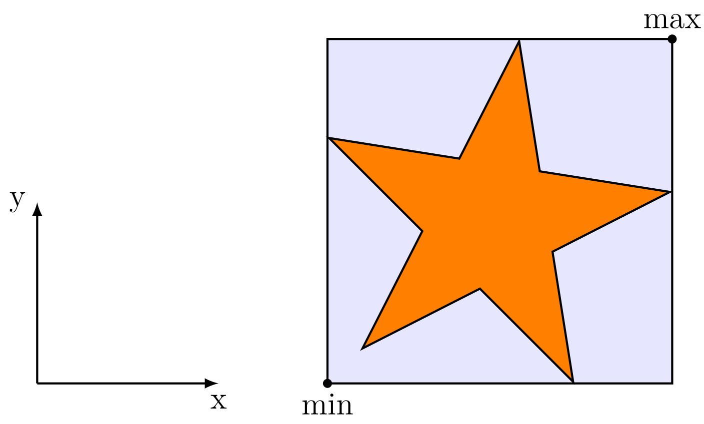

Figure 3.8: Example of AABB volume for any object in orange and its enclosing volume in blue.

The same principle can be applied in three dimensions to determine whether one AABB volume overlaps another. The following two points, which constitute each AABB, can be defined as follows:

- For the first AABB: $(\min A_x, \min A_y, \min A_z)$ and $(\max A_x, \max A_y, \max A_z)$
- For the second AABB: $(\min B_x, \min B_y, \min B_z)$ and $(\max B_x, \max B_y, \max B_z)$

In order for there to be an overlap, it is necessary that all of the cases represented by equation 3.2 are satisfied.

$$\begin{cases} \max A_x \geq \min B_x & \text{and} & \min A_x \leq \max B_x \\ \max A_y \geq \min B_y & \text{and} & \min A_y \leq \max B_y \\ \max A_z \geq \min B_z & \text{and} & \min A_z \leq \max B_z \end{cases} \tag{3.2}$$

This can be achieved in a relatively short time by checking whether two AABBs overlap, which can be done in $\mathcal{O}(1)$. Figure 3.9 illustrates this concept.

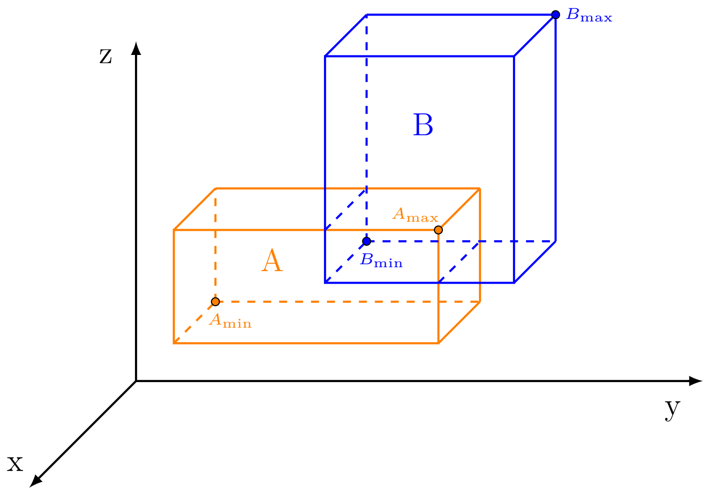

Figure 3.9: AABB overlap detection between two boxes in 3D.

Now that the structure is in place, the next step is to check whether there is a possible collision between the two meshes. Starting with the roots of each tree, test whether the root bounding boxes overlap. If they do not overlap, there is no collision. If they overlap, the bounding boxes of the children of the roots are then checked. This process is continued, level by level, down to the leaves of the trees. If the leaf boxes overlap, there is a potential collision. This potential collision initiates a more precise verification phase to determine whether the objects are really in collision.

Figure 3.10 shows an example of the application of a broad phase using the BVH principle with AABB overlap detection. This phase allows us to eliminate a large number of elements. But it also results in potential collisions that are not included, such as element C (Fig. 3.10). This shows that, as well as providing information of interest, the next (narrow) phase enables to check for real collisions. Note that for more details, Appendix D.1 provides pseudo code for the broad phase.

3.2.3 Narrow Phase

The narrow phase is the second part of the collision detection algorithm. It is used to determine whether two objects that have been identified as potentially colliding in the broad phase are actually colliding.
In order to facilitate comprehension of this phase, it is first necessary to familiarise oneself with two fundamental concepts : the Minkowski difference and the support mapping [30].

Minkowski Difference

The Minkowski difference is a mathematical operation. Given two sets A and B, this difference is represented as

$$A \ominus B = \{\mathbf{a} - \mathbf{b} \mid \mathbf{a} \in A, \mathbf{b} \in B\} \tag{3.3}$$

This means that this difference is a set that includes all the vectors obtained by subtracting a vector from set B from a vector from set A. The advantage of this set is that if the set obtained by the Minkowski difference contains the origin, it can be concluded that the sets A and B overlap (Fig 3.11). Conversely, if the set does not contain the origin, it can be deduced that the two sets do not overlap.

The construction of Minkowski difference set requires $2NM$ subtractions where N and M are the number of vertices in each respective shape, which is significant. This leads to the next concept.

Support Mapping

The support mapping $s_A(\mathbf{d})$ of a set A is a function that returns the extreme point in the set in a given direction $\mathbf{d}$. An useful property of the support mapping is:

$$\mathbf{d} \cdot s_A(\mathbf{d}) = \max\{\mathbf{a} \cdot \mathbf{d} \mid \mathbf{a} \in A\} \tag{3.4}$$

Figure 3.12 represents an example of the support mapping for two convex shapes.

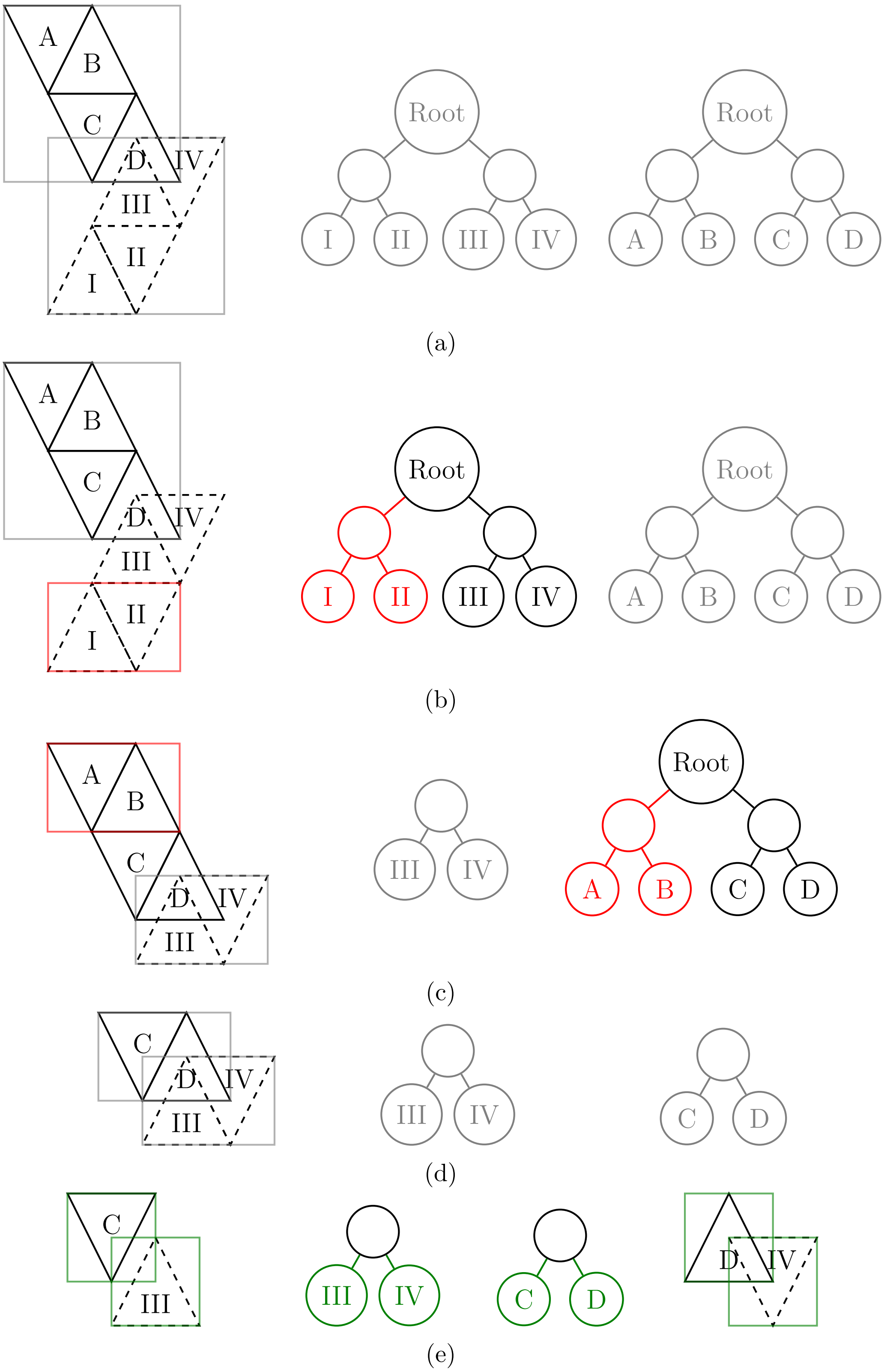

Figure 3.10: Example of the application of the broad phase for two simple meshes (A,B,C,D) and (I,II,III,IV). a) Once the BVH of each mesh has been constructed, a check is first made to see if the total BV (root) of each mesh overlaps. b) Then start exploring the first BVH by taking the first child. I and II are not in contact, since they do not overlap the BV of the root of the other mesh. c) Same process with the first child of the other mesh. A and B are not in collision. d) The process continues until the leaves of the tree are reached. e) On reaching the leaves, the BV of III collides with that of C. The BV of D collides with that of IV.

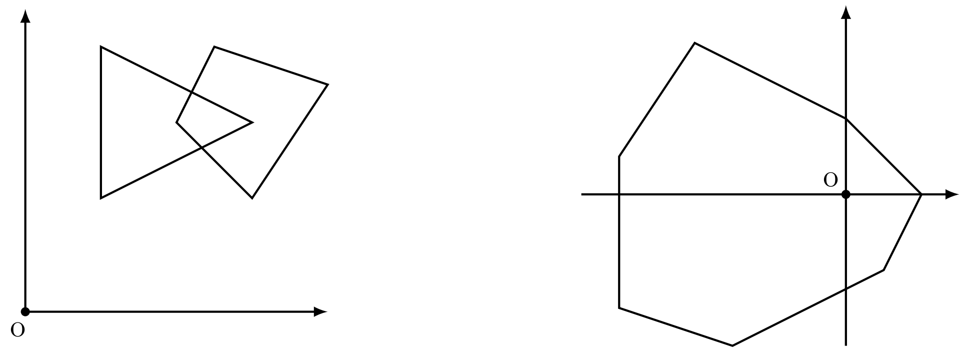

Figure 3.11: Two-dimensional example of the Minkowski difference. On the left, two intersecting convex shapes. On the right, the Minkowski difference, which includes the origin.

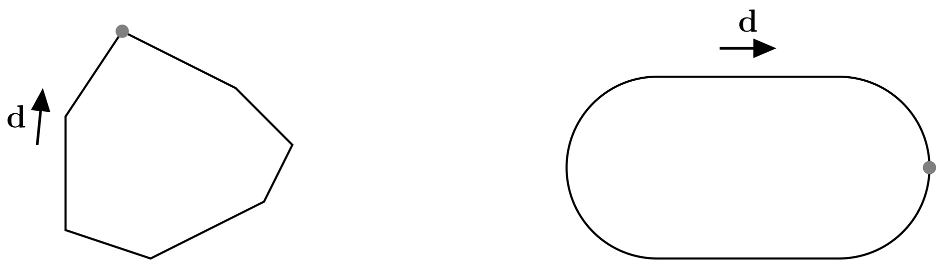

Figure 3.12: Support mapping for two convex shapes. The arrows indicate the search direction **d** and the grey points are the corresponding extreme points.

By deriving equations 3.3 and 3.4, a connection between the Minkowski Difference and the support mapping gives the following property:

$$s_{A\ominus B}(\mathbf{d}) = s_A(\mathbf{d}) - s_B(-\mathbf{d}) \tag{3.5}$$

The advantage of using equation 3.5 is that it is no longer necessary to calculate the entire Minkowski difference in order to be sure that it contains the origin.

GJK Algorithm

Based on the two concepts explained above, the narrow phase includes the GJK (Gilbert-Johnson-Keerthi) algorithm, which is a very efficient algorithm for detecting collisions between convex objects [31].
The principle of this algorithm is to identify a simplex that encompasses the origin of the Minkowski difference between the two objects. If the GJK algorithm succeeds, this means that there is an overlap. If it fails to construct a simplex, it means that the objects are not in contact.

In order to facilitate comprehension, Figure 3.13 demonstrates how the algorithm can be used in two-dimensions, using the example in Figure 3.11. In two-dimensions, the GJK algorithm must construct a three-point simplex (a triangle) to enclose the origin.

Algorithm 1 describes the GJK for three-dimensions. In three-dimensions, it is necessary to create a tetrahedron, which requires four points. When these are found there are two options. The first is that the origin is inside, so the GJK while loop is terminated. The second is that the tetrahedron does not contain the origin, so the update function (line 18)

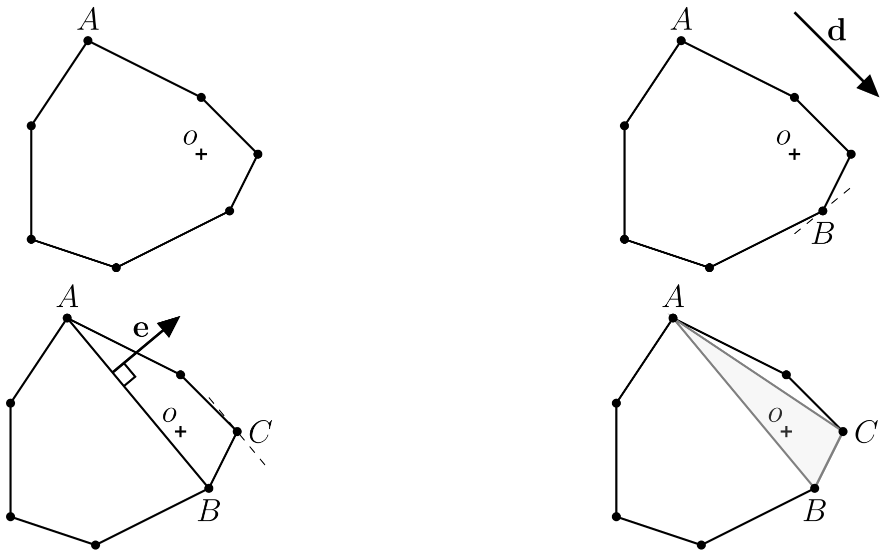

Figure 3.13: GJK algorithm in two-dimensions. The initial random point of the Minkowski difference is A. By looking for a support point in the random direction $\mathbf{d}$, the second point B is found. The third point C is added by looking at the support point found from the direction $\mathbf{e}$ orthogonal to $\overline{AB}$ in the direction of the origin. In two dimensions, only one triangle is needed to enclose the origin, and in this case triangle ABC encloses the origin.

Algorithm 1 GJK Distance Algorithm

function GJK_Distance(s_A, s_B)
    $A \leftarrow$ any point in $A \ominus B$
    $\mathbf{d} \leftarrow$ random direction
    $B \leftarrow s_{A \ominus B}(\mathbf{d})$
    $\mathbf{e} \leftarrow$ orthogonal direction to $\mathbf{d}$
    $C \leftarrow s_{A \ominus B}(\mathbf{e})$
    $simplex \leftarrow \{A, B, C\}$
    $\mathbf{f} \leftarrow (B - C) \times -C \times (B - C)$
    while True **do**
        $D \leftarrow s_{A \ominus B}(\mathbf{f})$
        if Dot($D, \mathbf{f}$) < 0 **then**
            return false
        end if
        $simplex$.append(D)
        if Contains_Origin($simplex$) **then**
            return true
        end if
        $\mathbf{f} \leftarrow$ updateSimplexAndSearchDirection($simplex$)
    end while
end function

tries again to create a new simplex that contains the origin. If, at any point in the while loop, the new support point has a negative dot product with the current search direction (lines 11–13), the GJK while loop is also terminated, as it can be concluded that the origin cannot lie inside the Minkowski difference.

All this is explained in more detail in [32], where he uses the algorithm to find the minimum distance between two shapes and if the two shapes collide, he returns 0.

EPA Algorithm

Now the next step is to solve the contact parameters, such as penetration depth, contact normal and contact point. This is achieved using the *Expanding Polytope Algorithm (EPA)* [33].

EPA is closely related to GJK, in that the EPA algorithm starts with the termination simplex of the GJK algorithm. EPA expands this simplex in the direction of the feature (such as an edge or triangle) closest to the origin among the colliding objects. This expansion is iterative and continues until the algorithm finds the feature closest to the true collision surface. Once the EPA has found the closest feature, it calculates the associated contact normal and penetration depth.

Figure 3.14 presents each step in a two-dimensional example. In three-dimensions, the algorithm follows the same principle. The only difference is that the feature is not an edge but a triangle. For more details, Algorithm 2 uses the pseudocode of [30].

Algorithm 2 Expanding Polytope Algorithm (EPA) for finding the penetration depth and contact normal.

```
procedure EPA(s_A, s_B, simplex)
    initialize the EPA polytope with the terminating GJK simplex
    while True do
        find the feature closest to the origin
        if |closestDistance − oldclosestDistance| < tol then
            penetrationDepth = closestDistance
            normal = GetNormal()
            break
        end if
        UpdateSearchDir()
        getNewSupportPoint(s_A, s_B)
        removeOldTriangles()
        updatePolytope()
    end while
end procedure
```

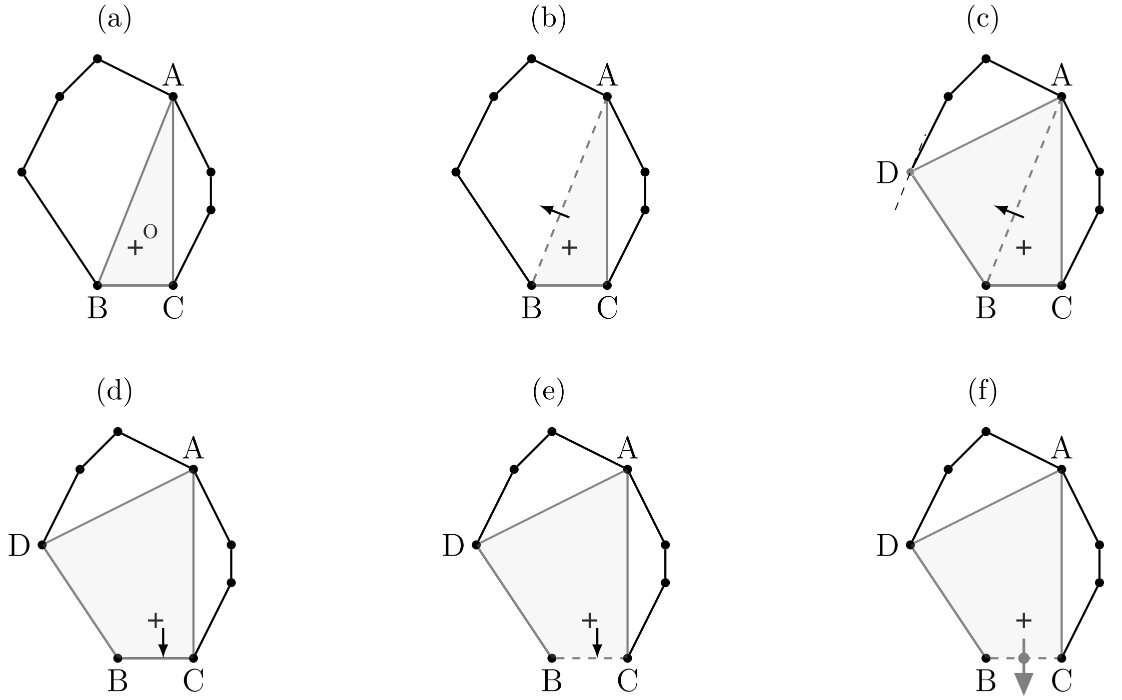

Figure 3.14: Example of EPA algorithm in two-dimensions. (a) The initial simplex (grey) containing the origin obtained by GJK algorithm. (b) In two-dimensions, the nearest face is the dotted edge of the triangle. (c) A new support mapping point D is found in the normal direction. (d) From D, two new edges are created so that the polytope is closed again. (e) A new closest edge is found (dotted grey line segment). (f) This new closest edge turns out to be the closest element on the shape of the Minkowski difference. The contact normal and penetration depth can now be calculated.

3.2.4 Validation

This section will present the results of a number of tests designed to validate the collision algorithm and to evaluate the data that can be extracted from these collisions.
In addition, the importance of convex and concave meshes will be examined in detail. There are three potential categories of collision: *Convex - Convex*, *Convex - Concave* and *Concave - Concave*.
As a reminder, in Section 3.2.1, convex meshes are considered as whole volumes, whereas the contour is only considered for the concave ones.
Figure 3.15 sets out the two-dimensional examples with simple shapes, as well as some important differences.

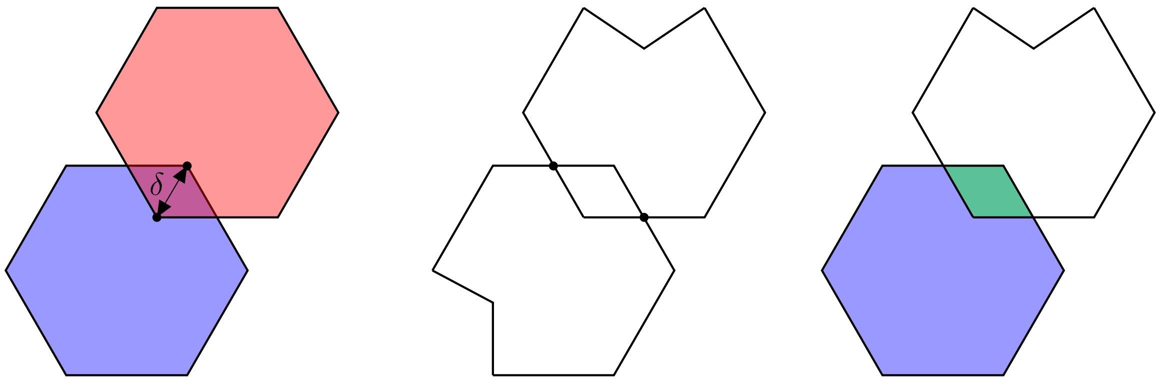

(a) Convex-Convex (b) Concave-Concave (c) Convex-Concave

Figure 3.15: Example of the difference between the three different types of collision. (a) In the Convex-Convex case, the two shapes are considered full, their maximum penetration δ is found. (b) For the Concave-Concave case, two collision points are obtained, both with lengths close to 0. (c) In this case, there is a collision surface between the two shapes.

Convex - Convex

The first case examined is that of a collision between two convex meshes. In Figure 3.15a, assuming there is a collision of both meshes, the distance will be found between the two entire objects, but not really by the elements themselves. This means that there will only be one collision, that of maximum depth distance.

Concave - Concave

In the case of a collision between two concave meshes, as explained above, only the elements of the mesh are taken into account. The elements of the first mesh that are in contact with the elements of the second mesh will be identified.
The concept of penetration depth will not be applicable in this instance, as the elements will be in direct contact with one another. In the two-dimensional case, this contact will be made by points (see Fig. 3.15b). However, in three-dimensions, these will be areas of contact. Figure 3.16 displays the collision between two spheres generated by PyGmsh, which are assumed to be concave (see Table 3.1).

Figure 3.17 indicates the areas of contact resulting from the collision. There is no real contact surface and no notion of depth, which will cause a problem for the calculation of forces in Chapter 4.

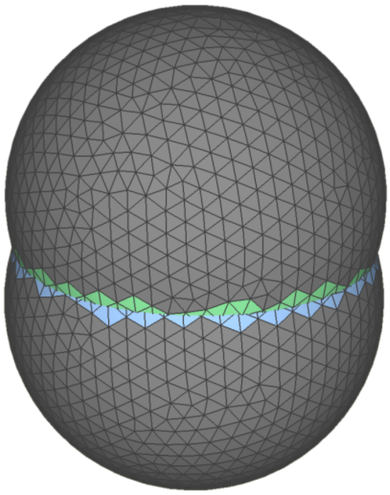

Figure 3.16: Example of a Concave-Concave collision with two spheres generated by PyGmsh.

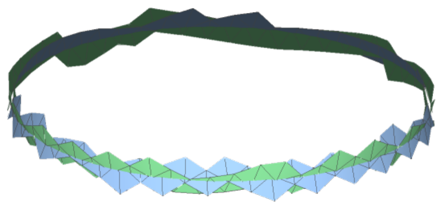

Figure 3.17: Result of the Concave-Concave collision. The green part belongs to the upper sphere and the blue part to the lower one.

Convex - Concave

In the last case, it is the contact between a convex mesh and a concave mesh.
All the information required can be found. This is due to the fact that a mesh which only considers external elements collides with a mesh which considers the entire object (see Fig. 3.15c). For each element of the concave mesh, it is possible to find the index of the element, the depth, the point of contact and the normal of contact, when the element is in collision. Figure 3.18 illustrates this case.

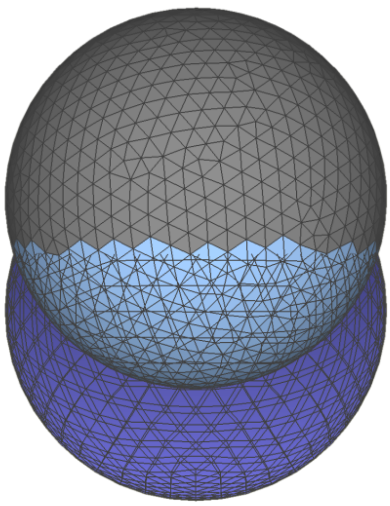

Figure 3.18: Example of a Convex-Concave collision with a sphere generated by PyGmsh (top) and a sphere generated by Trimesh (bottom). The blue area is the contact area.

To summarise the three cases, depending on the mesh geometry, different results are obtained, as indicated in Table 3.2.

	Benefits	Drawbacks
Convex-Convex	Maximum depth	Only one element is in contact
	Good normal/point for maximal depth point	Only for this point
		No face index
Concave-Concave	Correct face index	Two collision surfaces: one for each mesh
	Correct normal/contact for only surfaces found	No good depth
		No real collision surface
Convex-Concave	Good collision surface	
	All information is good here	

Table 3.2: Summary of the benefits and drawbacks of different collision scenarios.

After these explanations, we try, as far as possible, to combine a concave mesh with a convex mesh. Note that for spheres, with the numerical error explained in Section 3.1.4, it is possible to represent them concave and convex without losing their geometry.
The following analyses will be based on the case where a concave mesh is in contact with a convex one. A sphere is cut by a plane into two identical parts. The radius of the sphere is $3.18cm$, which corresponds to the approximation of the lateral femoral condyle. Figure 3.19 is an example of the phenomenon of contact surface overestimation as the number of faces in the icosphere increases.

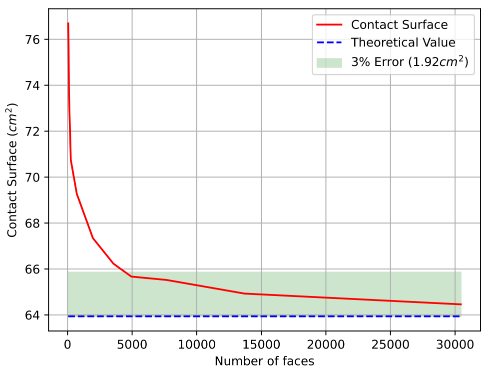

Figure 3.19: Contact surface between the concave icosphere and the convex rectangular parallelepiped.

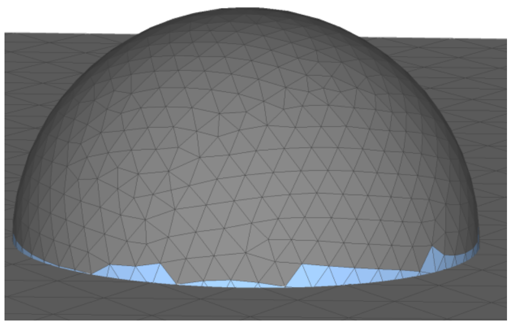

Figure 3.20: Representation of collision meshes for analysis, based on an icosphere with 2268 faces. In blue, the faces that are considered to be collisions, but for which part of their area is not.

Figure 3.20 suggests that the overestimation of the contact area is due to the error of considering the total area of the elements in collision, whereas some of them only display part of their surface actually in contact.

Using the same test, the execution time of the detection algorithm as a function of the number of icosphere faces is mainly linear (Fig. 3.21). Note that the number of faces increases up to approximately $250,000$. In our case, this is not realized, but it is to reveal for values of $\pm 200,000$ faces, the execution time does not increase in the same way. This is due to the fact that the algorithm imposes a maximum of $100,000$ possible contacts during the narrow phase. The remaining increase is due to the broad phase. This also means that the broad phase is faster than the narrow phase. The dotted lines have been calculated by linear regression and are presented to demonstrate the linearity of the algorithm execution.

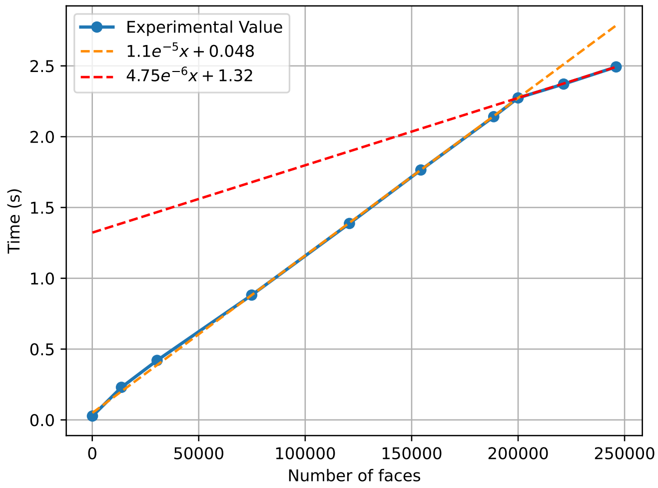

Figure 3.21: Execution time of the collision detection algorithm as a function of the number of faces in the icosphere, for the collision of a single icosphere with a plane that bisects it.

It should be noted that an additional robustness test was conducted using non-watertight meshes, which were typically split femur/tibia meshes. As a reminder, watertight corresponds to a mesh that is not closed, i.e. there is an edge that is not included in two faces. This does not change the results obtained.

To conclude, the collision algorithm is extremely precise and very fast.

3.3 Master-Slave Contact

As explained in the previous section, there should be a collision between a convex mesh and a concave mesh. All the information relating to the collision will be based on just one of the meshes. In fact, the index, contact point, penetration depth, etc. will be calculated for each element of the concave mesh in relation to the contact with the convex mesh.

In order to align with the existing literature, this can be seen to correspond to the concept of master-slave contact, which is much used in contexts where two surfaces interact with each other through the implementation of displacement-based finite elements. For example, [34] adopts this approach to find the sliding contact on beams instead of using the Lagrange multiplier method.

Both terms can be defined as follows:

- *Master surface* : It is the surface that directs or influences the interaction. For example, it can simulate realistic contact, including phenomena such as crushing or sliding.
- *Slave surface* : It is the surface that follows or reacts to the interaction. For example, the position and forces on the slave surface will be adjusted according to the constraints

imposed by the master surface.

In the present case, the convex mesh is designated as the master mesh, and the concave mesh is designated as the slave mesh. For the rest, the different models, examined in Chapter 5, will not all be possible with a master-slave contact. In fact, when the real femur and tibia meshes are used, they will be two concave (slave) meshes. This poses a problem. There are several ways of solving it. One potential solution is to transform the concave mesh into a convex one. The application of functions such as convex-hull to render convex meshes would result in an unacceptable loss of precision. Furthermore, the division of the mesh into multiple convex sub-meshes does not produce the same rendering results as expected. It is necessary to employ an alternative algorithm: *Ray Casting Algorithm*.

3.4 Ray Casting Algorithm

The principle of this algorithm is to check, for each vertex of the slave mesh, whether or not this point is inside the master mesh, and then if so to calculate its depth distance.

3.4.1 Algorithm Description

In two-dimensions, this algorithm consists of casting a ray in any direction, starting from the point of interest and counting how many times the ray intersects the polygon.
Figure 3.22 demonstrates that if the point is outside the polygon, the ray will cut its edge an even number of times. If the point is inside the polygon, it will intersect the edge an odd number of times.

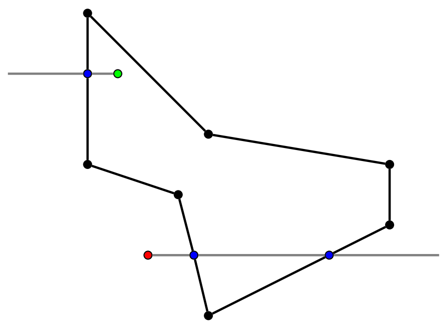

Figure 3.22: Example of the Ray Casting algorithm in 2D. The red point is outside the polygon, the blue points are the intersection and the green point is inside.

Using the same principle in three-dimensions, the points in the mesh can be found (Algorithm 3).

Lines 3–7 check whether the points belong to the volume of AABB. This verification corresponds to the broad phase (see Section 3.2.2). After this, the ray in an arbitrary direction is launched forwards and backwards and a series of tests are performed :

1. *Count_nb_hits()* : Count the number of times the ray hits the mesh in both directions.

2. *Count_nb_contains()* : Check whether the number of hits is even or odd.

Algorithm 3 Ray Casting : Check if a mesh contains a set of points

```
Function contains_points(mesh, points)
contains ← array of booleans of size points
for point ∈ points do
    if not point ∈ AABB(mesh) then
    contains(point) ← False
    end if
end for
ray_directions ← arbitrary directions
Agree ← False
while not Agree do
    rays ← cast rays from points inside the AABB
                in both forward and backward directions
    Count_nb_hits()
    Count_nb_contains()
    Agree, ray_directions ← Check_agree()
end while
return contains
```

3. *Check_agree()* : Check whether the Count_nb_contains is the same in both directions.
   - If it is identical, contains is defined as a function of Count_nb_contains and Agree is set to true, which let's it know whether the points are inside or not.
   - If it is not the same, the direction of the ray is considered broken, another direction is taken and agree is set to false to repeat the loop once more.

Note that if a ray does not touch the mesh, it is said to be in free space and its number of collisions is considered to be even. In addition, by using Check_agree, a special case is avoided. Indeed, since an arbitrary direction is used, it is possible to arrive at the case illustrated in Figure 3.23. The number of intersections in the forward direction may be even, whereas in the backward direction, it may be odd.

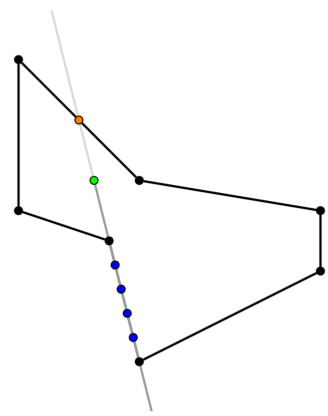

Figure 3.23: Special case where the ray passes through a side of the polygon. The point in orange is the intersection for the backward direction and the points in blue are the intersections for the forward direction.

The objective is not limited to determining whether the point is within the mesh; rather, it is to establish the precise location of the point within the mesh. Additionally, the depth distance must be calculated. An approach based on computational geometry is used, consisting mainly of spatial data structures such as KD trees [35].
From the point in the mesh closest to the point, the Euclidean distance is calculated.

A number of articles, such as [36] add a sign that depends on whether the point is inside or outside the mesh. In this case, as Ray Casting initially checks whether the point is inside, all distances are assumed to be positive and the distances of points outside the mesh are not even calculated.

3.4.2 Validation

In general, the algorithm works pretty well, but it is less robust than the Collision algorithm (see Section 3.2). Watertight meshes need to be used to ensure that the Ray Casting principle is valid. Since the ray could pass through these openings without detecting collisions with the mesh, the result would be distorted.

In addition, when a point is located on the contour of the mesh, it is detected randomly. In some cases, the point is considered to be inside the contour, while in others it is not. This random detection depends on the tolerance given to the penetration distance. Figure 3.24 shows that above $0.65\mu m$, the collision is sure to be detected. This value is too small to affect the results significantly, which is a good thing.

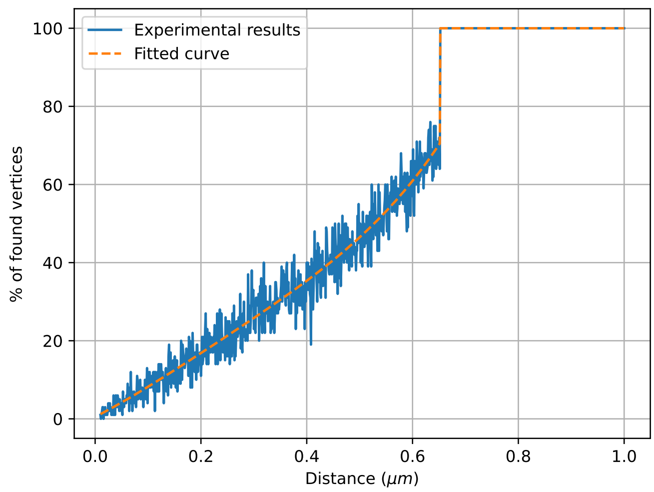

Figure 3.24: Percentage of found vertices as a function of the penetration distance. The penetration distance is the distance between the point and the edge of the mesh.

One element that will impact the model significantly is the execution time. Unlike the Collision algorithm described in Section 3.2, the Ray Casting algorithm is not linear but rather quadratic. Figure 3.25 verifies the result indicated by the dotted line, which was obtained through polynomial regression.

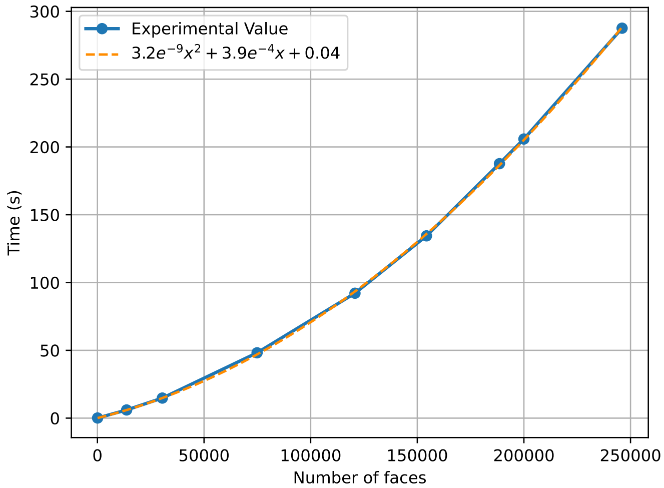

Figure 3.25: Execution time of the Ray Casting algorithm as a function of the number of faces in the icosphere, for the collision of a single icosphere with a plane that bisects it.

3.5 Conclusion

In conclusion, both algorithms offer very good performance. The first is faster and more accurate, but has limitations in some cases. The second, although slightly less accurate and slower, has negligible errors. It is therefore recommended that the first algorithm be used whenever possible.

Note that in Chapter 5, the application of the two algorithms to the same test will give results that are almost identical. However, there is a difference: two different results are obtained by taking a single vertex of the mesh in collision. In the first case, the common faces of the vertex are considered to be in contact, whereas in the other, only that vertex is considered to be in contact (Fig. 3.26). This is in line with Figures 3.19 and 3.20, which indicate the overrestimation of the collision algortihm. This is negligible, but if more precision were required, for example, it would be possible to increase the number of mesh elements considerably.

Figure 3.26: Particular case where only the blue vertex is in collision. On the left, the entire red surface is considered to be in collision, while on the right, only the blue vertex is in collision.

To conclude this chapter, Figure 3.27 gives a summary of each step in the contact detection phase between the two meshes. This diagram ends with the force/torque calculation, the subject of the Chapter 4.

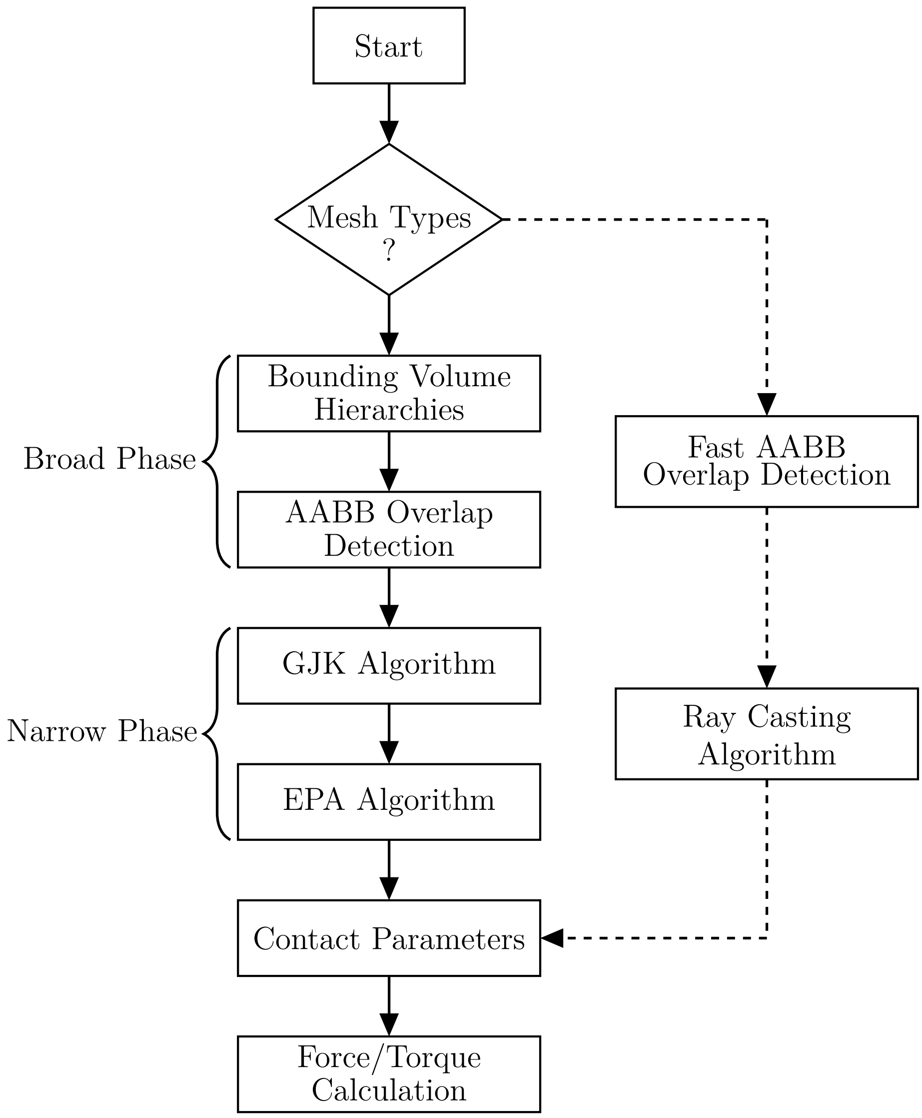

Figure 3.27: Flow diagram of the contact detection method. The continuous arrows represent the algorithm explained in Section 3.2 for Convex-Concave contact. If the mesh type is Concave-Concave, the alternative algorithm is represented by the dotted arrows.

Chapter 4

Contact Dynamics Modeling

The main objective of human motion modeling is to reproduce accurate motion, which is why contact dynamics is of particular interest. Contact dynamics models can be divided into discrete and continuous models [37]. Discrete models assume that contact takes place over a short period of time and that contact forces can be approximated as instantaneous impulses. Continuous contact models assume that the contact forces act continuously throughout the impact. Although computationally more complex the models are better adapted to intermittent and continuous contacts, multiple contacts and flexible bodies, which are common in biomechanical systems. This chapter will concentrate on continuous contact models, which are employed to simulate the knee joint.

4.1 Force Types

There are several types of contact force. In Brown's thesis [38], he describes some of them, such as Kelvin-Voigt, Hunt-Crossley (Hertz), elastic foundation, etc, ... The main forces studied here are shown in Figure 4.1. Note that elastic foundation is chosen as the baseline configuration for this model, and that the other types are more for comparison.

4.1.1 Elastic Foundation Models

In elastic foundation models, the contact surfaces are modelled as a layer of discrete springs on a rigid base (Figure 4.1a). These models are often used to represent contact between bones in the human body, for example in mathematical analyses of force transmission by [39] through the ankle joint.

[40] claims that the elastic foundation based on the knee is a fast enough model for certain optimisation studies. He assumes that the deformations only take place in the cartilage layer, which is treated as a simple elastic material. In our case, a spring is provided for each element of the contact surface.

Where there are springs, there is a stiffness constant. To determine the problem is simplified by considering that the contact surface is a first-order approximation of the relationship between the normal surface stress σ_n, which represents the pressure p, and the surface

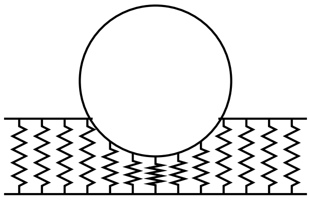

(a) Elastic Foundation

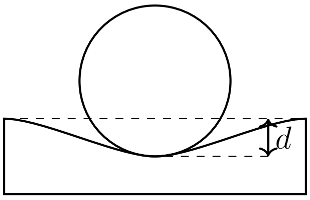

(b) Hertz

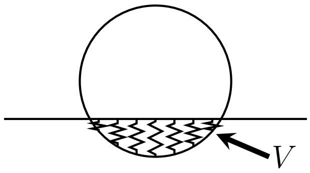

(c) Volumetric Forces

Figure 4.1: Overview of some contact models.

displacement d_n:

$$p = \sigma_n = k_n d_n \tag{4.1}$$

with

$$k_n = \frac{(1-\nu)E}{(1+\nu)(1-2\nu)h} \tag{4.2}$$

where E is the Young's modulus, ν is the Poisson's ratio, h is the thickness of the elastic foundation and k_n is the spring constant.

Note that d_n can be calculated at any time as a function of the current position and orientation of the tibia and femur. The baseline values are $E = 20\text{MPa}$ and $\nu = 0.3$. These values are inspired by [41], which looks at the sensitivity of the tibio-femoral response to modeling parameters. The order of magnitude is generally the same in other articles, such as that of [42], which analysed a variation of the contact pressure with different material parameters of menisci under a compressive load and an anterior tibial load.

The properties of the cartilage change greatly according to age, each individual and a number of other factors. For later analysis, E and ν will be considered as parameters to vary.

The thickness h of the elastic corresponds to the thickness of the soft layer of the knee, i.e the cartilage. The latter is estimated to be 6 mm in order to ensure maximum contact between the two bones. Figure 4.2 indicates the distribution of the cartilage.

It should be mentioned that equation 4.1 is strictly linear and is only valid for a small displacement of the surface. This deformation is the same as that applied by [44] in their two-dimensional model for the application of pressure to a joint.
For a larger displacement surface, the non-linearity of the relationship between surface normal

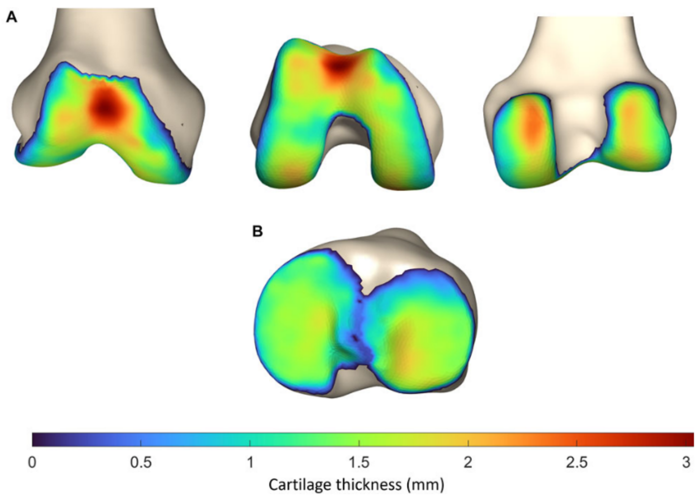

Figure 4.2: Representation of the specific cartilage thickness on (A) the femur, (B) the tibia. Figure reproduced from [43].

stress and surface displacement must be taken into account, as was done by [45]. However, we only focus on small deformations. It should also be remembered that for healthy human joints, friction is negligible, which eliminates the effects of shear forces.

Finally, after applying the collision algorithm explained in Chapter 3, each element in collision is known, as is all the information that needs to calculate the contact surface force. This expression is therefore available for each element e :

$$F_e = \sigma_e A_e = \frac{(1-\nu)E}{(1+\nu)(1-2\nu)} \frac{d_n}{h} A_e \tag{4.3}$$

where F_e, σ_e and A_e represent the force, stress and area of the element, respectively.
All that remains is to add up each element to find F the resultant force, A the area in contact and p the contact pressure. It can be demonstrated that the pressure and area are proportional to the distance between the surfaces in contact, which leads to the conclusion that the force is also proportional to the square of this distance.

4.1.2 Hertz Contact Theory

Unlike the elastic foundation model, the Hertz theory refers to the localised stresses that develop when two curved surfaces come into contact and deform slightly under the action of the applied forces (Fig. 4.1b). The degree of deformation depends on the elasticity of the material in contact, i.e. its modulus of elasticity. When considering the contact between a sphere and a plane, both of which are deformable, this theory provides two important approximate results:

1. The contact surface area increases in proportion to the depth of penetration. This phenomenon can be attributed to the geometry of the contact surface, which initially forms a punctual contact point and subsequently widens as the sphere descends. As the sphere sinks, its intersection with the initial plane forms a disk with a radius, a, that can be approximated by the following relationship: $a^2 \simeq Rd$.

2. Although the law of behaviour of the material is linear (Hooke's law), the relationship between the applied force F and the depth d is not: $F \propto d^{3/2}$.

where R is the radius of the sphere, and d is the penetration depth. This allows to determine contact pressure, contact force and pressure distribution.

The contact pressure p is given by the equation:

$$p = \frac{F}{A} = \frac{F}{\pi a^2} \tag{4.4}$$

The contact force is expressed as follows:

$$F = \frac{4}{3} E^* R^{1/2} d^{3/2} \tag{4.5}$$

where E^* is the effective Young's modulus, and is defined by the expression :

$$\frac{1}{E^*} = \frac{1-\nu_1^2}{E_1} + \frac{1-\nu_2^2}{E_2} \tag{4.6}$$

where E_1 and E_2 are the Young's modulus, ν_1 and ν_2 are the Poisson's ratios of the two materials, respectively. The pressure distribution is calculated as :

$$p(r_i) = p_0 \left(1 - \frac{r_i^2}{a^2}\right)^{\frac{1}{2}} \tag{4.7}$$

where $p(r)$ is the pressure distribution, r is the radial distance from the center of the contact area and p_0 is the maximum pressure :

$$p_0 = \frac{3F}{2\pi a^2} = \frac{1}{\pi}\left(\frac{6FE^{*2}}{R^2}\right)^{\frac{1}{3}} \tag{4.8}$$

Note that in geometry, the part of a sphere bounded by a plane is the spherical cap. Figure 4.3 serves to illustrate this concept. Using the Hertz method, the contact surface is represented by the base zone of the spherical cap (blue part). If an elastic foundation is used, the contact surface extends over the surface of the cap (red part).

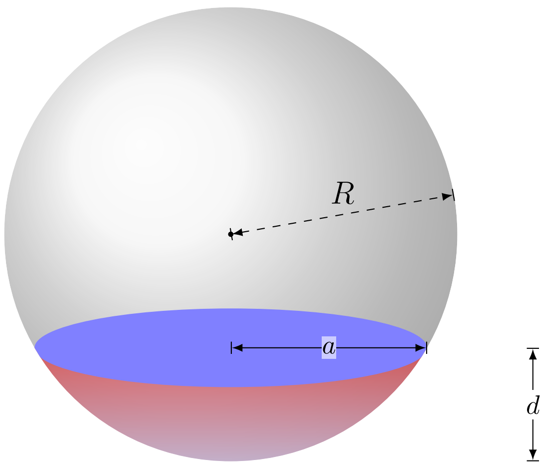

Figure 4.3: An example of spherical cap. The blue area represent the cap base area, and the red area represent the cap surface area.

Using the collision detection, the Hertz model is not the most accurate for modeling the contact between the femur and the tibia. For example, this model remains valid for fairly simple shapes, which will not be the final case. However, it is interesting to use it to compare results with other models.

Furthermore, the calculation of the contact force requires only a minimal amount of information, which is advantageous for rapid simulations. Indeed, simply calculating the maximum penetration d is sufficient to obtain an approximation of the contact force, and this is precisely the case if there is a Convex-Convex collision (reminder Table 3.2).

4.1.3 Volumetric Forces

The last case studied is that of volumetric forces (Fig 4.1c). The contact forces are represented by the following formula:

$$F_n = k_V V(1 + a v_{cn}) \tag{4.9}$$

where k_V is the volumetric stiffness, V is the volume of the contact area, a is the damping constant, and v_{cn} is the relative velocity of the two surfaces in the normal direction.
The volume of the contact area is given by:

$$V = \int_\Omega d\Omega = \underbrace{\frac{\pi}{3} d^2 (3R - d)}_{\text{for a spherical cap}}$$

where Ω is the contact area, and d is the penetration depth. Let's use k_V at $\simeq 1e^7 N/m^3$ and $a \simeq -1s/m$, since calculating the relative velocity takes a lot of calculation time, this case will not be studied extensively.

The proportion between the contact force F and the displacement d is not of degree 3/2 like Hertz but rather quadratic like the elastic foundation for small deformations, the relation is therefore $F \propto d^2$.

4.2 Discussion

In the rest of the thesis, meshes of $\simeq$ 5000 elements are generally used, and this is the case for the following discussion.
Figure 4.4 demonstrates the evolution of contact forces as a function of indentation for the three models. This graph is in logarithmic scale, which verifies the complexity of the different models. A slope of 2 is observed for the elastic foundation and for the volumetric forces, indicating that $F \propto d^2$. This is consistent with the predictions of Hertz, which suggest a slope of 3/2.

In the field of medicine, surgeons often refer to the concept of maximum pressure. Figure 4.5 shows the evolution of maximum pressure as a function of depth for the three models. Given that the contact surface is proportional to the indentation in all three models, with the proportionality constant equal to the ratio of the force to the surface area, it follows that the pressure is proportional to the ratio of the force to the depth. This relationship is expressed as proportionality to the indentation depth, d, for the volumetric forces and the elastic foundation. For Hertz, the proportionality is expressed as p proportional to the

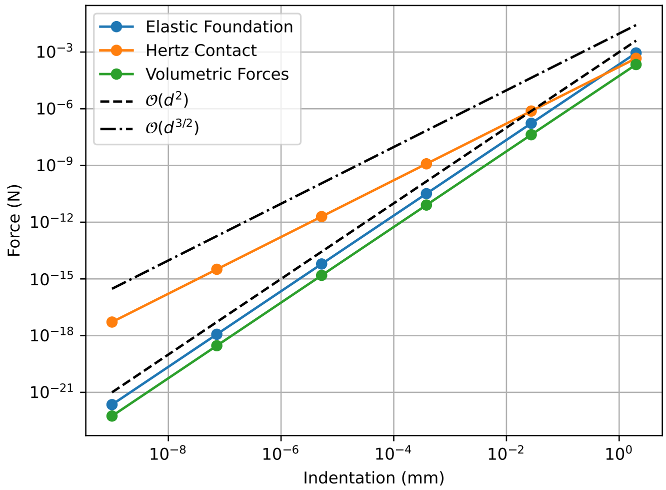

Figure 4.4: Evolution of forces as a function of penetration depth in log-log scale for the three different models.

indentation depth to the power of 1/2, $p \propto d^{1/2}$. Furthermore, it can be observed that for a given indentation depth, the elastic foundation tends to result in a higher maximum pressure.

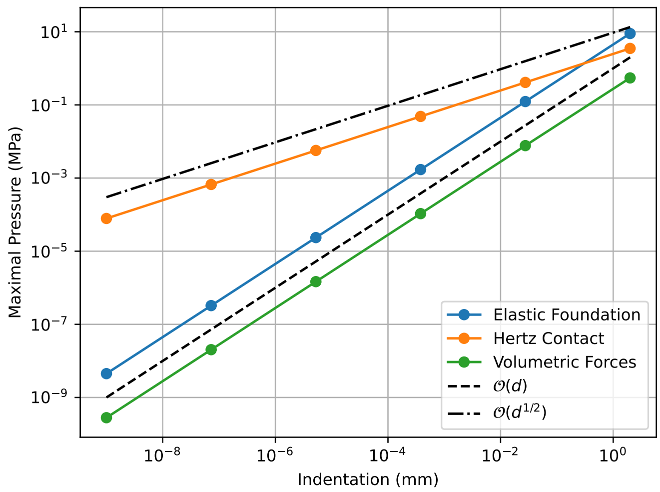

Figure 4.5: Evolution of the maximal pressure as a function of penetration depth for the three different models.

As regards material parameters, Figure 4.6 reveals that Young's modulus has a significant influence on maximum contact pressure. The contact force increases linearly as the Young's modulus increases, which is to be expected since the contact force is proportional E. This is less true for the Poisson coefficient, except when approaching 0.5, where the pressure explodes due to the term $(1 - 2\nu)$ in the denominator of equation 4.3.

These results are obtained in a case where the penetration is fixed, not as when it will be adjusted when the models are in equilibrium. In reality, changing any parameter will change the value of penetration. This will be studied in Chapter 5.

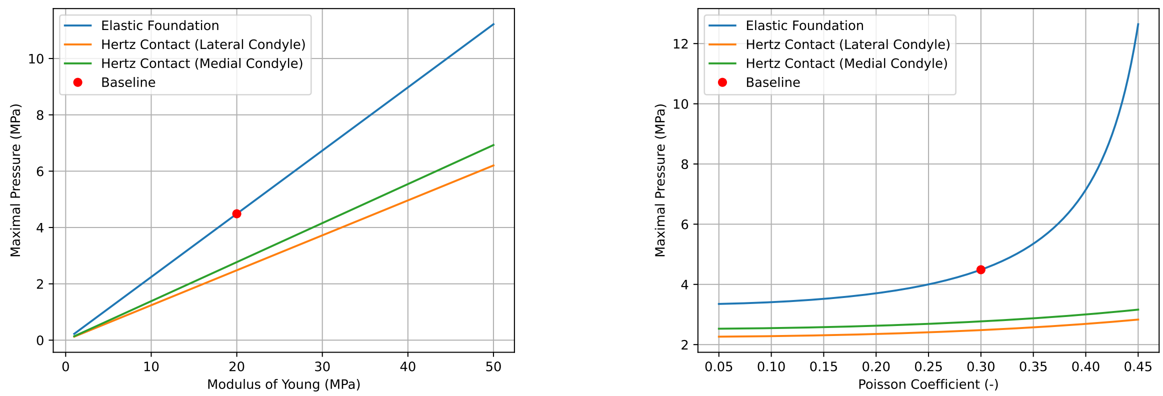

Figure 4.6: Influence of the Young's modulus (on the left) and the Poisson's ratio (on the right) on the maximal pressure of contact for $d = 1$ mm. Baseline corresponds to the case that is used as the reference case.

Subsequently, the pressure distribution must be examined following an investigation of the maximum pressure. As mentioned earlier, the maximum pressure for Hertz is lower than for the elastic foundation model. Equation 4.7 produces a parabolic pressure distribution for Hertz, which is not the case for the elastic foundation. Figure 4.7 illustrates the pressure distribution for both models. Figure 4.8 reveals this from another perspective.

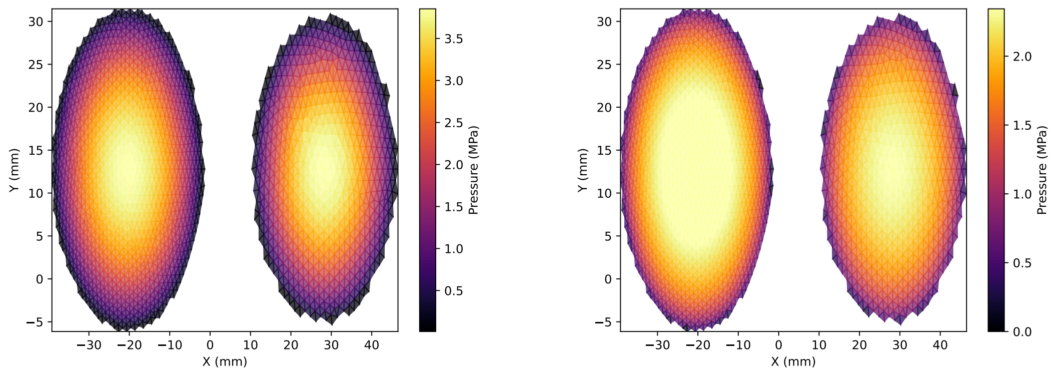

Figure 4.7: Pressure distribution in the contact area for the same penetration distance. The figure on the left illustrates the pressure distribution using the elastic foundation model, and the figure on the right the pressure distribution using the Hertz model.

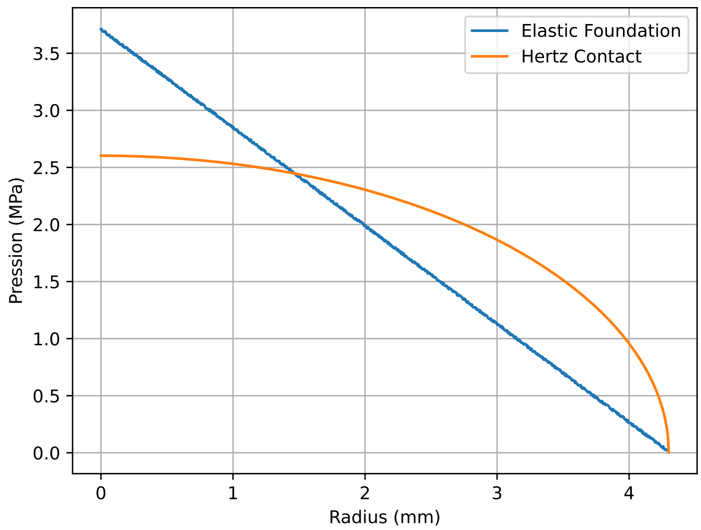

Figure 4.8: Comparison of the pressure distribution between the elastic foundation model and the Hertz model.

Chapter 5

Implemented Models

This chapter examines the different models implemented in this study. The initial model assumes that contact is punctual. The femoral condyles are represented by rigid spheres, while those of the tibia are represented by rigid planes. Next, more complex models are implemented using meshes to represent the condyles more realistically and to get an idea of the flexibility of the knee joint. The influence of varying parameters will be investigated and the results will be validated against existing literature. The effect of ligaments will also be investigated and finally the effect of contact geometry on the results.

5.1 Rigid Model

To start, a simple model has been created, which is mainly an application of Robotran. Using the dimensions of the model in Appendix B.1, a two-body model can be constructed, wherein the first represents the femur and the second represents the tibia.

5.1.1 Model Creation

The femur is fixed in place, and the tibia is attached to the femur with six degrees of freedom. These six degrees comprise the three translations and three rotations of the knee joint, which are explored in greater detail in Section 2.1.2.
The first objective in this case is to examine the influence of the force applied to the condyles, and to understand how it is distributed. The knee joint will be locked in flexion/extension, and a vertical force of $800N$ will be applied to the center of the distal part of the tibia at 0 degrees of flexion, corresponding to the global position $(-7.9, 12.8, -380)$ mm. This point will be the reference application position.
This could represent the force associated with contact between the foot and the ground.
Constraints will be placed on the other joint translations and rotations, with the constraints described in Section 1.3.1.
This means that there are three constraints for each contact between the femoral and tibial condyles, and only one for each ligament (Fig. 5.1). The result is :

- *Condyles* : two ball-type cuts, six constraints, two dependent variables and four degrees of freedom added to create the tibial planes.

- *Ligaments* : three rod cuts, three constraints, three dependent variables.

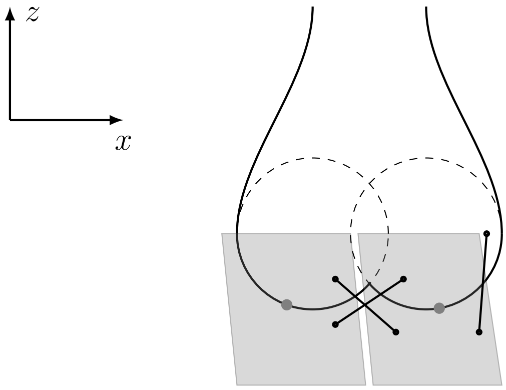

Figure 5.1: Schematic representation of the knee joint model with the tibial and femoral condyles. The black lines represent the ligament constraints, while the tibial planes are shown in grey with a dot representing the three constraints imposed on each of them.

Note that there are only three possible constraints that can be imposed on the ligaments, whereas traditionally there are four main ligaments. We decided to eliminate the LCL ligament, which is not included in Table B.1 used by [14] and which, as a reminder, is not attached to the tibia but to the patella.

This means that every knee joint is under stress, and the following results are obtained without the ligaments (Table 5.1).

Force Medial	41.48 %	323.71 N
Force Lateral	58.51 %	456.67 N

Table 5.1: Force distribution without the impact of the ligaments for the Rigid model with a force of 800N applied to the reference point.

The force is distributed more over the lateral condyle than on the medial condyle. This can be explained by the fact that although the application point is geometrically at the same distance, but the lateral condyle is larger than the medial condyle.
Note that the sum of the forces distributed in the two condyles is not equal to the value of the external force ($800N$). This phenomenon can be attributed to the influence of gravity, with the weight of the femur and tibia included in the model.

Adding the constraints on the ligaments, the results are shown in Table 5.2. This simple method of representing ligaments does not affect the model. The values are very low, which is not the case in reality. This is probably due to the constraints placed on the femoral condyles, which also affect ligament stress. Due to the low value of ligaments, the percentage of ligaments is not a significant representation.

An important parameter that will influence the results is the point at which the force is applied. If this point is moved, the force applied to the condyles will vary. This is mainly due to the torque generated by the movement of this point. Indeed, the resulting force moment around a point is the vector product of the force $F = [F_x, F_y, F_z]$ and the lever arm

Force Medial	41.48 %	323.71 N
Force Lateral	58.51 %	456.67 N
Ligament MCL	55.04 %	3.63e-08 N
Ligament ACL	4.97 %	3.28e-09 N
Ligament PCL	39.98 %	2.64e-08 N

Table 5.2: Force distribution with the impact of the ligaments for the Rigid model with a force of 800N applied to the (-7.9, 12.8, -380) mm point.

$d = [d_x, d_y, d_z]$. The following equation is derived for the moment of force:

$$T = d \times F = \begin{pmatrix} d_y F_z - d_z F_y \\ d_x F_z - d_z F_x \\ d_y F_x - d_x F_y \end{pmatrix}$$

As the force is applied vertically $F = [0, 0, F_z]$, a moment of force will appear, which will influence the force applied on the condyles as well as the flexion/extension of the knee. As this rotation is blocked, it is only by moving d_x that there will be an impact. In fact, this is logical: if the movement is on the longitudinal or antero-posterior axis, there is no torque on the condyles if the force is perfectly vertical, but there is on the transverse axis.

The impact of this movement on the results will now be examined, and the following results will be obtained (see Fig. 5.2).

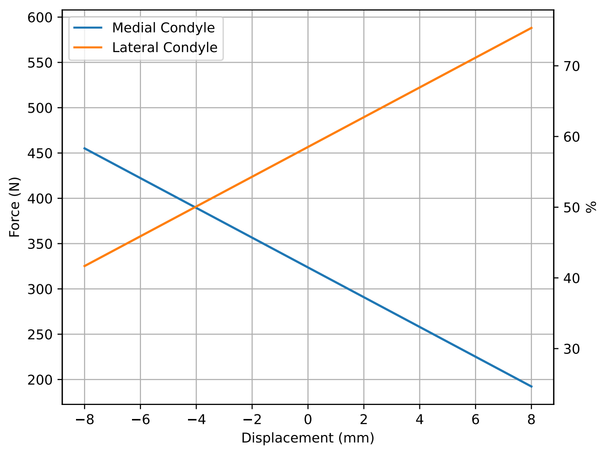

Figure 5.2: Variation of the force for the Rigid model as a function of the position of the application point in the transverse axis, where displacement 0 is the reference application point, positive displacement is to the right and negative displacement is to the left.

The closer to the medial condyle, the greater the force applied, and vice versa for the lateral condyle. A displacement of $4mm$ of the point of application results in an equilibrium of force between the two condyles.

5.1.2 Validation

To be validated by the literature, a similar study would need to have been carried out. This is not the case. To be sure that the force distribution in Figure 5.2 varies as much with this modification of the point of impact, it is necessary to consider a case that can be easily solved by hand. Consider that :

- No ligaments and gravity.
- Two femoral condyles of the same radius r.
- Two condyles symmetrical in relation to the vertical axis Δx.
- Two tibial contact planes at the same height.

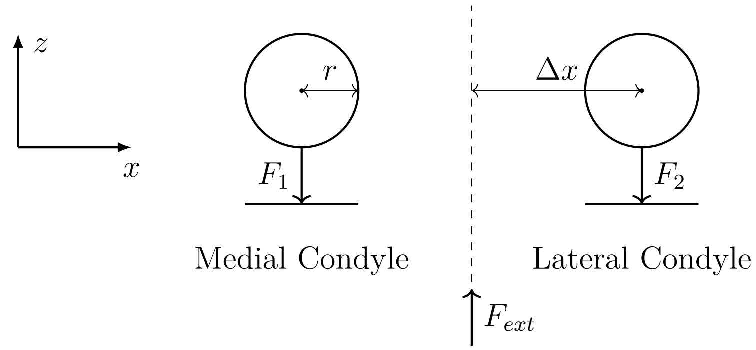

Figure 5.3: Model for the validation of the Rigid model.

Figure 5.3 presents a diagram of the centred model. With equilibrium, the results can be easily verified using classical physics:

$$\begin{cases} \sum F = 0 \\ \sum M = 0 \end{cases} \tag{5.1}$$

Assuming that $\Delta x = 25mm$ and $r = 30mm$, Figure 5.4 reveals the force distribution as a function of the application point of the external force. The same force is applied to both condyles, at the point at equal distance from the condyles on the transverse axis, i.e. the reference application point of the external force. Moreover, assuming a displacement of 3.5 mm, the values of F_1 and F_2 can be verified using equation 5.1, which gives $344N$ and $456N$, respectively.

$$\begin{cases} \sum F = F_1 + F_2 - F_{ext} \overset{\checkmark}{=} 0 \\ \sum M = -F_1 \times (\Delta x + 3.5) - F_2 \times (\Delta x - 3.5) \overset{\checkmark}{=} 0 \end{cases}$$

5.2 Meshes Models

After considering the two bodies as rigid, the condyles are represented by meshes and considered as flexible. Initially the model will be between two spheres in contact with two planes, then the two spheres will be in contact with the mesh of the scanned tibia, and finally the scanned femur will be in contact with the scanned tibia. In these cases, it will be easier to calculate the pressure applied to the condyles, as well as the contact surface and

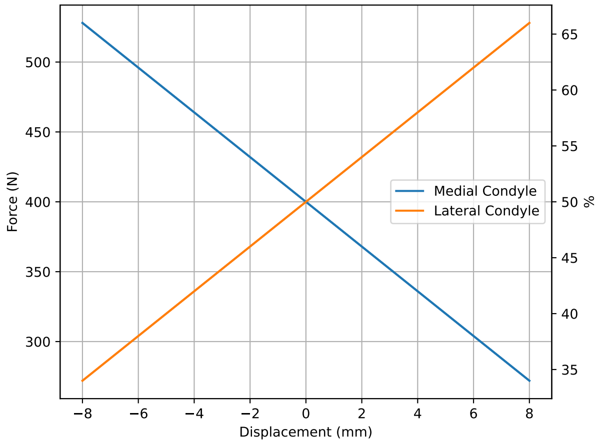

Figure 5.4: Force distribution for the validation of the Rigid model as a function of the position of the application point in the transverse axis, where displacement 0 is the reference point, positive displacement is to the right and negative displacement is to the left.

contact depth. The pressure distribution as a function of the contact surface can thus be determined. All results are, of course, obtained using the equilibrium procedure described in Section 1.3.3.

Figure 5.5 presents a flow diagram which reproduces the order of each stage detailed in the previous chapters.

5.2.1 Sphere/Plane Meshes Contact

The initial model is constructed with the condyles represented by meshed spheres and the tibia by meshed planes. The difference from the previous model is that the condyles are no longer considered as "ball" constraints. Instead, finite elements are used to represent them and forces are applied as a function of the contact area, as explained in Chapter 4. Using the elastic foundation, the following results can be obtained from Table 5.3 when the external force is applied at the same point as before. Obviously, the contact area is calculated using the contact detection algorithm explained in Chapter 3.

	Medial	Lateral
Maximal Pressure (MPa)	3.59	3.81
Mean Pressure (MPa)	1.91	2.08
Total Force (N)	324.1	456.2
Contact Area (mm^2)	168.9	219.2
Depth Max of Contact (mm)	0.8	0.85

Rigid Model	
Medial	Lateral
323.7 N	456.67 N

Table 5.3: Baseline results for Sphere/Plane contact with two sphere meshes of $\simeq 5000$ elements using $E = 20, \nu = 0.3$, the elastic foundation method and without the impact of ligaments. On the right a reminder of the distribution of forces obtained for the first model studied in this chapter (see Table 5.1).

The distribution of forces is identical to that observed in the Rigid model. This observation is valuable because it demonstrates the consistency of our mesh-based approach. The relative error between the two models is less than $1N$.

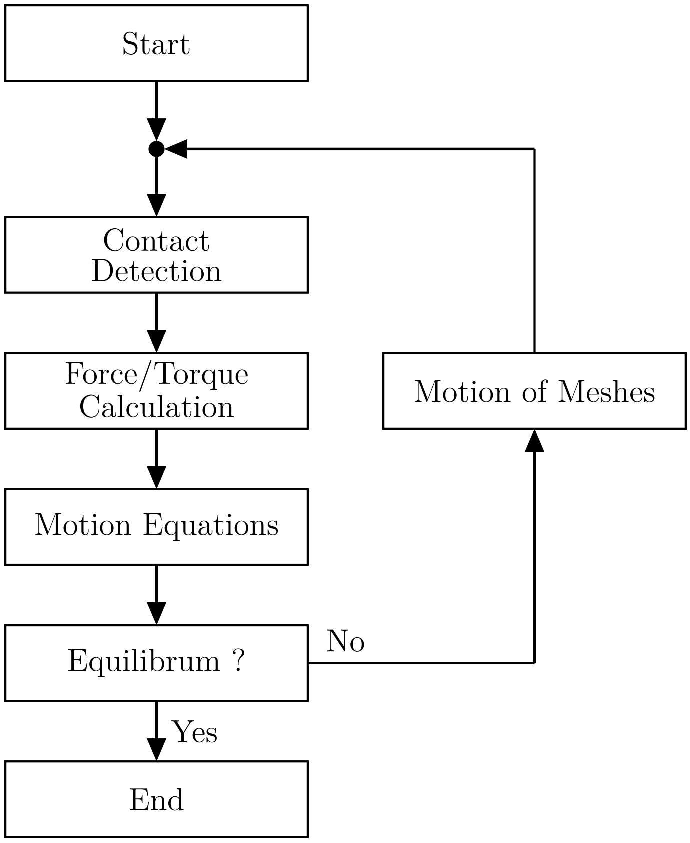

Figure 5.5: Flow diagram of the total algorithm. First, the contacts between the meshes are computed (see Chapter 3). Then, depending on the results obtained, the forces and torques of each body can be calculated (see Chapter 4), and applied to the equations of motion (see Chapter 1). At each Newton-Raphson iteration, the question is determined whether or not equilibrium has been achieved. If not, the meshes are moved according to the position and rotation found for the bodies. If yes, the solution has been found.

Let's now look at the influence and importance of the right choice of parameters. First, the number of elements is increased and the Young's modulus E is varied, the results of which are presented in Table 5.4.

E	9		15		30		Baseline (20)	
Number of elements	4928	13728	4928	13728	4928	13728	4928	13728
Maximal Pressure (MPa)	2.51	2.66	3.18	3.4	4.37	4.70	3.59	3.88
Mean Pressure (MPa)	1.31	1.44	1.73	1.79	2.22	2.55	1.91	2.09
Total Force (N)	326.3	328.6	326.4	328.5	326.2	328.0	324.1	328.5
Contact Area (mm^2)	249.8	236.1	186.9	184.3	145.4	132.8	168.9	161.8
Maximum Depth (mm)	1.24	1.32	0.95	1.01	0.65	0.69	0.8	0.86

(a) Medial Part

E	9		15		30		Baseline (20)	
Number of elements	4936	13702	4936	13702	4936	13702	4936	13702
Maximal Pressure (MPa)	2.62	2.77	3.32	3.52	4.54	4.88	3.81	4.04
Mean Pressure (MPa)	1.42	1.43	1.75	1.86	2.42	2.5	2.08	2.15
Total Force (N)	454.1	451.8	453.9	451.9	454.1	452.3	456.2	451.9
Contact Area (mm^2)	325.6	323.4	262.3	245.9	187.5	182.1	219.2	214.5
Maximum Depth (mm)	1.29	1.37	0.99	1.05	0.68	0.72	0.85	0.9

(b) Lateral Part

Table 5.4: Variation of the Young's modulus E for the medial and lateral condyles with $\nu = 0.3$ and $\simeq 5000$ and 13000 elements with the reference point of impact and without ligaments.

For the variation in the number of elements, the main difference lies in the contact area, which decreases because the contact detection algorithm tends to overestimate the detection area less when the number of elements increases. This effect modifies the pressure but has a negligible impact on the distribution of forces.

It can be observed that the increase in Young's modulus E has a greater influence on the results, particularly the pressure value. This can be explained by the fact that Young's modulus increases the rigidity of the material. Nevertheless, the force between the two femoral condyles remains more or less the same. This means that the variation in Young's modulus E has no influence on the force applied between the two condyles.

This is explained because of the equilibrium, note that unlike the discussion in Section 4.2 where the material parameters are examined as a function of different types of force, equilibration here modifies the maximum penetration of the contact. Consequently, the maximum pressure does not vary in the same way as in Figure 4.6.

The other parameter to be varied is the Poisson's coefficient ν. The results are presented in Table 5.5. As with Young's modulus E, an increase in the Poisson's coefficient ν increases the pressure on the condyles and does not change the force between the two condyles.

As with the previous model, let's now examine the influence of the point of impact on the results, as shown in Figure 5.6. Despite the presence of a few errors, the result is the same as in Figure 5.2. In fact, the point where an equal distribution is found between the two condyles is slightly offset and the error relative to the previous model is less than 1% when the impact point is moved by $8mm$. This serves to validate the initial mesh model.

Poisson Coefficient ν	0.15	0.4	0.45	Baseline (0.3)
Maximal Pressure (MPa)	3.24 3.39	4.49 4.67	5.77 6.09	3.59 3.81
Mean Pressure (MPa)	1.83 1.81	2.33 2.49	3.34 3.17	1.91 2.08
Total Force (N)	324.1 456.3	324.3 456.1	324.8 455.7	324.1 456.2
Contact Area (mm^2)	176.8 254	138.1 183.9	95.1 140	168.9 219.2
Depth Max of Contact (mm)	0.92 0.96	0.62 0.65	0.45 0.48	0.8 0.85

Table 5.5: Variation of poisson coefficient ν for $E = 20$, 4928 elements for the medial and 4936 for the lateral, the value for the medial condyle is above while for the lateral it is below.

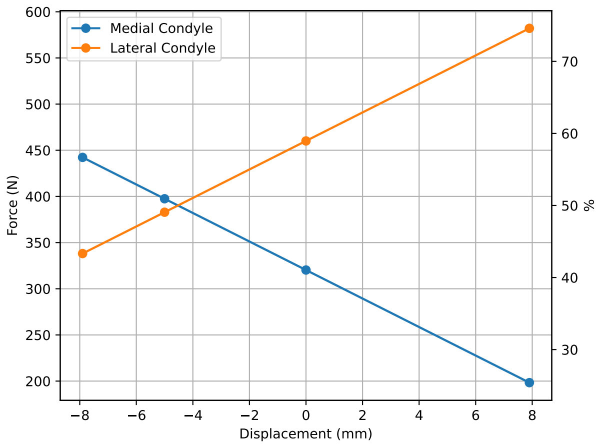

Figure 5.6: Variation of the force passing through the two femoral condyles for the Sphere/Plane meshes contact model as a function of the position of the application point in the transverse axis, where displacement 0 is the reference point, positive displacement is to the right and negative displacement is to the left.

All this was done without the impact of the ligaments, which is why a contribution from the ligaments will be added. This time the ligaments have been included, which gives the results in Figure 5.7.

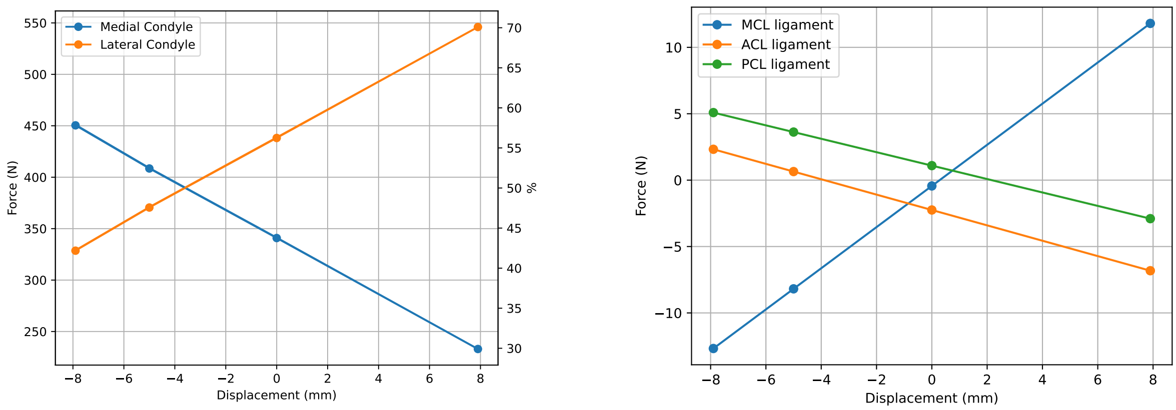

Figure 5.7: On the left, the variation of forces in the condyles, on the right the variation of forces in the ligaments. These variations are for the Sphere/Plane meshes model.

Ligaments influence the results. Note that a positive force on the ligaments indicates traction, whereas a negative force indicates compression. The results are always of the same order of magnitude: for example, the point at which the distribution of forces between two condyles is identical is shifted by just under $1mm$ compared to the model without ligaments, while the % distribution remains more or less the same.

With regard to the ligaments, the MCL ligament, which connects the medial condyle of the femur to the upper part of the tibia and is responsible for maintaining stability of the knee, is in compression when the force on the medial condyle is greater. The other two ligaments are also connected and follow a similar trajectory. These are the two cruciate ligaments, whose principal function is to restrict the rotation of the knee.

Hertz

Chapter 4 showed that the Hertz equation can be used to calculate the pressure on the condyles. Using the reference parameters, the following results are obtained, see Table 5.6.

	Hertz Method		Elastic Foundation Method	
	Medial	Lateral	Medial	Lateral
Maximal Pressure (MPa)	2.49	2.43	3.59	3.81
Mean Pressure (MPa)	1.34	1.33	1.91	2.08
Total Force (N)	337.8	442.5	324.1	456.2
Contact Area (mm^2)	262.2	325.5	168.9	219.2
Depth Max of Contact (mm)	1.33	1.36	0.8	0.85

Table 5.6: Baseline results for Sphere/Plane contact with two $\simeq 5000$ elements sphere meshes using $E = 20, \nu = 0.3$, the Hertz method, and without the impact of ligaments. On the right, a reminder of the results using the elastic foundation (Table 5.3).

Using the Hertz model, the applied force is close to that obtained with the elastic foundation. The only parameter that changes is the pressure, which is lower with the Hertz method. This influences the contact area, which is larger with the Hertz method. This difference was discussed in Section 4.2, and is confirmed by these results.

The results are summarised in Figure 5.8, where the point of impact of the force is varied. The results are more or less the same as for the elastic foundation. In fact, when the ligaments are not used, the points with the same distribution on either side of the condyles are situated in approximately the same location, with the only difference being the displacement of the point of impact, which is smaller.

One hypothesis to explain this phenomenon is that the contact zone is smaller on the Hertz side (remind Fig. 4.3). In the case of an elastic foundation, the surface area is significantly larger, giving more importance to the condyle, where the distribution of forces is greatest. To illustrate, when the external force is offset by $-8mm$ on the transverse axis, the medial condyles are approximately 450 and 430N for the elastic foundation and Hertz respectively, whereas if the external force is offset by $8mm$, the medial condyles are 210 to 250N, again with the elastic base and Hertz respectively. In both cases, Hertz therefore underestimates the force. However, given the limited data available, Hertz is a very good approximation when the femoral condyles are assumed to be perfect spheres in contact with planes.

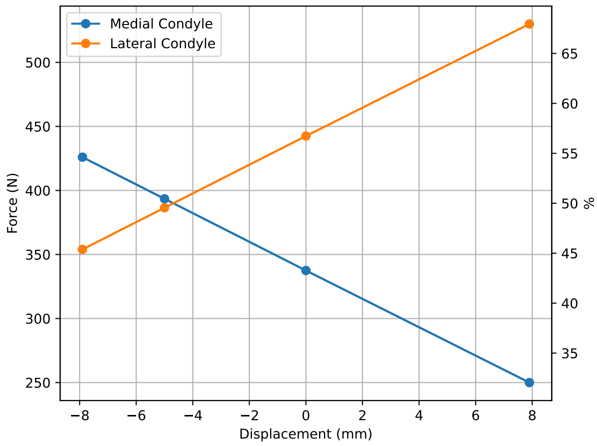

Figure 5.8: Variation of forces in the condyles using the Hertz method as a function of the position of the application point in the transverse axis, where displacement 0 is the reference point, positive displacement is to the right and negative displacement is to the left.

The next step is to add the ligaments to determine their contribution (Fig. 5.9). On this occasion, the results cannot really be said to be exactly the same as those obtained using the elastic foundation method (Fig. 5.7). Indeed, as explained above, when using the Hertz method, the surface area and pressure are lower, resulting in a greater depth of penetration to obtain the same order of magnitude of force. This depth of penetration gives greater importance to the ligaments. This modification affects the distribution of force within the condyles.

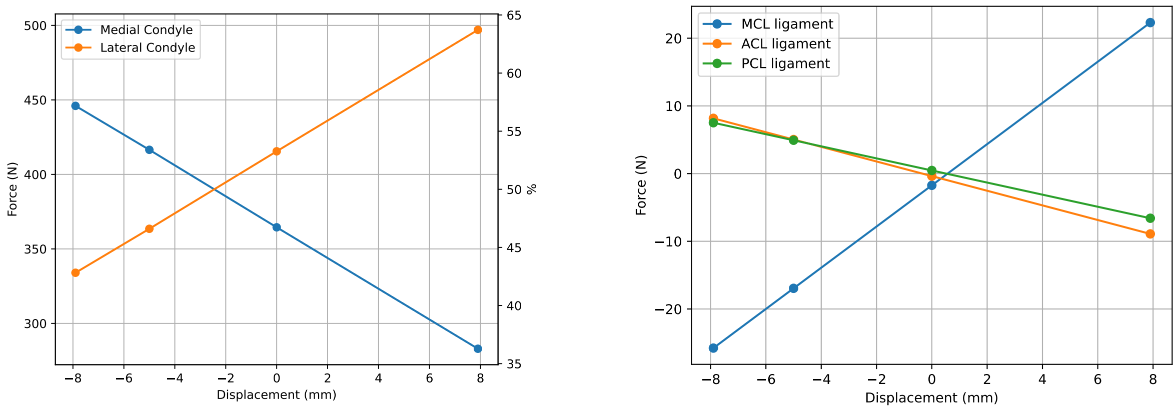

Figure 5.9: On the left, the variation in forces in the condyles, on the right, the variation in forces in the ligaments. These variations are using the Hertz method for the Sphere/Plane meshes model.

Maximum Pressure and Torque

The great advantage of using finite elements is that it is easy to concentrate on the pressure exerted on the condyle. This can be observed in Figure 4.7, which analyses the pressure difference between the elastic foundation model and the Hertz model, in the previous chapter. It also provides an opportunity to analyse the maximum pressure difference when the point of impact is moved.

Figure 5.10 reveals this difference without the use of ligaments, as well as the resulting torque caused by the force applied to the condyles. As the pressure on one condyle increases, the pressure on the other decreases. The maximum pressure on the medial condyle decreases with increasing displacement, while the maximum pressure on the lateral condyle increases. This is in similar to the distribution in force analysis.
However, the point at which the distribution of forces is the equivalent does not correspond to the point at which the maximum pressures are identical. As far as the torques are concerned, the torques of the two condyles cancel each other out at the reference point of impact. Note that a positive torque indicates rotation in the abduction direction and a negative torque in the adduction direction. These rotations have been discussed in Chapter 2 (see Figure 2.3).

Figure 5.11 presents the same situation but with the ligaments included. The same conclusions can be reached, however, it can be observed that the maximum pressure is the same at the reference point of impact. The constraints of the ligaments result in an identical maximum pressure at the reference impact point, which in reality is a desired result. This is partly explained by the fact that the ligaments play a crucial role in stabilising the knee joint by distributing loads evenly and preventing excessive movements that could result in damage to internal structures.

Literature Validation

The validation of the results with the literature is very complicated due to the different parameters that have an influence on the model. The difficulty may be attributed to various

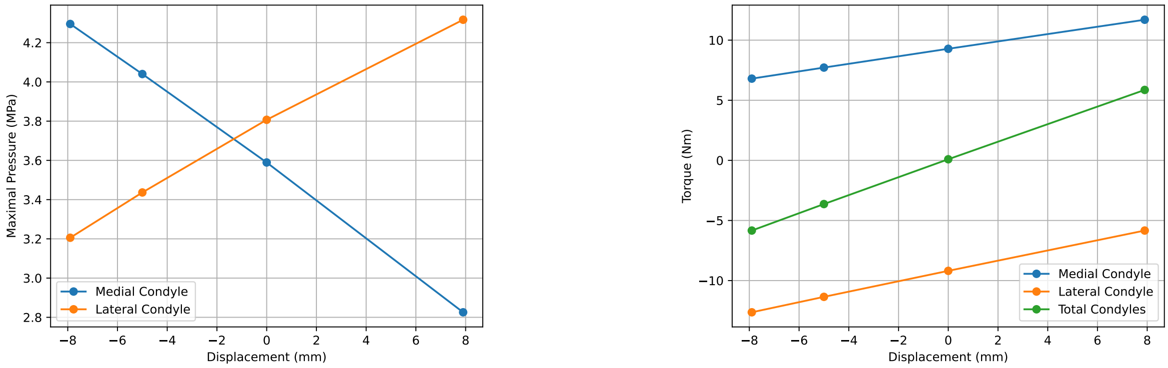

Figure 5.10: On the left, the maximum pressure for the Sphere/Plane meshes contact model without ligaments, on the right the torque as a function of displacement of the application point in the transverse axis.

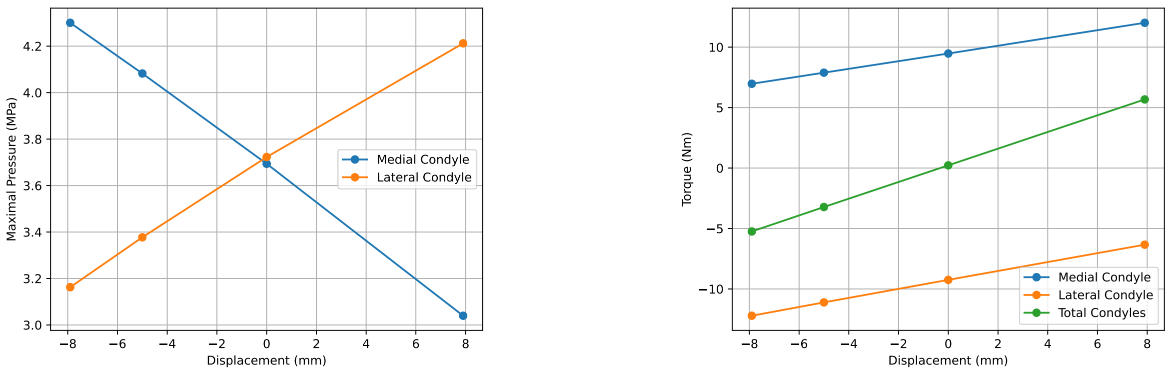

Figure 5.11: On the left, the maximum pressure for the Sphere/Plane meshes contact model with ligaments, on the right the torque as a function of displacement of the application point in the transverse axis.

factors, including the lack of consideration for ligament flexibility, the choice of coefficients, the location of force application, and the distinct geometrical characteristics of the model and the literature. However, if the orders of magnitude are found to be the same, that is already a good point.

[46] developed a geometrically accurate three-dimensional solid model of the human knee, focusing on the menisci and articular cartilage. The bone models (tibia and femur) were produced from computed tomography (CT) images, giving the exact geometry of the bones. Similarly, he applied a force of $800N$ at 0 degree of flexion. Tables 5.7a and 5.8a summarise his results.

Average element size	Max Pressure	Mean Pressure	Total Force	Contact Area
5 mm by 5 mm	3.05 MPa	1.02 MPa	410 N	365 mm^2
2 mm by 2 mm	2.38 MPa	0.88 MPa	404 N	409 mm^2
1 mm by 1 mm	2.36 MPa	0.88 MPa	408 N	415 mm^2

(a) Resuts obtained from [46] of the lateral condyle.

Average element size	Max Pressure	Mean Pressure	Total Force	Contact Area
5 mm by 5 mm	2.62 MPa	1.32 MPa	392N	385 mm^2
2 mm by 2 mm	2.77 MPa	1.41 MPa	395 N	376 mm^2
1 mm by 1 mm	2.79 MPa	1.43 MPa	393 N	374 mm^2

(b) Our results from the lateral condyle for the elastic foundation model.

Table 5.7: Comparison for the lateral condyle of maximum pressure, mean pressure, total force and contact area obtained for different mesh sizes with those of [46] for the same position of external force application.

Applying the force at the same point as him, i.e. the point where the force distribution between the condyles is equivalent, gives the following results (Tables 5.7b and 5.8b). Table 5.7 compares the results obtained in this study with those reported by [46] for the lateral condyle. Table 5.8 presents a similar comparison for the medial condyle.

Average element size	Max Pressure	Mean Pressure	Total Force	Contact Area
5 mm by 5 mm	2.75 MPa	1.16 MPa	415 N	401 mm^2
2 mm by 2 mm	2.51 MPa	0.8 MPa	411 N	483 mm^2
1 mm by 1 mm	2.55 MPa	0.78 MPa	409 N	490 mm^2

(a) Resuts obtained from [46] of the medial condyle.

Average element size	Max Pressure	Mean Pressure	Total Force	Contact Area
5 mm by 5 mm	2.51 MPa	1.31 MPa	390 N	401 mm^2
2 mm by 2 mm	2.66 MPa	1.39 MPa	387 N	483 mm^2
1 mm by 1 mm	2.69 MPa	1.41 MPa	389 N	490 mm^2

(b) Our results from the medial condyle for the elastic foundation model.

Table 5.8: Comparisons for the medial condyle of the results obtained for different mesh sizes with those of [46] for the same position of external force application.

The order of magnitude is essentially the same, the only difference being that when the mesh is refined, the contact area increases, which is not the case in our results. Indeed, as already explained a few times, with the detection algorithm presented in Chapter 3, Figure 3.20

suggests that the contact area tends to be overestimated. As a result, the pressure increases when the mesh is refined in the opposite direction.

This author confirms that the finite element model of the human knee is a powerful tool for studying how variables associated with meniscal replacement affect the tibio-femoral contact, which can be crucial for the design of synthetic replacements or for graft selection. In this case, it meets both the objective and the opinion.

Other Application

One method of stressing only the ligaments is to ensure that the force distribution between the femoral condyles is identical. Here, a new constraint is imposed with the objective of ensuring that the force is distributed equally between the two condyles, and an analysis of the impact of the force application point on the results is made.

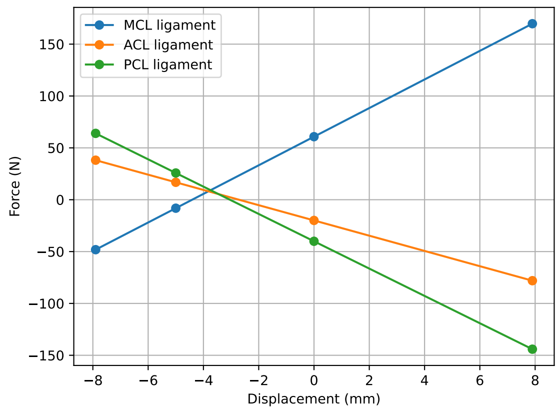

Figure 5.12: Variation of the forces on the ligaments, assuming that the forces between the condyles are equal.

Figure 5.12 illustrates that there is a position where no force is applied to the ligaments. Indeed, at this point, the force is distributed equally between the two condyles (see Fig. 5.7). Similarly, the medial collateral ligament (MCL) is in compression when the medial condyle bears a greater load, whereas the MCL is in traction when there is an increased load on the lateral condyle. Conversely, the anterior cruciate ligament (ACL) and posterior cruciate ligament (PCL) are in tension when the medial condyle is most stressed and in compression when the lateral condyle is most stressed.

Unlike the other cases where the two cruciate ligaments appeared to be connected, here it appears that the PCL is there to counteract the MCL rather than the two cruciate ligaments together.

Inclined Plane

Since the beginning of this chapter, the planes have been assumed to be transverse, but in fact they are inclined. To return to the discussion in Chapter 2, the influence of the inclination of these planes on these results is examined in Table 5.9.

	Inclined Plane		Transverse Plane	
	Medial	Lateral	Medial	Lateral
Maximal Pressure (MPa)	3.18	4.23	3.59	3.81
Mean Pressure (MPa)	1.79	2.22	1.91	2.08
Total Force (N)	352.6	427.4	324.1	456.2
Contact Area (mm^2)	195.8	198.2	168.9	219.2
Depth Max of Contact (mm)	0.71	0.94	0.8	0.85

Table 5.9: Baseline results for Sphere/Plane contact with two sphere meshes of $\simeq 5000$ elements using $E = 20, \nu = 0.3$, using the inclined planes calculated in Table 2.1. On the right, a reminder of the results in Table 5.3 when the planes are considered transverse, i.e. without inclination.

The order of magnitude remains more or less the same. The contact area is smaller, and the distribution of forces is different. Without going into too much detail, since for the rest of the work the scanned meshes of the tibia and femur will be used, Table 5.10 gives the results used when representing the plane with degree 3 polynomials for the tibial plateau.

	Medial	Lateral
Maximal Pressure (MPa)	3.26	4.21
Mean Pressure (MPa)	1.78	2.28
Total Force (N)	332.6	447.8
Contact Area (mm^2)	190.6	204.7
Depth Max of Contact (mm)	0.81	1.03

Table 5.10: Baseline results for Sphere/Plane contact with two sphere meshes of $\simeq 5000$ elements using $E = 20, \nu = 0.3$, using degree 3 polynomials for the tibial plateau.

The difference between the two tables is mainly in the force, but the maximum and average pressures remain similar. It is hoped that the results using the polynomials will be similar when using the scanned meshes.

5.2.2 Sphere/Tibia Meshes Contact

Now that the analysis of the case where the tibial condyles are represented by planes has been completed, it is appropriate to move on to the case where the mesh of the scanned tibia is used to represent them.

Given the geometry, there is a conflict with the intercondylar eminence [1]. Figure 5.13 represents the contact, it is exaggerated to better view the part of the collision. This is because the spheres representing the femoral condyles are overestimated and thus a collision with this bony structure occurs, which is not possible in reality. This distorts the results by adding forces that should not exist. In addition, the result are an unequilibrium in the system.

To remedy this, the part of the spheres that is in contact with this structure is cut out and the spheres are represented as hemispheres of different sizes. The idea is to try to keep

[1] As a reminder, the intercondylar eminence is a bony structure located on the upper part of the tibia, between the medial and lateral condyles.

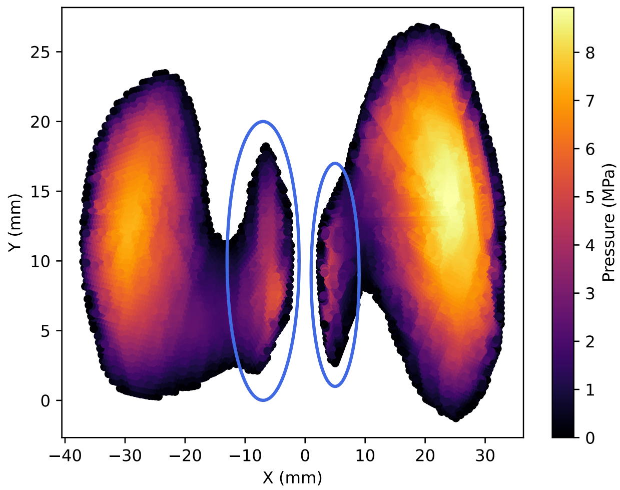

Figure 5.13: Example of a case where the spheres collide with the intercondylar eminence of the tibia. This area is outlined in blue.

the shape of the femoral condyles simple. Later on, the case will be analysed with the real geometry of the femoral condyles.

As a reminder, in Chapter 3, there are two methods of contact detection, and these two algorithms depend on the nature of the meshes used. In this case, both methods can be used. Indeed, since in this case the scanned tibia mesh (concave mesh) is used with spheres (convex or concave meshes), the configuration can be either Concave-Concave or Convex-Concave. Figure 5.14 confirms that the two algorithms used in this work give the same results, apart from a few negligible errors. Consequently, Algorithm 1 will be used for the remainder of the analysis, as it is much faster and gives the same results.

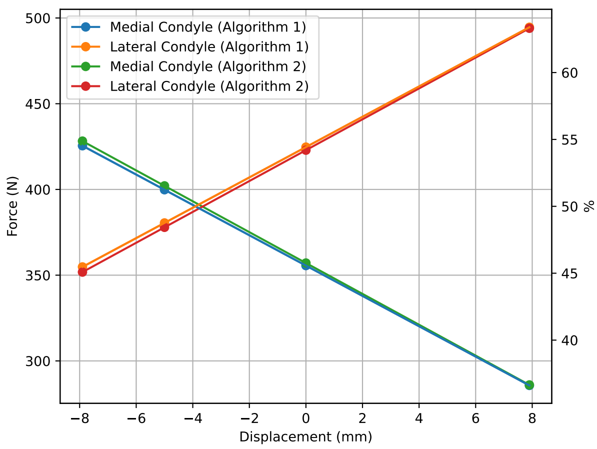

Figure 5.14: Variation of the force for the Sphere/Tibia meshes contact model as a function of the position of the application point in the transverse axis, where Algorithm 1 is the Collision algorithm in Section 3.2 and Algorithm 2 is the Ray Casting algorithm included in Section 3.4.

The point of equal force distribution between the two condyles is the same as for the other models, however, the effect of the force application point is less important than for the others.

The distribution of force remains fairly even, unlike the punctual model where 3/4 of the force passes through the lateral condyle when the application point is moved by $8mm$. Note that at the initial point of application, the distribution is very similar to Table 5.9, which represents the model from earlier when the planes were inclined.

With regard to the addition of ligaments, the results are shown in Figure 5.15.

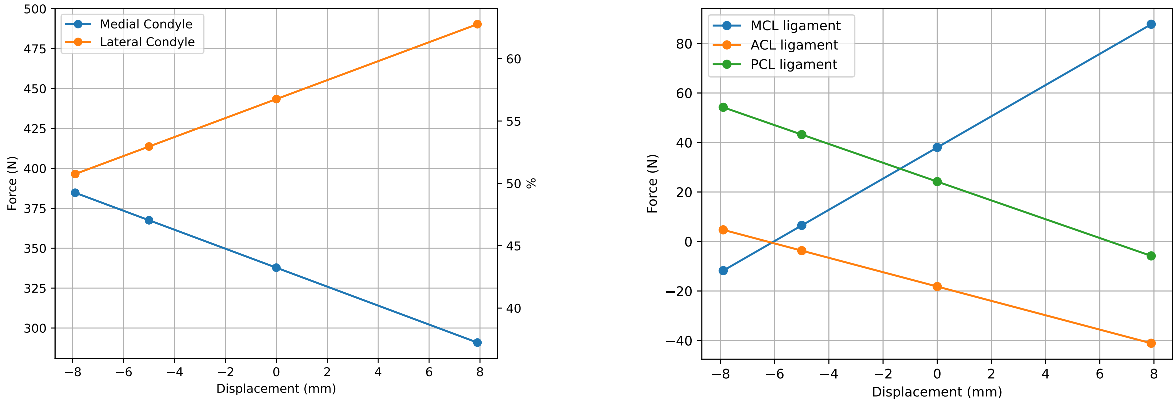

Figure 5.15: On the left, the variation of forces in the condyles, on the right, the variation of forces in the ligaments as a function of the application point of the external force. These variations are for the Sphere/Tibia meshes model.

In this case, the influence of the ligaments is more pronounced than in the other models, which may be attributed to an implementation error. The ligaments are very sensitive to geometry. If the attachment point is incorrectly positioned, the results can be distorted. Nevertheless, an equilibrium solution was found.

Although the application point of the external force must be moved a considerable distance in order for the medial condyle to be the most represented, the distribution remains well distributed and not everything passes through a single condyle, which is a good point. Furthermore, although the ligament values are higher than in the other cases, their norms remain correct. The MCL ligament increases as a function of the force distribution in the lateral condyle and the other two ligaments react together in the opposite way.

5.2.3 Femur/Tibia Meshes Contact

In the last case, the scanned femur and tibia meshes are employed to represent the condyles. In this way, the available geometry is used to represent the condyles and the results are hopefully as close to reality as possible. Unlike the other models, the Ray Casting algorithm must be used to detect the contact, as the Collision algorithm does not work for this type of mesh. The calculation time is therefore much longer. For the reference point application of the external force, the results are presented in Table 5.11.

Compare with Table 5.9 for the Sphere/Planes model, by inclining the planes. The pressures are almost the same. However, the distribution of forces and the contact area are different, although the values are related when polynomials are used (Table 5.10). The point model is even closer when the contact is considered with only kinematic constraints, i.e. the Rigid model (see Section 5.1).

	Femur/Tibia		Inclined		Polynomial	
	Medial	Lateral	Medial	Lateral	Medial	Lateral
Maximal Pressure (MPa)	3.4	4.2	3.18	4.23	3.26	4.21
Mean Pressure (MPa)	1.76	2.12	1.79	2.22	1.78	2.28
Total Force (N)	294.1	486.3	352.6	427.4	332.6	447.8
Contact Area (mm^2)	188.2	219.8	195.8	198.2	190.6	204.7
Depth Max of Contact (mm)	0.88	1.11	0.71	0.94	0.81	1.03

Table 5.11: Baseline results for the Femur/Tibia meshes contact model using the Ray Casting algorithm with $\simeq 5000$ elements, $E = 20, \nu = 0.3$ and without the impact of ligaments. The "Inclined" tabular is a reminder of Table 5.9 and the "Polynomial" tabular is one of Table 5.10, these are the results obtained by the Sphere/Plane contact using for the plane, an inclined plane and a degree 3 polynomial respectively.

Figure 5.16a shows the impact of the force application point on the results. The position of the force application point between the two condyles is offset by $2mm$ compared with the first model. However, the impact appears to be the same: in addition to the initial error, the model reacts in the same way to the modification. The relative error remains constant at $\pm 2\%$.

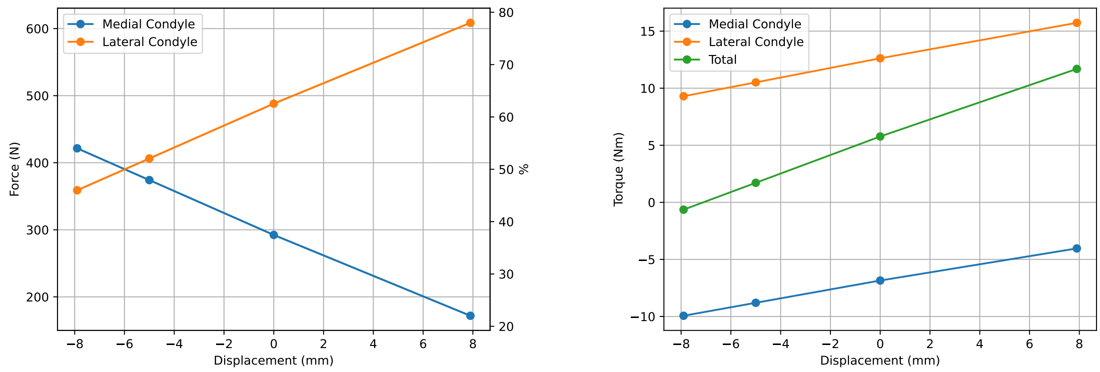

(a) (b)

Figure 5.16: Variation of the force (a) and the torque (b) for the Femur/Tibia meshes model as a function of the position of the application point in the transverse axis.

This difference can also be noticed in the distribution of torques, as the more realistic geometry does not apply a total torque of zero at the reference point of impact (Fig. 5.16b). The sum of the torques between the condyles is zero when the point of impact is moved to the left. This could explain the $2mm$ offset in the equivalent distribution of forces in the condyles observed above.

Figure 5.17 illustrates the position of the meshes obtained. It can be seen that the mesh is not in contact with the intercondylar eminence.

Figure 5.18 highlights the pressure exerted on the condyles. The closer the force application point is to the medial condyle, the greater the force and the greater the pressure on that condyle. The shape of the condyle is visible, with maximum pressure in the centre.

The ligaments are now added to examine their contribution, as shown in Figure 5.19. As in

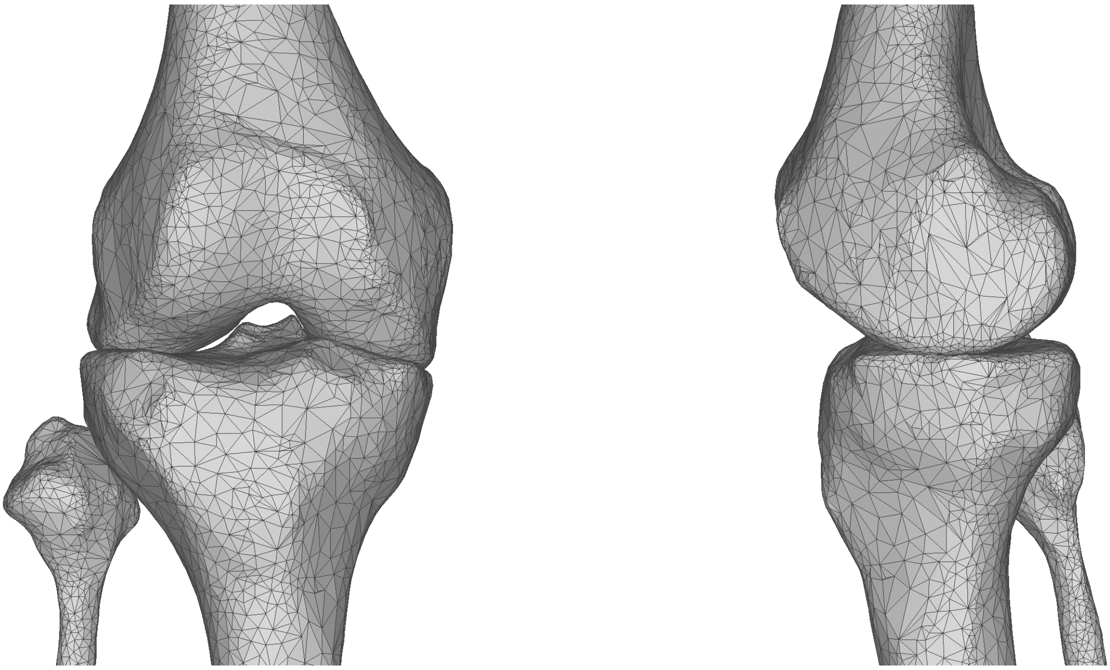

(a) (b)

Figure 5.17: Visualisation of the position of the meshes obtained when applying the external force to the reference point without ligament in several views: (a) frontal view and (b) sagittal view.

the previous model, the impact of the added ligaments is significant. The ligaments seem to behave in more or less the same way as in the previous model, but they are much more stressed. This is reflected in the distribution of forces, which remains reasonable, but where there is equal distribution between the two condyles at a displacement $\Delta x = -16.9mm$. A ligament that can resist a pull of 200N seems realistic, since they can resist several thousand newtons.

Figure 5.21 reflects the pressure exerted on the condyles by the impact of the ligaments. It can be seen that the ligaments shift the contact surface as well as the shape, resulting in a larger surface area. The maximum pressure is still centred, but for the lateral condyle (on the right) it is no longer of the same strength, touching the intercondylar eminence slightly.

This can be felt in the torque distribution (Fig. 5.20), where the torque of the femoral condyle varies only slightly and does not match that found in Figure 5.16b. The collision with the intercondylar joint alters the results, distancing the analysis from reality. The geometry and the representation of the ligaments are no longer precise enough to be used in this model.

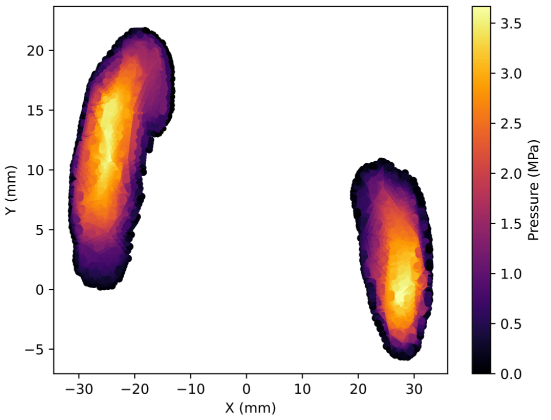

(a) $\Delta x = -7.9$ mm

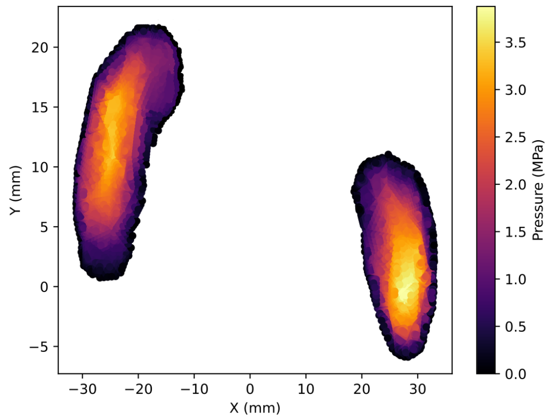

(b) $\Delta x = -5$ mm

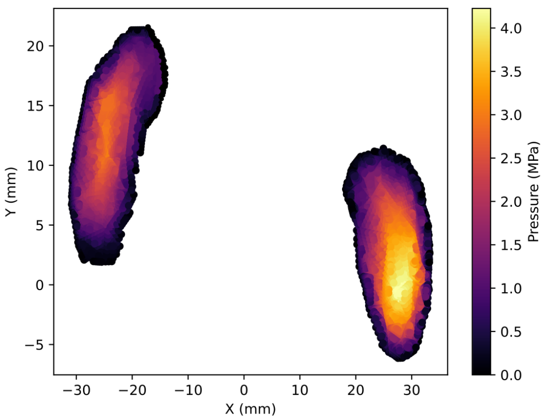

(c) $\Delta x = 0$ mm

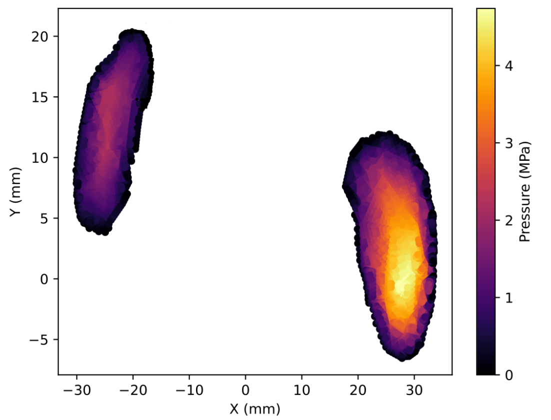

(d) $\Delta x = 7.9$ mm

Figure 5.18: Representation of the pressure applied on the condyles for the Femur/Tibia meshes model without ligaments, depending on the application point of the external force.

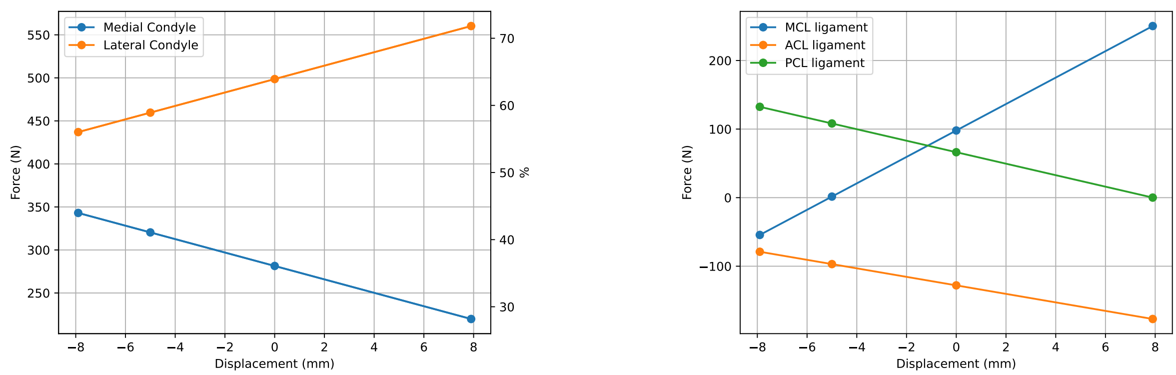

Figure 5.19: On the left, the variation of forces in the condyles, on the right, the variation of forces in the ligaments. These variations are for the Femur/Tibia meshes model with ligaments.

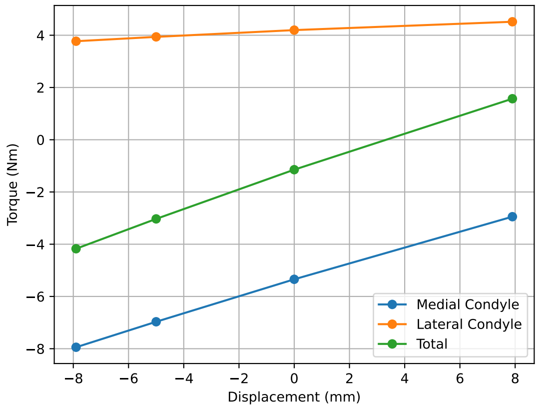

Figure 5.20: Variation of the torque for the Femur/Tibia meshes model with ligaments impact as a function of the position of the application point in the transverse axis.

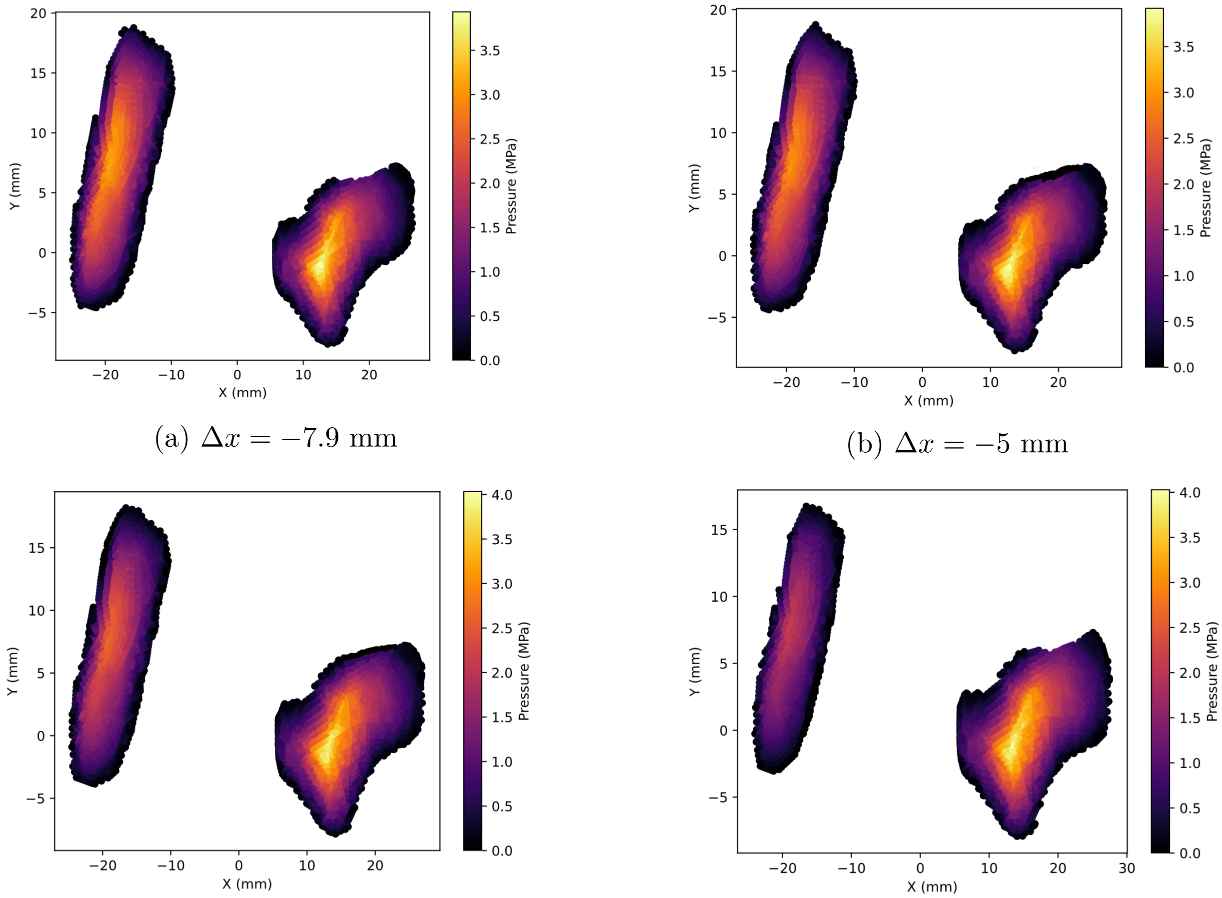

(a) $\Delta x = -7.9$ mm

(b) $\Delta x = -5$ mm

(c) $\Delta x = 0$ mm

(d) $\Delta x = 7.9$ mm

Figure 5.21: Representation of the pressure applied on the condyles for the Femur/Tibia meshes model with ligaments, depending on the application point of the external force.

5.3 Discussion

Each case presented here shows the same trends when ligaments are not considered. Each model has its own set of advantages and disadvantages. The initial model was a Rigid model, which was a purely multibody dynamics application using rigid bodies. This model provided us with a comprehensive understanding of the distribution of forces between the condyles, which were considered as simple shapes.

The following models were constructed using meshes, which represented a crucial step in understanding the concept of pressure, a fundamental aspect in the medical domain. This approach also allowed us to increase the complexity of the articular surface geometry, after obtaining similar results to the first model. The results of the various meshes models are presented in Table 5.12. These models demonstrated that the simplicity of ligament modeling is insufficient when the complexity of the geometry increases. The ligaments are implemented with insufficient realism, as they assume that two points remain at the same distance, which is unrealistic given that ligaments are flexible. It has been observed that a small error in dimension, simplification gives results that do not represent reality. However, the differences between the models remain small, as shown by the different variations in the distribution of forces between the condyles.

		Baseline	Hertz	Inclined	Polynomial	Scanned
Max Pressure (MPa)	Medial	3.59	2.49	3.18	3.26	3.4
	Lateral	3.81	2.43	4.23	4.21	4.2
Mean Pressure (MPa)	Medial	1.91	1.34	1.79	1.78	1.76
	Lateral	2.08	1.33	2.22	2.28	2.12
Total Force (N)	Medial	324.1	337.8	352.6	332.6	294.1
	Lateral	456.2	442.5	427.4	447.8	486.3
Contact Area (mm^2)	Medial	168.9	262.2	195.8	190.6	188.2
	Lateral	219.2	325.5	198.2	204.7	219.8
Depth Max (mm)	Medial	0.8	1.33	0.71	0.81	0.88
	Lateral	0.85	1.36	0.94	1.03	1.11

Table 5.12: Summary of the results using $\simeq 5000$ elements, $E = 20, \nu = 0.3$ and without the impact of the ligaments included in Tables 5.3, 5.6, 5.9, 5.10 and 5.11. The baseline case is the case where the elastic foundation is used with the Sphere/Plane meshes model. Inclined corresponds to the case where planes are inclined, Polynomial corresponds to the case where planes are constructed with polynomials of degree 3 and Scanned corresponds to the case of the scanned contact of the Femur/Tibia meshes.

This phenomenon may be termed the "luck of choice" and is specific to the dimension of the knee in question. Instead of looking at the right knee first, where the lateral condyle is larger than the medial condyle, an alternative approach is to consider other dimensions. The alternative model presented in the thesis by [14] is employed. The geometry of this problem is presented in Appendix B.2.. It should be noted that this is a left knee model. In comparison to the right knee, the medial and lateral condyles are reversed; the medial condyles are on the right and the lateral condyles are on the left. The application of an external force of $800N$ to the centre of the distal tibia at 0 degrees of flexion, with the point of impact moving along the transverse axis, gives Figure 5.22.

This figure is based on the first model, the Rigid model. There is no interest in redoing an

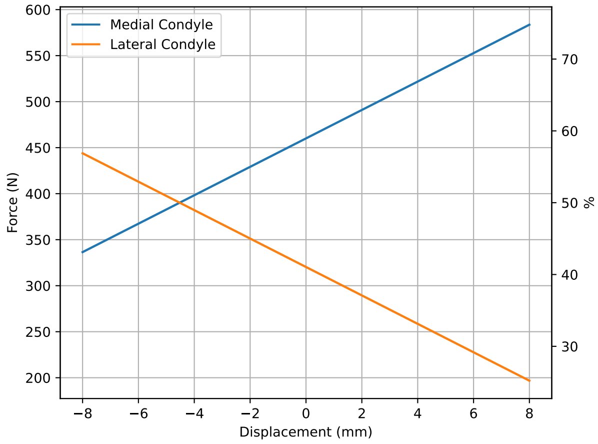

Figure 5.22: Variation of the force passing through the two femoral condyles for an another knee size as a function of the position of the application point in the transverse axis, where displacement 0 is the reference point, positive displacement is to the right and negative displacement is to the left.

entire analysis on these new dimensions. The results are similar (less than 1% error) to those in Figure 5.2, which shows the variation of the impact point force for the knee dimensions initially studied.

The only major difference is that the lateral condyle replaces the medial condyle. This is simply because a left knee is now being analysed rather than a right knee. If a force is applied with a positive displacement of the impact point, the medial condyle will receive more repartition than the lateral.

Chapter 6

Conclusions

This thesis presents an indepth study of the modeling and analysis of tibio-femoral joint contact by integrating surface meshes with a multibody formalism. The main objective was to develop an accurate and efficient model to simulate the complex interactions within the knee joint, focusing on the dynamics of the contact between the femur and the tibia. The research used advanced computational techniques, including the generation of precise anatomical meshes, collision detection algorithms and dynamic modeling of contact forces.

These finite element models were employed to simulate the different pressures within the knee. The implemented models were validated by simulation, demonstrating their ability to accurately reproduce real-world biomechanical behaviour.

A number of results have led to a better understanding of the physical phenomena involved in simulating the knee joint. In particular, the contact forces were found to be highly dependent on the point of impact of the external force. The maximum pressure also varies, but remains within acceptable values for bone and cartilage.

The influence of parameter approximations, such as the Young's modulus or the Poisson coefficient, has little effect on the models. This suggests that the models are capable of capturing the key physical phenomena and that the simplifications made do not impact too greatly.
However, the representation of the joint surface geometry remains a crucial point for the accuracy of the simulations, whether using inclined surface meshes, polynomials or anatomical meshes. The quality of the meshes and models used must therefore be carefully considered in order to guarantee accurate results. For example, the ligament model is too simplistic when using precise anatomical meshes. Another example is the simple fact that an error in the dimensions of the geometry can affect the results, as happens with intercondylar contact.

In conclusion, despite all the simplifications and approximations made, results were obtained that remain consistent with clinical observations and experimental data. This suggests that the models are capable of capturing key physical principles and providing valuable information on joint mechanics. However, significant improvements are still needed to increase the validity and accuracy of the models.

Recommendations For Future Work

In view of the results presented in Chapter 5, the most obvious approach would be to improve the modeling of ligaments. Indeed, ligaments play a crucial role in knee stability and force distribution. More realistic modeling, considering the viscoelastic properties and anatomical variability of ligaments, could improve the accuracy of simulations. The integration of experimental data or more advanced modeling methods, such as tensegrity models, would provide a better account of the biomechanical complexity of these structures [47]. In [48], the authors discuss the effects of ligaments with a finite element study. In addition to the bones represented in the finite element model, the introduction of ligaments would be consistent with this study.

Another suggestion for improvement would be the flexion/extension rotation of the knee, where this degree of freedom could be added and constrained by the application of muscles. Indeed, knee rotation is an important movement for many daily and sporting activities, and its modeling could provide valuable information on joint constraints and injury risk. This would be done more in the dynamics of the movement than in the statics, enabling a better understanding of the forces at play during complex movements, such as a vertical jump with a view larger than the knee [49].

Several other possibilities may be possible. For example, the simulation of dynamic and non-linear conditions, such as complex movements, impact loads and fatigue effects, could be improved. Indeed, joints are often subjected to dynamic and non-linear forces in everyday life, and modeling these aspects is essential for a complete understanding of their function and pathology. On the subject of pathology, another idea would be to simulate the effects of common pathologies (such as osteoarthritis) [50].

Tibio-femoral contact and, more generally, knee and other joint biomechanics are expanding areas of research, and many questions remain unanswered. It is therefore obvious that tibio-femoral joint contact models offer great potential to improve understanding of joint biomechanics and to guide the development of new therapies and treatments. By combining experimental and numerical approaches, and integrating anatomical and clinical data, these models are expected to be more accurate and comprehensive, and can be used for both clinical and research applications.

Appendix A

Clinical Terminology

A.1 Reference Planes

The reference planes of the body are listed in Figure A.1. The neutral position of the body in relation to these planes is defined when the body is upright, with feet together and arms at the sides with the palms facing forward.

- *Sagittal plane:* A vertical plane that divides the body into right and left parts.
- *Frontal or Coronal plane:* A vertical plane that divides the body into front and back parts.
- *Transverse or Horizontal plane:* A horizontal plane that divides the body into upper and lower parts.

A.2 Anatomical Directions

The following terminology has been adopted to describe joint structures and movement in relation to anatomical directions:

- *Anterior:* Towards the front of the body.
- *Posterior:* Towards the back of the body.
- *Right:* To the right side of the body.
- *Left:* To the left side of the body.
- *Superior:* To the top or towards the head-end of the body.
- *Inferior:* Towards the bottom or away from the head-end of the body

As engineers, let's talk about axes. Each axis is associated with two directions, which gives the three main axes:

- *Transverse axis:* It is the axis that extends from the left to the right of the body. In this thesis, it is associated with the x-axis and is positive towards the right.
- *Antero-posterior axis:* As its name suggests, is the axis that extends from the front to the back of the body. In this thesis, it is associated with the y-axis and is positive towards the front.
- *Longitudinal axis:* It is the axis that extends from the top to the bottom of the body. In this thesis, it is associated with the z-axis and is positive towards the top.

A.3 Description of Motion

When describing movement at a joint, different conventions have been adopted for different joints. At the knee, rotations in three reference planes are usually considered:

- *Flexion and Extension:* Rotation in the sagittal plane. Flexion bends the knee, while extension straightens it.
- *Internal and External:* Rotation in transverse plane about the long axis of the femur. Internal rotation is when the foot is turned inwards (towards the mid-line), while external rotation is when the foot is turned outwards.
- *Abduction and Adduction:* Rotation in the frontal plane. Abduction is when the knee moves away from the midline of the body, while adduction is when the knee moves towards the midline of the body.

A.4 Relative Directions

There are other terms to describe anatomical directions. For example, there is *Distal* and *Proximal*, which are used to describe parts of the limbs in relation to their point of attachment to the trunk.

- *Distal:* Away from the point of attachment or further from the centre of the body.
- *Proximal:* Close to the point of attachment or closer to the centre of the body.

In the application with the knee, the primary uses will be *Medial* and *Lateral*.

- *Medial:* Towards the middle of the body or close to the median line.
- *Lateral:* Away from the middle of the body or towards the sides.

This is depicted in Figure A.2.

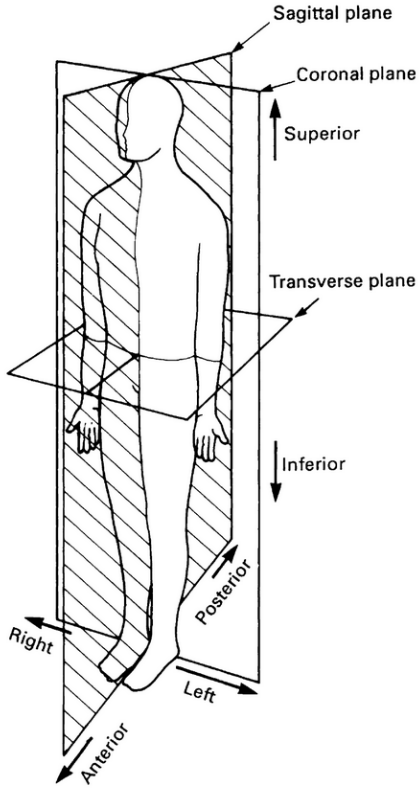

Figure A.1: The three reference planes and six fundamental directions of the human body, with reference to the anatomical position. Figure provided with permission from [51].

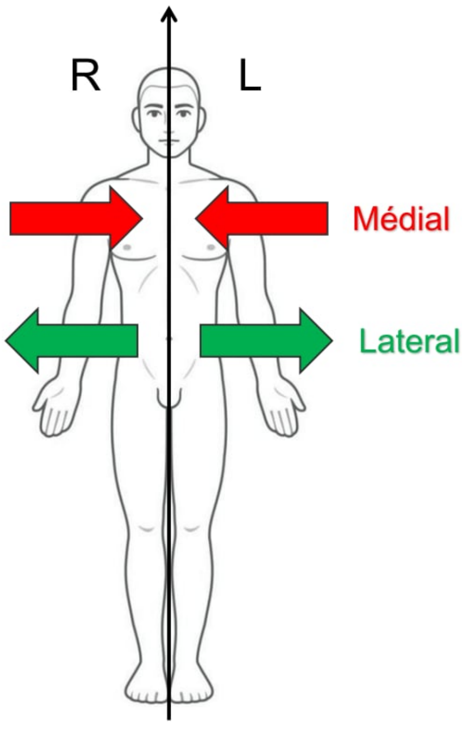

Figure A.2: The two most commonly used anatomical relative directions of the human body.

Appendix B

Model Parameters

B.1 Baseline Model

The dimensions of a right knee used for all the basic analyses are listed in Table B.1.

		x(mm)	y(mm)	z(mm)
Femur	ACL attachment	17.0	31.4	20.4
	PCL attachment	-7.9	21.3	8.8
	MCL attachment	-38.0	13.8	11.2
	Medial condyle center	-20.4	12.8	16.8
	Lateral condyle center	28.3	12.8	25.8
Tibia	ACL attachment	0.0	0.0	0.0
	PCL attachment	18.3	35.5	-21.3
	MCL attachment	-3.0	-1.0	-64.6
	Medial contact point	-20.4	12.8	-8.7
	Lateral contact point	28.3	12.8	-6.0

Table B.1: Parameters of the baseline model. The origin of the model is defined at the center of the tibial plateau. The coordinates are given in millimeters. The x-axis is defined as the transverse axis, the y-axis as the antero-posterior axis, and the z-axis as the longitudinal axis. The values are taken from [14].

This allows us to determine the radius of the condyle and the length of the ligaments, which is the distance between the attachment points:

$$L = \sqrt{(x_2 - x_1)^2 + (y_2 - y_1)^2 + (z_2 - z_1)^2}$$

The results obtained are summarised in Table B.2.

B.2 Additional Model

The dimensions of the other knee, which is a left knee, are indicated in Table B.3.

	Length(mm)
ACL Ligament	41.12
PCL Ligament	42.36
MCL Ligament	84.82
Medial Radius Condyle	25.5
Lateral Radius Condyle	31.8

Table B.2: Length of the radius and ligaments of the baseline model calculated using the dimensions in Table B.1.

		x(mm)	y(mm)	z(mm)
Femur	ACL attachment	-5.7	3.6	29.7
	PCL attachment	10.2	5.4	20.2
	MCL attachment	43.5	-2.4	27.7
	Medial condyle center	24.3	0.1	24.8
	Lateral condyle center	-27.5	0.1	25.6
Tibia	ACL attachment	0.0	0.0	0.0
	PCL attachment	-6.9	26.1	-14.3
	MCL attachment	14.0	-6.0	-58.8
	Medial contact point	24.3	0.1	-2.1
	Lateral contact point	-27.5	0.1	0.1

Table B.3: Parameters of the different model for a new left knee. The origin of the model is defined at the center of the tibial plateau. The coordinates are given in millimeters. The x-axis is defined as the transverse axis, the y-axis as the antero-posterior axis, and the z-axis as the longitudinal axis. The values are taken from [14].

Table B.4 lists radius and ligament lengths.

	Length(mm)
ACL Ligament	30.46
PCL Ligament	43.72
MCL Ligament	91.46
Medial Radius Condyle	26.9
Lateral Radius Condyle	25.7

Table B.4: Length of the radius and ligaments of the additional model calculated using the dimensions in Table B.3.

B.3 Mesh Representation

Figure B.1 shows two visualisations of the scanned meshes used to represent the femur and tibia in the model.

(a) Tibia + Fibula

(b) Femur

Figure B.1: Visualisation in the frontal plane of the complete meshes used to represent the tibia (a) and femur (b).

Appendix C

Mathematical Reminder

C.1 Spherical Coordinates

Spherical coordinates are a system of three-dimensional coordinates that describe the position of a point in space using three variables: radial distance, azimuth angle and polar angle.

- *Radial distance (r):* The distance from the origin to the point.
- *Azimuth angle (θ):* The angle between the x-axis and the projection of the point onto the xy-plane. This angle ranges from 0 to 2π.
- *Polar angle (ϕ):* The angle between the z-axis and the line segment connecting the origin to the point. This angle ranges from 0 to π.

These variables are shown in Figure C.1.

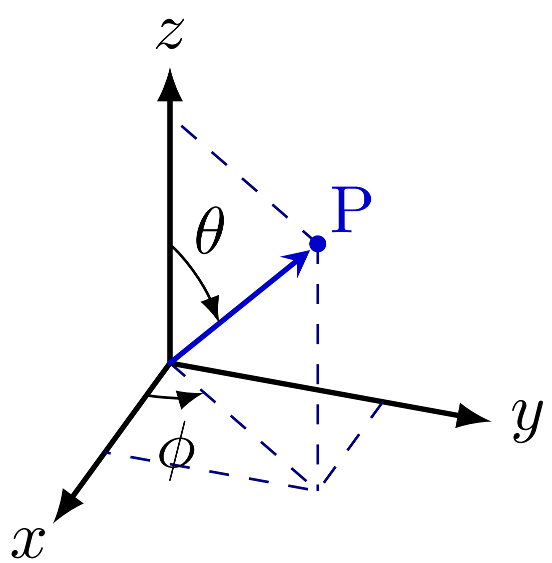

Figure C.1: Representation of spherical coordinates used to describe points.

To convert from Cartesian to spherical coordinates, the following equations are employed:

$$\begin{cases} r = \sqrt{x^2 + y^2 + z^2} \\ \theta = \arctan\left(\frac{y}{x}\right) \\ \phi = \arccos\left(\frac{z}{r}\right) \end{cases} \tag{C.1}$$

And vice-versa:

$$\begin{cases} x = r\sin(\phi)\cos(\theta) \\ y = r\sin(\phi)\sin(\theta) \\ z = r\cos(\phi) \end{cases} \tag{C.2}$$

C.2 Rotation Matrices

In this appendix, the equations of the calculated plane are used to find the rotation matrices. This means that the plane $z = ax + by + c$ must be aligned with the plane $z = 0$. The normal vector of the plane $\mathbf{n} = (a, b, -1)$ must be collinear with the vector $\mathbf{k} = (0, 0, 1)$. The rotation around the y axis cancels the a component of the normal vector $\mathbf{n}$ and modifies it as follows:

$$\mathbf{n}' = R_y(\theta_y)\mathbf{n} = \begin{pmatrix} \cos(\theta_y) & 0 & \sin(\theta_y) \\ 0 & 1 & 0 \\ -\sin(\theta_y) & 0 & \cos(\theta_y) \end{pmatrix} \begin{pmatrix} a \\ b \\ -1 \end{pmatrix} = \begin{pmatrix} \cos(\theta_y)a + \sin(\theta_y) \\ b \\ -\sin(\theta_y)a + \cos(\theta_y) \end{pmatrix} \tag{C.3}$$

Let's try to ensure that the x component of the resulting normal vector is zero, and that the following is true :

$$\theta_y = -\arctan(a)$$

Next a rotation about the x-axis is sought to eliminate the b component of the normal vector $\mathbf{n}$. After a rotation about the y axis, the new normal vector is $\mathbf{n}' = (0, b, -\sqrt{1 + a^2})$. The component y of the normal vector must be zero, so the result is :

$$\mathbf{n}'' = R_x(\theta_x)\mathbf{n}' = \begin{pmatrix} 1 & 0 & 0 \\ 0 & \cos(\theta_x) & -\sin(\theta_x) \\ 0 & \sin(\theta_x) & \cos(\theta_x) \end{pmatrix} \begin{pmatrix} 0 \\ b \\ -\sqrt{1 + a^2} \end{pmatrix} = \begin{pmatrix} 0 \\ b\cos(\theta_x) + \sqrt{1 + a^2}\sin(\theta_x) \\ -b\sin(\theta_x) + \sqrt{1 + a^2}\cos(\theta_x) \end{pmatrix} \tag{C.4}$$

This provides the following

$$\theta_x = \arctan\left(\frac{b}{\sqrt{1 + a^2}}\right)$$

The angles λ and γ, which are described in Figure 2.4b, can easily be found with the equations of the plane found by least squares.

Appendix D

Algorithm

D.1 Collision Detection

Here is the pseudo-code (Algo. 4) which corresponds to the broad phase of the collision algorithm where, for each node, the following information can be obtained:

- *isLeaf()* : checks whether the node is a leaf
- *bv*: provides the node's bounding volume
  - *overlap()* : checks whether there is an overlap between two bounding volumes
  - *size()* : give the size of the bounding volume
- *children* : lists the two children of the node

Algorithm 4 CollisionRecursive

```
Function CollisionRecursive(root1, root2)
  node1 ← root1
  node2 ← root2
  if not node1.bv.overlap(node2.bv) then
    return false
  end if
  if node1.isLeaf() and node2.isLeaf() and node1.bv.overlap(node2.bv) then
    return true
  end if
  if node2.isLeaf() or (not node1.isLeaf() and node1.bv.size() > node2.bv.size()) then
    if collisionRecursive(node1.children[0],node2) then
      return true
    end if
    if collisionRecursive(node1.children[1], node2) then
      return true
    end if
  end if
  else
    if collisionRecursive(node1, node2.children[0]) then
      return true
    end if
    if collisionRecursive(node1, node2.children[1]) then
      return true
    end if
  end else
  return false
end Function
```

Bibliography

[1] V. Wylde, A. Beswick, J. Bruce, A. Blom, N. Howells, and R. Gooberman-Hill, "Chronic pain after total knee arthroplasty," *EFORT Open Reviews*, vol. 3, p. 461, Aug. 2018.

[2] L. Kapandji, *The Physiology of the Joints, Vol. 2 The Lower Limb. Churchill Livingstone, 5th edition.* 1987.

[3] J. A. C. Ambrósio and A. Kecskeméthy, "Multibody dynamics of biomechanical models for human motion via optimization," in *Multibody Dynamics* (J. C. García Orden, J. M. Goicolea, and J. Cuadrado, eds.), (Dordrecht), p. 245–272, Springer Netherlands, 2007.

[4] M. S. Hefzy and E. S. Grood, "Review of knee models," *Applied Mechanics Reviews*, vol. 41, p. 1–13, Jan. 1988.

[5] M. Sharif Shourijeh and J. McPhee, "Forward dynamic optimization of human gait simulations: A global parameterization approach," *Journal of Computational and Nonlinear Dynamics*, vol. 9, July 2014.

[6] K. H, W. Ps, A. S, G. A, and H. T, "Geometry and motion of the knee for implant and orthotic design," *Journal of biomechanics*, vol. 18, no. 7, 1985.

[7] J. Savlovskis and K. Raits, "Anatomy standard, 2021-2023."

[8] J. H, S. P, and S. P, "A sensory role for the cruciate ligaments," *Clinical orthopaedics and related research*, July 1991.

[9] A. Wilson, "Knee anatomy including ligaments, cartilage and meniscus."

[10] C. W. McCutchen, "The frictional properties of animal joints," *Wear*, vol. 5, p. 1–17, Jan. 1962.

[11] C. Bailey, "Joint : a beginner's guide to the knee," Jan. 2021.

[12] Multibody Research Group of MEED, *Robotran 1.24.2.* https://www.robotran.be/, Université catholique de Louvain (UCLouvain), 2023.

[13] J. Samin and P. Fisette, *Symbolic Modeling of Multibody Systems.* 01 2003.

[14] J. Feikes and J. D. Feikes, *The mobility and stability of the human knee joint.* http://purl.org/dc/dcmitype/text, University of Oxford, 2000.

[15] M. Pandy, K. Sasaki, and S. Kim, "A three-dimensional musculoskeletal model of the human knee joint. part 1: Theoretical construct," *Computer methods in biomechanics and biomedical engineering*, vol. 1, no. 2, 1998.

[16] J. Wismans, F. Veldpaus, J. Janssen, A. Huson, and P. Struben, "A three-dimensional mathematical model of the knee-joint," *Journal of Biomechanics*, vol. 13, p. 677–685, Jan. 1980.

[17] M. Machado, P. Flores, J. Ambrósio, and A. Completo, "Influence of the contact model on the dynamic response of the human knee joint," *Proceedings of the Institution of Mechanical Engineers, Part K: Journal of Multi-body Dynamics*, vol. 225, p. 344–358, Dec. 2011.

[18] T. M. Guess, G. Thiagarajan, M. Kia, and M. Mishra, "A subject specific multibody model of the knee with menisci," *Medical Engineering - Physics*, vol. 32, p. 505–515, June 2010.

[19] N. Schlömer, *PyGmsh 1.2.0: A Python frontend for Gmsh.* https://github.com/nschloe/pygmsh, 2024.

[20] C. Geuzaine and J.-F. Remacle, "Gmsh reference manual: the documentation for gmsh, a finite element mesh generator with built-in pre-and post-processing facilities," *URL http://www. geuz. org/gmsh*, Jan. 2008.

[21] D.-H. et al., *trimesh 3.2.0.* https://trimesh.org/, 2019.

[22] T. M. Guess, S. S. Razu, K. Kuroki, and J. L. Cook, "Function of the anterior intermeniscal ligament," *The Journal of Knee Surgery*, vol. 31, p. 068–074, Jan. 2018.

[23] T. M. Guess and S. Razu, "Loading of the medial meniscus in the acl deficient knee: A multibody computational study," *Medical Engineering - Physics*, vol. 41, p. 26–34, Mar. 2017.

[24] M. Kazemi, Y. Dabiri, and L. P. Li, "Recent advances in computational mechanics of the human knee joint," *Computational and Mathematical Methods in Medicine*, vol. 2013, no. 1, p. 718423, 2013.

[25] F. Developers, *python-fcl.* https://pypi.org/project/python-fcl/, 2023.

[26] B. Mirtich, "Efficient algorithms for two-phase collision detection," Tech. Rep. TR97-23, MERL - Mitsubishi Electric Research Laboratories, Cambridge, MA 02139, Dec. 1997.

[27] Y. R. Serpa and M. A. F. Rodrigues, "Broadmark: A testing framework for broad-phase collision detection algorithms," *Computer Graphics Forum*, vol. 39, no. 1, p. 436–449, 2020.

[28] W. R. Franklin and S. V. G. de Magalhães, "Parallel intersection detection in massive sets of cubes," in *Proceedings of BigSpatial'17: 6th ACM SIGSPATIAL Workshop on Analytics for Big Geospatial Data*, (Los Angeles Area, CA, USA), 7-10 Nov 2017.

[29] C. C. Wang, M. Wang, J. Sun, and M. Mojtahedi, "A safety warning algorithm based on axis aligned bounding box method to prevent onsite accidents of mobile construction machineries," *Sensors (Basel, Switzerland)*, vol. 21, p. 7075, Oct. 2021.

[30] L. J. H. Seelen, J. T. Padding, and J. A. M. Kuipers, "A granular discrete element method for arbitrary convex particle shapes: Method and packing generation," *Chemical Engineering Science*, vol. 189, p. 84–101, Nov. 2018.

[31] G. V. D. Bergen, "A fast and robust gjk implementation for collision detection of convex objects," 1999.

[32] P. Lindemann, "The gilbert-johnson-keerthi distance algorithm," 2009.

[33] G. Bergen, "Proximity queries and penetration depth computation on 3d game objects," Jan. 2001.

[34] J. J. Muñoz and G. Jelenić, "Sliding contact conditions using the master–slave approach with application on geometrically non-linear beams," *International Journal of Solids and Structures*, vol. 41, p. 6963–6992, Dec. 2004.

[35] Tyler, D. Cournapeau, E. Burovski, P. Peterson, W. Weckesser, J. Bright, and S. J. . van der Walt, "SciPy 1.0: Fundamental Algorithms for ScientificComputing in Python," *Nature Methods*, vol. 17, pp. 261–272, 2020.

[36] B. Krayer and S. Müller, "Generating signed distance fields on the gpu with ray maps," *The Visual Computer*, vol. 35, p. 961–971, June 2019. Company: Springer Distributor: Springer Institution: Springer Label: Springer number: 6 publisher: Springer Berlin Heidelberg.

[37] G. Gilardi and I. Sharf, "Literature survey of contact dynamics modelling," *Mechanism and Machine Theory*, vol. 37, p. 1213–1239, Oct. 2002.

[38] D. Brown, *Contact Modelling for Forward Dynamics of Human Motion*. PhD thesis, Jan. 2017.

[39] G. T. Wynarsky and A. S. Greenwald, "Mathematical model of the human ankle joint," *Journal of Biomechanics*, vol. 16, p. 241–251, Jan. 1983.

[40] B. J. Fregly, Y. Bei, and M. E. Sylvester, "Experimental evaluation of an elastic foundation model to predict contact pressures in knee replacements," *Journal of Biomechanics*, vol. 36, p. 1659–1668, Nov. 2003.

[41] P. Beillas, S. Lee, S. Tashman, and K. Yang, "Sensitivity of the tibio-femoral response to finite element modeling parameters," *Computer methods in biomechanics and biomedical engineering*, vol. 10, p. 209–21, July 2007.

[42] E. Peña, B. Calvo, M. A. Martínez, and M. Doblaré, "A three-dimensional finite element analysis of the combined behavior of ligaments and menisci in the healthy human knee joint," *Journal of Biomechanics*, vol. 39, no. 9, p. 1686–1701, 2006.

[43] A. Van Oevelen, K. Duquesne, M. Peiffer, J. Grammens, A. Burssens, A. Chevalier, G. Steenackers, J. Victor, and E. Audenaert, "Personalized statistical modeling of soft tissue structures in the knee," *Frontiers in Bioengineering and Biotechnology*, vol. 11, Mar. 2023.

[44] K. N. An, S. Himeno, H. Tsumura, T. Kawai, and E. Y. S. Chao, "Pressure distribution on articular surfaces: Application to joint stability evaluation," *Journal of Biomechanics*, vol. 23, p. 1013–1020, Jan. 1990.

[45] L. Blankevoort, J. H. Kuiper, R. Huiskes, and H. J. Grootenboer, "Articular contact in a three-dimensional model of the knee," *Journal of Biomechanics*, vol. 24, p. 1019–1031, Jan. 1991.

[46] T. Donahue, M. Hull, M. Rashid, and C. Jacobs, “A finite element model of the human knee joint for the study of tibiofemoral contact,” *Journal of Biomechanical Engineering-transactions of The Asme - J BIOMECH ENG*, vol. 124, June 2002.

[47] W. Kim, “A tensegrity model of a knee for the acl reconstruction,” *Biomedical Journal of Scientific Technical Research*, vol. 10, p. 001–001, Oct. 2018.

[48] A. M. Kiapour, V. Kaul, A. Kiapour, C. E. Quatman, S. C. Wordeman, T. E. Hewett, C. K. Demetropoulos, and V. K. Goel, “The effect of ligament modeling technique on knee joint kinematics: A finite element study,” *Applied Mathematics*, vol. 4, p. 91–97, May 2013.

[49] D. J. Cleather, J. E. Goodwin, and A. M. Bull, “Hip and knee joint loading during vertical jumping and push jerking,” *Clinical biomechanics (Bristol, Avon)*, vol. 28, p. 98, Jan. 2013.

[50] A. M. Seitz, A. Lubomierski, B. Friemert, A. Ignatius, and L. Dürselen, “Effect of partial meniscectomy at the medial posterior horn on tibiofemoral contact mechanics and meniscal hoop strains in human knees,” *Journal of Orthopaedic Research*, vol. 30, p. 934–942, June 2012.

[51] M. W. Whittle, *Gait Analysis: An Introduction.* Butterworth-Heinemann, May 2014. Google-Books-ID: dYHiBQAAQBAJ.

UNIVERSITÉ CATHOLIQUE DE LOUVAIN
École polytechnique de Louvain
Rue Archimède, 1 bte L6.11.01, 1348 Louvain-la-Neuve, Belgique | **www.uclouvain.be/epl**